

Dissertation
submitted to the
Combined Faculties for the Natural Sciences and for Mathematics
of the Ruperto-Carola University of Heidelberg, Germany
for the degree of
Doctor of Natural Sciences

Put forward by
Dipl.-Phys. Oliver Picht
Born in : Worms
Oral examination : May 26, 2010

GROWTH AND CHARACTERIZATION OF BISMUTH TELLURIDE NANOWIRES

Referees :

Prof. Dr. Reinhard Neumann

Prof. Dr. Annemarie Pucci

Zusammenfassung

Polykristalline Bi_2Te_3 -Nanodrähte werden elektrochemisch in ionenspurgeätzten Polycarbonat-Membranen abgeschieden. Abscheidungen wurden unter potentiostatischen Bedingungen in Membranen mit Dicken von 10 bis 100 μm durchgeführt. Die kleinsten beobachteten Nanodrahtdurchmesser waren 20 nm in dünnen Membranen und ungefähr 140-180 nm in dickeren Membranen. Der Einfluss der verschiedenen Abscheideparameter auf die Wachstumsgeschwindigkeit der Nanodrähte wird gezeigt. Langsameres Wachstum wurde durch gezielte Änderung der Abscheidepotentiale und niedrigere Temperaturen erzielt. Eine Verlangsamung des Wachstumsprozesses wirkt sich positiv auf die Ausbildung einer bevorzugten Kristallorientierung und die Oberflächenrauigkeit der Drähte aus. Im Bezug auf strukturelle Charakteristiken bestätigen Röntgendiffraktionsmessungen und Transmissionselektronenmikroskopie das Wachstum von Bi_2Te_3 und belegen die Stabilität einiger Eigenschaften, z.B. Korngrößen oder bevorzugte Orientierung von Nanodrähten, hinsichtlich Änderungen der Abscheidebedingungen. Das Wechselspiel der Herstellungsparameter, wie Temperatur, Abscheidepotential und Nanokanaldurchmesser wird für Drähte, die in 30 μm dicken Membranen abgeschieden wurden, aufgezeigt. Aus den Röntgendiffraktionsmessungen ist erkennbar, dass die Vorzugsorientierung von Nanodrähten durch die Wachstumsbedingungen variiert werden kann, dies aber auch abhängig vom Durchmesser der Nanokanäle ist. Sowohl (015)- als auch (110)-Reflexe wurden für die Nanodrahtarrays beobachtet. Messungen mittels energiedispersiver Röntgenanalyse deuten außerdem darauf hin, dass eine Veränderung des Nanodrahtdurchmessers auch zu einer Änderung der Elementzusammensetzung der Drähte führen könnte.

Abstract

Polycrystalline Bi_2Te_3 nanowires are electrochemically grown in ion track-etched polycarbonate membranes. Potentiostatic growth is demonstrated in templates of various thicknesses ranging from 10 to 100 μm . The smallest observed nanowire diameters are 20 nm in thin membranes and approx. 140-180 nm in thicker membranes. The influence of the various deposition parameters on the nanowire growth rate is presented. Slower growth rates are attained by selective change of deposition potentials and lower temperatures. Nanowires synthesized at slower growth rates have shown to possess a higher degree of crystalline order and smoother surface contours. With respect to structural properties, X-ray diffraction and transmission electron microscopy verified the growth of Bi_2Te_3 and evidenced the stability of specific properties, e.g. grain size or preferential orientation, with regard to variations in the deposition conditions. The interdependency of the fabrication parameters, i.e. temperature, deposition potential and nanochannel diameters, is demonstrated for wires grown in 30 μm thick membranes. It is visible from diffraction analysis that texture is tunable by the growth conditions but depends also on the size of the nanochannels in the template. Both (015) and (110) reflexes are observed for the nanowire arrays. Energy dispersive X-ray analysis further points out that variation of nanochannel size could lead to a change in elemental composition of the nanowires.

Contents

1. Introduction	1
2. Thermoelectricity	3
2.1. Basic Principles - Thermoelectricity and Figure-of-Merit	4
2.2. Bismuth Telluride	9
2.3. Thermoelectric Properties of Low-Dimensional Structures	12
2.4. Bismuth Telluride Nanowires	16
3. Fabrication Method	21
3.1. Ion Track-Etched Membranes	21
3.1.1. Ion-Solid Interaction	21
3.1.2. Chemical Etching	25
3.2. Electrochemical Synthesis	27
3.2.1. Deposition of Bismuth Telluride	28
3.2.2. Nanowire Growth	30
4. Electrodeposition of Bi_2Te_3 Nanowires	33
4.1. Fabrication and Characterization of Templates	33
4.2. Experimental Set-Up for Electrochemical Deposition	38
4.3. Control of Growth Rates	41
4.4. Determination of Filling Ratios	45
Conclusions - Electrodeposition of Bi_2Te_3 Nanowires	49
5. Morphology and Structure	51
5.1. Scanning Electron Microscopy	51
5.2. X-Ray Diffraction	56
5.2.1. Membrane Thickness	60
5.2.2. Nanochannel Diameter	61

5.2.3. Deposition Temperature	64
5.2.4. Deposition Potential	66
5.3. Transmission Electron Microscopy	72
Conclusions - Morphology and Structure Analysis	77
6. Composition Analysis	79
6.1. Energy Dispersive X-Ray (EDX) Analysis	79
6.2. SEM/EDX on Nanowires	83
6.3. TEM/EDX on Nanowires	85
6.4. EDX Analysis of Nanowire Caps	86
Conclusions - Composition Analysis	89
7. Summary and Outlook	91
A. Ion Track-Etched Membranes	95
Bibliography	98
Acknowledgments	113

List of Figures

2.1. Schematics of thermoelectric devices	5
2.2. Charge carrier dependency of power factor and thermal conductivity	7
2.3. Crystal structure of bismuth telluride	11
3.1. Ion range and energy loss	24
3.2. Schematic - nanochannel geometry in ion track-etched membranes	26
3.3. Pores in ion track-etched templates	27
3.4. I - t transient for electrodeposition of nanowires	31
3.5. Freestanding submicron wires and nanowire with cap	32
4.1. Pore opening diameter dependence on etching time and membrane thickness	34
4.2. 50 μm long $\text{Bi}_{2+x}\text{Te}_{3-y}$ nanowire	36
4.3. Small diameter $\text{Bi}_{2+x}\text{Te}_{3-y}$ nanowires	37
4.4. Experimental set-up for the electrochemical deposition	39
4.5. Au cathode on polycarbonate template	40
4.6. Potential dependent growth rates in narrow nanochannels	41
4.7. Potential dependent growth rates	43
4.8. SEM/EDX - Estimate of nucleation ratios in large pores	49
5.1. Nanowire morphology	52
5.2. Cap morphology	54
5.3. Cap morphology - size dependent morphology change	55
5.4. Schematic set-up for ω - 2θ -scans	57
5.5. Theoretical peak positions for ω - 2θ scans of Te and various $\text{Bi}_{2+x}\text{Te}_{3-y}$ compounds.	59

5.6. Influence of deposition temperature on nanowire texture	60
5.7. Nanochannel diameter dependent texture variation for fixed de- position conditions : - 100 mV vs SCE	62
5.8. Nanochannel diameter dependent texture variation for fixed de- position conditions : 0 mV vs. SCE	63
5.9. Growth temperature influence on nanowire texture in thick mem- branes	64
5.10. Texture variation by deposition temperature reduction	66
5.11. Influence of the deposition potential on texture	67
5.12. Influence of the deposition potential on texture	68
5.13. (HR-)TEM on Bi ₂ Te ₃ nanowires	73
5.14. HRTEM on polycrystalline Bi ₂ Te ₃ nanowires	74
5.15. HRTEM on polycrystalline Bi ₂ Te ₃ nanowires	75
6.1. Electron-sample interaction in SEM	80
6.2. Basic principle of EDX	81
6.3. EDX analysis on nanowire bundles in SEM	84
6.4. EDX analysis in HRTEM	86
6.5. EDX spectra of nanowire caps	87
6.6. Comparison - composition of nanowires and caps	88
A.1. Correlation of channel diameter, ion fluence and resulting prob- abilities of channel overlap	96
A.2. Estimated influence of filled volume fraction and thermal conduc- tivity in nanowire-template composites	98

List of Tables

2.1. Literature overview on electrochemically deposited embedded nanowire arrays	19
4.1. Diameter-dependent growth rates	44
4.2. Temperature-dependent growth rates	45
4.3. Estimated filling ratios	48
5.1. XRD - grain sizes	71
5.2. Determined interplanar spacings by HRTEM	76
6.1. SEM/EDX on nanowire bundles	85

1. Introduction

For more than 50 years, bismuth telluride-based compounds have been and continue being the most efficient thermoelectric materials available for devices operating at room temperature. The suitability of a material for thermoelectric application is commonly described by the value of the so-called thermoelectric figure of merit (ZT). Due to the correlation between the different physical quantities contributing to the figure of merit, namely thermal conductivity, electrical conductivity and Seebeck coefficient, only minor progress has been made with respect to improvement of thermoelectric materials in the last decades [1].

Recent efforts have been devoted to the aim to increase the thermoelectric efficiency by either engineering completely new materials with improved qualities, or, as it has been recently proposed, by enhancing the properties of readily well-known materials by size reduction [2,3]. When the size of a material is reduced and becomes comparable to intrinsic length scales, e.g. spin diffusion length or mean free path of charge carriers or phonons, finite size [4,5] or quantum size effects [6] occur. This offers a new path for the enhancement of thermoelectric properties in conventional materials with additional degrees of freedom in the modification of materials properties.

Significant improvement of the figure of merit is expected, e.g. by quantization of the energies of the charge carriers [4,5]. This can manifest itself as a size dependent change in band structure, leading to a beneficial variation of the charge carrier density of states near the Fermi-level and thereby an enhancement of the Seebeck-coefficient of the material. Sufficiently small lateral dimensions are also suggested to exhibit phonon confinement effects in bismuth telluride (Bi_2Te_3) quantum wells [7]. As readily shown on bulk material [8], bismuth telluride based superlattice structures [9] and multilayered spark-plasma sintered

Bi_2Te_3 [10], enhanced phonon scattering can offer significant improvement of the thermoelectric properties.

With the advantages that bismuth telluride has demonstrated as a thermoelectric bulk material and the recent progress for thin films and superlattices based on Bi_2Te_3 , it is reasonable to consider this compound semiconductor as a model system to investigate the implications of low-dimensionality on thermoelectric materials.

Theoretical works have repeatedly pointed out the possibility to significantly enhance the thermoelectric properties of bismuth telluride, when grown as nanowires with small diameters [2, 11, 12]. Experimental validation is still pending, but first results on the reduction of the thermal conductivity of single nanowires with diameters in the range of 44-50 nm [13] are promising. However, it is suggested that further size reduction is necessary and parameters such as wire crystallinity and composition need to be highly adjustable.

In this work, Bi_2Te_3 nanowires are successfully synthesized by electrochemical deposition in ion track-etched membranes. Fabrication of suitable membranes by heavy ion irradiation of polycarbonate foils at the UNILAC linear accelerator at GSI, chemical etching and subsequent electrodeposition of bismuth telluride in the nanochannels enabled the synthesis of nanowires with diameters as small as 20 nm and nanowires with length of 100 μm . A systematic study was conducted on the influence of all relevant deposition parameters, e.g. electrolyte concentration, deposition potential and temperature, on the growth process. For a specific electrolyte, morphology, composition and crystallographic properties were investigated on nanowires with different diameters and lengths, as a function of both, deposition potential and temperature.

2. Thermoelectricity

The field of thermoelectricity covers the physical effects associated with the coupled appearance of thermal and electrical currents and hereby the transformation from thermal to electrical energy and vice versa. Since the discovery of the basic principles in the first half of the 19th century, the technological potential of thermoelectricity has been quickly established and recently regained importance outside the conventional niche applications, due to the need for cooling structures for microelectronic circuits and the search for environmentally conscious and energy saving techniques [1, 14, 15]. The basic principles governing the thermoelectric properties of bulk materials are the Seebeck, Peltier and Thomson effect, as well as Joule heating. The Seebeck effect describes the coupling between an existent temperature gradient in a material dT and an observed change in the electrical potential dU along the gradient, according to $S = \frac{dU}{dT}$, where S is the so-called Seebeck coefficient. The origin for the buildup of potential difference is the different energy and hence velocity distribution of the charge carriers, leading to a net flow of charges from the hot to the cold side of the material. Thus S depends on the majority charge carrier type, being positive for p-type and negative for n-type material. The Peltier coefficient Π determines the rate of heat exchange as a function of an electronic current I according to $Q = \Pi I$ and can also be expressed in terms of the Seebeck coefficient by $\Pi = ST$. Analogously, the Thomson coefficient τ , which describes the temperature dependence of S , can be written as $\tau = T \frac{dS}{dT}$.

2.1. Basic Principles - Thermoelectricity and Figure-of-Merit

Despite their low efficiency, thermoelectric devices are indispensable in many areas of research and everyday's life. They offer several advantages over more conventional techniques. Depending on the employed materials and without the production of exhaust fumes, as well as cooling agents, these systems are considered environmentally friendly. In addition, the scalability of thermoelectric devices, offers the possibility for selective cooling on the microscale, e.g. for electronic circuits and the potential for size-reduced thermal sensor systems. Furthermore, it is worth mentioning that the avoidance of mechanical parts in thermoelectric devices renders the devices noise- and maintenance-free, making them especially suitable for applications where long-time self-sustainable energy harvesting is needed, such as the powering of satellites [1]. In order to be able to compare the suitability of different materials for the usage in thermoelectric applications, the dimensionless so-called figure-of-merit ZT has been introduced. For current state-of-the-art materials, $ZT \approx 1$ [1]. It is a function of the physical properties of the material, namely the Seebeck coefficient S , the electrical conductivity σ , the thermal conductivity κ and the absolute temperature T ,

$$ZT = \frac{S^2 \sigma}{\kappa} T = \frac{S^2 \sigma}{\kappa_l + \kappa_e} T. \quad (2.1)$$

The Seebeck coefficient is a band structure dependent quantity, correlating an observed change in the electrical potential as the result from an applied temperature gradient along a material. In the aforementioned notation of the figure of merit, the thermal conductivity is the sum of the electronic thermal conductivity κ_e and thermal conductivity of the lattice κ_l . Especially changes in the lattice contribution should be considered for optimization of a thermoelectric material, since enhancing the electrical conductivity increases the thermal conductivity by charge carriers at the same time. A correlation between the electrical and the thermal conductivity was already phenomenologically observed for different metals by Wiedemann and Franz in 1853 [16]. For bulk metals, the ratio of the

electronic contribution to the thermal conductivity and the electrical conductivity is theoretically given by

$$\frac{\kappa_e}{\sigma} = \frac{1}{3} \left(\frac{\pi k_B}{e} \right)^2 T = L \cdot T, \quad (2.2)$$

where L is the Lorenz number, which is given by $2.44 \cdot 10^{-8} \text{ W} \cdot \Omega \cdot \text{K}^{-2}$. Fig. 2.1 shows a schematic view of a basic thermoelectric device, built of a p- and a n-type semiconducting leg. Both semiconductors are electrically connected in series, while they are thermally connected in parallel. When a temperature gradient is applied to the device (Fig. 2.1 (left)), the difference in the charge carrier velocity distributions on the hot and cold side of the n- and p-type legs of the device yields the formation of a usable potential drop and an associated electrical current. This illustrates the basic principle for energy harvesting by thermoelectricity. If an external current source is applied to a device with the same layout (Fig. 2.1 (right)), selective cooling or heating occurs, depending on the flow direction of the charge carriers, demonstrating the basic mode of operation of a Peltier cooler.

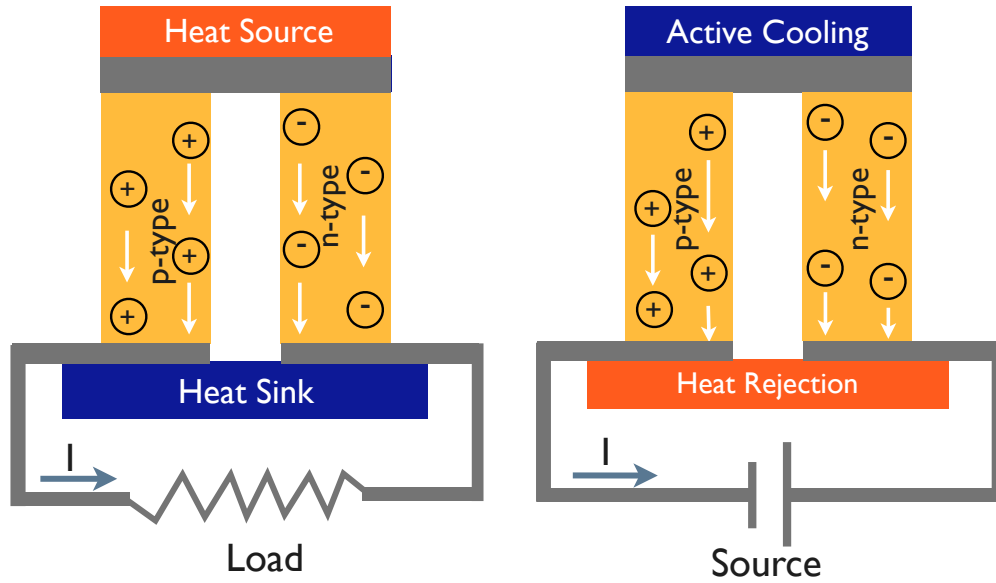


Figure 2.1.: Sketch of simplified thermoelectric devices with one n-type and one p-type semiconducting leg. Cold areas are depicted in blue, warmer areas in red. Dependent on the configuration, the systems can be used for energy generation (left) and or for cooling (right).

For a thermoelectric generator with two branches, operated with a given resistance R and an electrical current I , the efficiency can be written as [15]

$$\eta = \frac{RI^2}{(S_p - S_n)IT_h + \lambda(T_h - T_c) - \frac{1}{2}RI^2}, \quad (2.3)$$

which corresponds to the ratio of the power of an external load and the heat flow to the cold side of the device structure. T_h and T_c are the temperatures at the hot and the cold side, respectively. The Seebeck coefficients of the n-type and p-type legs are given by S_p and S_n and the maximum thermal efficiency at the mean temperature T_m is described by

$$\eta = \frac{T_h - T_c}{T_h} \cdot \frac{\sqrt{1 + ZT_m} - 1}{\sqrt{1 + ZT_m} + \frac{T_c}{T_h}}. \quad (2.4)$$

For the ideal case that $ZT_m \rightarrow \infty$, the efficiency approaches the Carnot efficiency $\eta_c = \frac{T_h - T_c}{T_h}$.

Even though the parameters which need optimization to increase the efficiency of thermoelectric modules are application dependent, e.g. high thermal conductivity and high power factor $S^2\sigma$ for cooling purposes, ZT enhancement is generally desired to boost the performance of the devices. Improvement of the thermoelectric figure of merit would not only be beneficial to applications such as energy harvesting by temperature gradients or Peltier cooling for refrigeration on large scale, but also for low-dimensional sensoric devices. With an enhanced ZT , the signal-to-noise ratio (SNR) and the detectivity of thermal sensors will be increased. At the same time, noise-equivalent-power (NEP) and thermal time constant can be reduced, the latter determining the time for the read out of information of a thermal sensor, which is of great importance for time-resolved monitoring.

The interplay between the various contributions to ZT is schematically depicted in Fig. 2.2. It is shown that an increase of S alone is not sufficient for an improved ZT , since σ is reduced at the same time. Higher n is also counterproductive, due to the reduction in S and the increase of the electronic component of the thermal conductivity.

In the work of Hicks and Dresselhaus [3] the thermoelectric figure of merit was evaluated in the approximation for a material with a single parabolic band

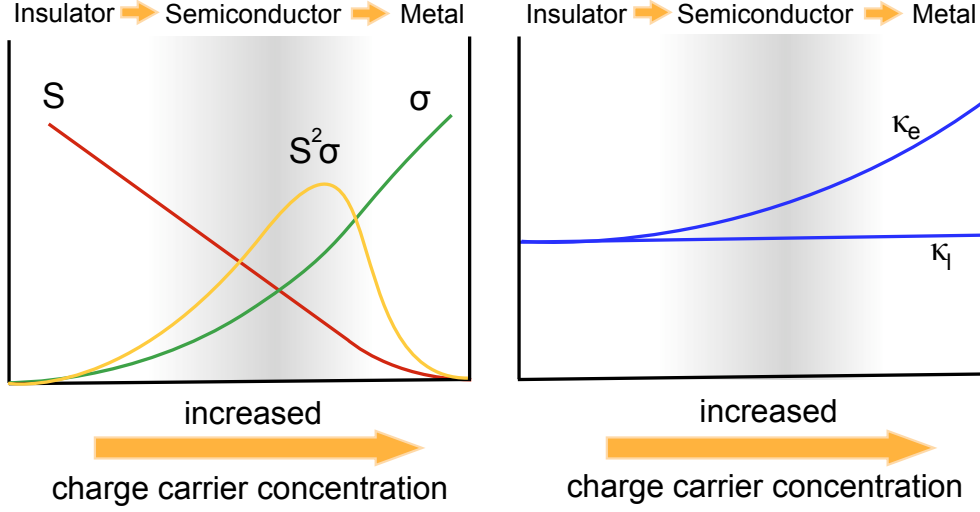


Figure 2.2.: Dependence of power factor and the charge carrier and lattice thermal conductivity on the carrier concentration. (adopted from [1] ch.9)

and the additional prerequisite of constant relaxation times τ for charge carriers. Commonly, relaxation times are energy dependent according to $\tau = \tau_0 \varepsilon^r$, where ε is reduced charge carrier energy in terms of $k_B T$ and τ_0 is a constant. For acoustic phonon scattering $r = -1/2$, $1/2$ for optical phonon and $3/2$ for ionic impurity scattering. From the measurements of Kulbachinskii et al. [17], it is assumed that the $r = 0$ is a valid approximation for Bi_2Te_3 based materials at temperatures exceeding 77 K, since r has been found to vary from $-1/2$ to $1/2$ in the temperature range from 77 to 300 K. The different contributions to the thermoelectric figure of merit can be rewritten as functions of Fermi Dirac Integrals F_m :

$$F_m = F_m(\zeta^*) = \int_0^\infty \frac{\varepsilon^m}{e^{\varepsilon - \zeta^*} + 1} d\varepsilon \quad , \quad (2.5)$$

where ζ^* is the reduced chemical potential (i.e. in terms of $k_B T$) and ε is the reduced charge carrier energy with respect to either the bottom of the conduction band or the top of the valence band, for electrons and holes, respectively. F_m represents the influence of the density of states (DOS) on ZT and specifically the variation of the electrical transport properties as a function of the chemical potential and hereby the position of dopant or impurity levels in the band gap. Hicks and Dresselhaus have arbitrarily chosen the charge carrier movement to

be in x -direction, without loss of generality. For the electrical conductivity, this yields

$$\sigma = n \cdot e\mu_x = \frac{1}{2\pi^2} \left(\frac{2k_B T}{\hbar^2} \right)^{\frac{3}{2}} (m_x m_y m_z)^{\frac{1}{2}} F_{\frac{1}{2}} \cdot e\mu_x \quad (2.6)$$

with n being the charge carrier density, m_i the effective masses and μ_x the mobility in x -direction. The Seebeck coefficient and the charge carrier contribution to the thermal conductivity are given by

$$S = \pm \left(\frac{5}{3} \cdot \frac{F_{\frac{3}{2}}}{F_{\frac{1}{2}}} - \zeta^* \right) \frac{k_B}{e} \quad \begin{cases} \text{'+' : holes} \\ \text{'-' : electrons} \end{cases} \quad (2.7)$$

$$\kappa_e = \frac{\tau \hbar^2}{6\pi^2} \left(\frac{2k_B T}{\hbar^2} \right)^{\frac{5}{2}} \left(\frac{m_y m_z}{m_x} \right)^{\frac{1}{2}} \cdot k_B \left(\frac{7}{2} F_{\frac{5}{2}} - \frac{25 F_{\frac{3}{2}}^2}{6 F_{\frac{1}{2}}} \right) \quad (2.8)$$

$$ZT_{3D} = \frac{\frac{3}{2} \cdot \left(\frac{5}{3} \cdot \frac{F_{\frac{3}{2}}}{F_{\frac{1}{2}}} - \zeta^* \right)^2 F_{\frac{1}{2}}}{\frac{1}{B} + \frac{7}{2} \cdot F_{\frac{5}{2}} - \frac{25 F_{\frac{3}{2}}^2}{6 F_{\frac{1}{2}}}} \quad (2.9)$$

$$B = \frac{1}{3\pi^2} \cdot \left(\frac{2k_B T}{\hbar^2} \right)^{\frac{3}{2}} (m_x m_y m_z)^{\frac{1}{2}} \frac{k_B^2 T \mu}{e \kappa_l} \quad (2.10)$$

Under the condition of the constant-relaxation time approximation, the given form of ZT_{3D} (equ. 2.9) exhibits two possible directions for the tuning of thermoelectric properties in bulk materials.

The first approach is to find materials with suitable intrinsic properties. These characteristics are represented by the factor B (equ. 2.10) and include the effective charge carrier masses and mobilities, as well as the lattice thermal conductivity. It can be seen that increased B is beneficial for the improvement of ZT . Hence,

- the reduction of κ_l is a suitable parameter for the enhancement of ZT . Since the lattice thermal conductivity is proportional to $T_m^{\frac{3}{2}} A^{-\frac{7}{6}}$, with A being the mean atomic weight and T_m the melting temperature of the material [18], heavy compounds such as Bi_2Te_3 are preferable thermoelectric materials.

- anisotropic materials should be grown with preferential orientation with high μ .
- for dominant acoustic scattering ($r = -1/2$), materials with low effective masses m are desirable, since $\mu = T^{-\frac{3}{2}} m^{-\frac{5}{2}}$ and therefore $B \propto m^{-1}$ ([15], p.71).

The second approach is to modify the band structure for high- B material by doping with charge carriers to obtain

- materials with high Seebeck coefficients. Under the assumption of a material without lattice thermal conductivity ($\kappa_l = 0$) and that the theoretical value for L is applicable, a minimum Seebeck coefficient of $\approx 160 \mu\text{V/K}$ is required to obtain $ZT = 1$.
- an optimum of the power factor. For semiconductors this is found for charge carrier concentration of approx. $10^{19}/\text{cm}^3$ [1].

Since S, σ , and κ are temperature dependent quantities, high ZT values can only be realized for material-specific temperature ranges. An overview of the temperature dependent performance of different thermoelectric materials can be found e.g. in [1] or [15]. Bismuth telluride satisfies several of the extracted criteria, e.g. low lattice thermal conductivity, anisotropic electrical properties, high Seebeck coefficients and easily tunable composition by deviation from the stoichiometric composition or by alloying with isostructural compounds, e.g. Sb_2Te_3 or Bi_2Se_3 .

2.2. Bismuth Telluride

Bismuth telluride Bi_2Te_3 is the basis for most of today's thermoelectric devices operating close to room temperature. Despite the environmental aspects and health concerns associated with the use of tellurium, the lack of alternative materials and its high ZT still makes Bi_2Te_3 based compounds the optimal candidates for prototype device structures in many areas of application, e.g. energy harvesting from the heat of car exhaust systems [1].

A figure of merit as high as 0.72 in p-type $(\text{Bi}_1\text{Sb}_1)\text{Te}_3$ has already been reported in 1958 by Wright et al. [19]. Recently published high ZT of 1.04

in n-type $\text{Bi}_2(\text{Te}_{0.94}\text{Se}_{0.06})_3$ [20] and 1.41 in p-type $(\text{Bi}_{0.25}\text{Sb}_{0.75})_2\text{Te}_3$ [21] thin films underline the potential of engineering well-known materials for further improvement of their thermoelectrical properties, the importance of Bi_2Te_3 and its ternary compounds with Sb and Se for thermoelectric technology.

Undoped bismuth telluride is a p-type semiconductor with a Seebeck coefficient of $230 \mu\text{V/K}$. This compound has the big advantage of being tunable from p- to n-type by doping with Cu, I, Te, or Se. For enhancement of the p-type characteristics, the binary compound can be doped e.g. with Bi, Si, or Sb, where in both cases the ternary system with the latter compound is the technologically most important one [15]. A change from p- to n-type semiconductor characteristics has also been found for increasing number densities of Te-vacancies [22]. Depending on the concentration of the elements, bismuth and tellurium form different compounds, which are mostly isostructural [23]. According to the Bi-Te phase diagram, none of these composites is more Te-rich than Bi_2Te_3 [24]. Any excess of Te is found to be either located at the boundaries between grains of bismuth telluride or form precipitates in the surrounding matrix. On the Bi-rich side of Bi_2Te_3 , several compounds have been reported, e.g. Bi_4Te_5 , Bi_6Te_7 and several more compounds which can be described by stacking sequences of Bi_2 and Bi_2Te_3 layers [23, 24]. Thereof, BiTe (tsunoite) and Bi_4Te_3 (pilsenite) are naturally occurring minerals. The crystallographic structure of Bi_2Te_3 can be described with a five-atom rhombohedral unit cell with the point group $R\bar{3}m$. Alternatively, bismuth telluride is most commonly depicted as a hexagonal lattice, with the following lattice parameters : $a = 4.3835 \pm 0.0005 \text{ \AA}$ and $c = 30.487 \pm 0.001 \text{ \AA}$ [25]. However, lattice parameters are known to change as a function of the composition [26]. In the hexagonal description (cf. Fig.2.3), one obtains a quintet of alternating bismuth and tellurium layers, $-\text{Te}^{(1)}-\text{Bi}-\text{Te}^{(2)}-\text{Bi}-\text{Te}^{(1)}-$ where three of such quintets form one supercell. The $\text{Te}^{(1)}-\text{Te}^{(1)}$ bonds are of van-der-Waals type, allowing for easy cleavage of the crystals along these planes, whereas the other bonds are more stable covalent bonds [27]. The reduced bond strength between two adjacent Te layers is also believed to be the reason for the enhanced impurity diffusion of copper as compared to the diffusion along the crystals c-axis [28]. At room temperature, the difference in the diffusion coefficients amounts to several or-

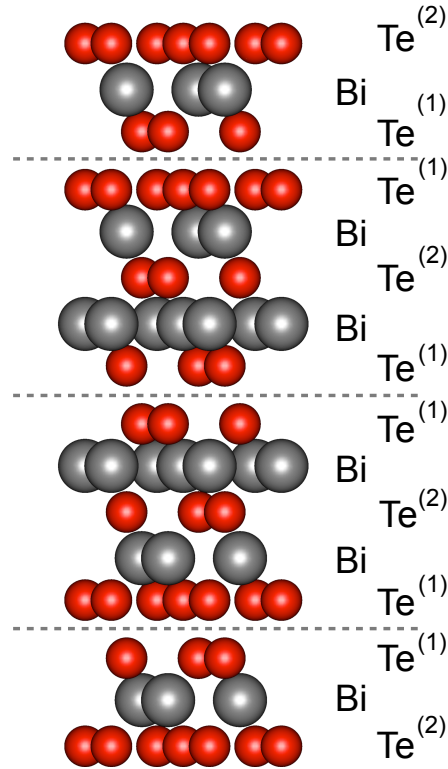


Figure 2.3.: Representation of the layered crystalline structure of bismuth telluride. The view was chosen perpendicular to the c -axis of the crystal. The Te atoms are marked dependent on their bonds by '2' (covalent) and '1' (van-der-Waals). Bi_2Te_3 quintets are separated by dashed lines.

ders of magnitude and is approx. $10^{-6} \text{ cm}^2 \text{ s}^{-1}$ parallel to the basal plane of a cleaved crystal. The highest melting temperature of the $\text{Bi}_{2+x}\text{Te}_{3-y}$ composites is found to be 858 K for a non-stoichiometric composition of 40.065 at% Bi and 59.935 at% Te [29], the mass density ρ is $7.8628 \cdot 10^3 \text{ kg/m}^3$. The electrical conductivity of intrinsic Bi_2Te_3 is in the order of $1.4 \cdot 10^4 \Omega^{-1} \text{ m}^{-1}$ at room temperature [30]. The thermal conductivity approaches 1.5 W/mK. For n-type bulk material, an overall thermal conductivity of 2-3.3 W/mK with a lattice contribution of 1.7 W/mK was reported [29]. The band structure of the compound is best described by a six-valley valence and conduction band [31, 32] with an experimentally determined band gap around 150 meV (160 meV [30], 145 meV [33]). The Fermi energy of the narrow band gap semiconductor is approximately 60 meV [34]. For doped Bi_2Te_3 the electrical conductivity is found

to be dependent on the crystal orientation [29] and, in addition, on the charge carrier type of the composite [31, 35]. In n-type compounds, the conductivity along the c-axis was determined to be of the order 4 to 5 times its value in the cleavage planes, the corresponding ratio in p-type is reported to be about 3. The thermal conductivity is shown to be reduced by a factor of 2-2.5 along the c-direction [29, 36].

While the Seebeck coefficient in the mixed and intrinsic charge carrier regime depends on the temperature gradient direction, due to the hole and electron mobility, it is isotropic in extrinsic Bi_2Te_3 [35]. Further investigations on thin films have shown, that the Seebeck coefficient depends only weakly on temperature in the region of 300 K [34].

2.3. Thermoelectric Properties of Low-Dimensional Structures

Due to the proportionality of electrical and thermal conductivity and the correlation between Seebeck coefficient and charge carrier density, the potential of enhancement of ZT in bulk material appears limited [1]. When the lateral dimension of a material or its constituting crystallites are decreased in size to intrinsic length scales, e.g. thermal wavelength of charge carriers λ_D or the phonon mean free path l , the observed physical properties will change as a function of size. Thereby, the contributions to ZT , i.e. charge carrier density, mobilities, relaxation rates and mean free paths, can be influenced by confinement and size effects in low-dimensional structures. Examples for finite size effects in low dimensional structures are, e.g., the enhanced electrical resistivity due to surface scattering of charge carriers in cylindrical wires and scattering on grain boundaries, both of which are well described by the models of Dingle [4] and Mayadas-Shatzkes [5], and have been experimentally detected in measurements on single Bi nanowires with diameters below 200 nm by Cornelius et al. [37]. With respect to the appearance of quantum size effects, single Bi nanowires have also shown to exhibit a diameter dependent shift in the infrared absorption [6], which can be explained by the theoretically predicted size dependent

changes in the band structure of Bi [38]. For an estimate of the lateral dimension at which size effects come into consideration for Bi_2Te_3 , the effective masses of electrons m_i are used to approximate the de Broglie wavelength of the charge carriers. According to [39], m_i amounts to $m_x = 0.021 m_e$, $m_y = 0.081 m_e$ and $m_z = 0.032 m_e$ for electrons, with m_e being the electron mass. With

$$\lambda_D = \left(\frac{\hbar^2}{2mk_B T} \right)^{\frac{1}{2}}, \quad (2.11)$$

the estimated wavelengths range from 17.5 to 68.4 nm. Similarly, the classical phonon mean free path l can be derived from the heat capacity c_V , the velocity of sound v and the lattice thermal conductivity by the relation

$$\kappa_l = \frac{1}{3} c_V v l, \quad (2.12)$$

which yields a range in the order of 1 nm [2]. This already indicates that sizes well below 50 nm would be favorable to observe the influence of classical size effects on the resistivity of Bi_2Te_3 nanowires.

In analogy to the treatment of bulk and quantum-well structures [3], Hicks and Dresselhaus derived an approximation of ZT in quantum wires [2], which takes the energy quantization in a wire with the square cross section of a^2 into account. Compared with the expressions given in sec. 2.1, the transport properties are altered due to changes in the band structure induced by confinement effects and are given by

$$\sigma = n \cdot e \mu_x = \frac{1}{\pi a^2} \left(\frac{2k_B T}{\hbar^2} \right)^{\frac{1}{2}} m_x^{\frac{1}{2}} F_{-\frac{1}{2}} \cdot e \mu_x \quad (2.13)$$

$$S = \pm \left(\frac{3F_{\frac{1}{2}}}{F_{-\frac{1}{2}}} - \zeta' \right) \cdot \frac{k_B}{e} \quad \left\{ \begin{array}{l} \text{'+' : holes} \\ \text{'-' : electrons} \end{array} \right. \quad (2.14)$$

$$\kappa_e = \frac{2\tau}{\pi a^2} \left(\frac{2k_B T}{\hbar^2} \right)^{\frac{1}{2}} m_x^{-\frac{1}{2}} \cdot k_B^2 T \left(\frac{5}{2} F_{\frac{3}{2}} - \frac{9F_{1/2}^2}{2F_{-1/2}} \right) \quad (2.15)$$

$$ZT_{1D} = \frac{\frac{1}{2} \cdot \left(\frac{3F_{\frac{1}{2}}}{F_{-\frac{1}{2}}} - \zeta' \right)^2 F_{-1/2}}{\frac{1}{B'} + \frac{5}{2} \cdot F_{\frac{3}{2}} - \frac{9F_{1/2}^2}{2F_{-1/2}}} \quad (2.16)$$

$$B' = \frac{2}{\pi a^2} \cdot \left(\frac{2k_B T}{\hbar^2} \right)^{\frac{1}{2}} m_x^{\frac{1}{2}} \frac{k_B^2 T \mu_x}{e \cdot \kappa_l} \quad (2.17)$$

It should be noted that the optimal reduced chemical potential ζ' for the quantum wire deviates from the bulk value and needs refinement by carrier doping. As in the case for bulk material, B' (equ. 2.17) summarizes intrinsic material properties. In the 1D approximation, beneficial influence of the size restriction is visible in the material specific parameter and its dependency of a , $B' \propto \frac{1}{a^2}$.

From the shown results of Hicks and Dresselhaus, it is evident that mainly two different approaches are pursued for the enhancement of the thermoelectric properties by low-dimensionality:

1. Quantization effects for alterations in the density of states of the charge carriers, thereby changing the DOS near the Fermi edge, and thus enhancing the power factor $S^2 n$ of a material.
2. Selective increase of phonon scattering, e.g. by superlattice structures or surface scattering, reducing the lattice contribution to the thermal conductivity and thereby increasing B' without interfering with the electrical transport properties of the thermoelectric material.

Quite a few simulations have been made of the influence of size restrictions on the thermoelectric properties of different materials. Especially the above mentioned work of Hicks et al. [2], the publications of Singh et al. [11] and Bejenari et al. [12] considered the implications of lower dimensionality on the electrical properties of Bi_2Te_3 . Hicks et al. stated that a potential increase to $ZT = 14$ for quantum wires with an edge length of 0.5 nm is possible. For larger widths of the nanowires of 1 nm $ZT = 6$ was estimated. Even though the sizes used for the calculation are improbable for experimental realisation and verification by experimental techniques in the near future, a comparison with an earlier work on the potential of quantum-well superlattice structures

as compared to conventional bulk Bi_2Te_3 [3] implied that further improvement of ZT is possible by size reduction from 2D to 1D structures. In their respective calculations on the enhanced figure of merit in Bi_2Te_3 nanowires with square cross-section, Singh et al. [11] also included a size dependent reduction of the charge carrier component of the thermal conductivity. For optimally doped wires they propose $ZT = 1.75$ and 1.2 for more experimentally feasible width of 10 and 20 nm, respectively. Similar values were evaluated by Bejenari et al. [12] for p-type wires with cross-sections ranging from 30×30 to $7 \times 7 \text{ nm}^2$. In addition, they demonstrated the shift of the optimal temperature for ZT_{max} to higher temperatures with reduced wire diameters. With respect to the reduction of the phonon contribution to the thermal conductivity, Balandin et al. [7] have proposed phonon confinement effects for thin Bi_2Te_3 quantum-well structures, which influence the phonon relaxation rates advantageously.

Since the first model calculation suggested an increase of ZT by low-dimensional structures, significant effort has focused on the formation of these structures by various techniques. In a few cases of specifically engineered films, this research has already proven the possibility of enhanced ZT , mainly due to the reduced thermal conductivity rather than changes in the electronic band structure. The highest values for the figure-of-merit near room temperature have been presented by Venkatasubramanian et al. for n-type $\text{Bi}_2\text{Te}_3/\text{Bi}_2\text{Te}_{2.83}\text{Se}_{0.17}$ superlattices with $ZT = 1.4$ and p-type $\text{Bi}_2\text{Te}_3/\text{Sb}_2\text{Te}_3$ superlattices with $ZT = 2.4$, grown by molecular beam epitaxy [9]. Multilayered spark-plasma sintered Bi_2Te_3 has been shown to exhibit ZT as high as 1.35 [10].

So far, validation of the theoretically predicted ZT enhancement is mostly found for thin films and superlattices. Only few works reported on measurement of thermoelectric properties of 1D structures. The most promising results were obtained for measurements in 50 nm diameter Si nanowires with rough surface morphology [40], where phonon scattering is assumed to be responsible for the reduction of the thermal conductivity by a factor of 100 with respect to the bulk material. The evaluated ZT is 0.6 at room temperature, albeit it should be noted that Seebeck coefficient and electrical conductivity were measured on a different wire than the thermal conductivity. An even lower value for the thermal conductivity (0.76 W/mK) has been found in 10 nm wide Si nanowires

by Boukai et al. [41], and a peak value of $ZT \approx 1$ at 200 K was evaluated for 20 nm wide wires.

With respect to measurements on Bi_2Te_3 wires, enhanced thermoelectric properties are still to be presented. First indications are made on wires with still considerably large diameters of 44-50 nm, exhibiting slightly reduced thermal conductivity as compared to bulk samples [13].

Boikov et al. [8] performed measurements on Bi_2Te_3 and the ternary $\text{Bi}_{0.5}\text{Sb}_{1.5}\text{Te}_3$ compound and demonstrated that reduced lattice thermal conductivity is present in films with small grain sizes. Annealing of the samples led to an increase of the crystallites in the film and thereby an increase of κ_l . Therefore, they proposed that enhanced grain boundary scattering could also be beneficial for the enhancement of ZT . The lower limit for the thermal conductivity is predicted to be 0.31 W/mK for nanostructured multilayers $(\text{Bi}_2\text{Te}_3)_m(\text{TiTe}_2)_n$ [42]. In conclusion, simulations and first experiments indicate that small diameters below 40 nm in combination with well-defined crystallinity and composition are necessary prerequisites for the appearance of enhanced and size-tunable ZT in low-dimensional structures.

2.4. Bismuth Telluride Nanowires

The effect of low-dimensionality on the thermoelectric properties of materials is expected to be much more pronounced in 1D than in 2D systems. Since bismuth telluride is the most effective compound for room temperature application and several theoretical works suggest that a significant improvement of ZT is possible for low-dimensional structures of this compound, different groups have started to fabricate bismuth telluride nanowires. Different approaches with their specific advantages and drawbacks have been applied. Solution and template-free based methods, such as solvothermal [43, 44] and microwave assisted wet chemical processes [45], surfactant directed growth [46] or high temperature organic solutions [46]. It should be mentioned that bismuth telluride wires are also obtainable by the chemical transformation of Te-wires [47] or galvanic displacement of Ni-nanowires [48]. While the template-free approaches are mostly

suitable for the synthesis of large amount of the compounds, the reaction products are difficult to integrate into micro- and nanoscale model device structures. Further disadvantages of these techniques can include sheath formation on the nanowires [46,47,49], short length of nanorods and large diameter distributions, all of which are undesired for well-defined nanoscale structures. Additional limitations are the use of complex and expensive organometallic precursors, toxic agents (e.g. H_2Te) and high synthesis temperatures, contributing to high fabrication costs.

A different approach combining fast and low-cost structure fabrication, with high tunability of important nanowire properties, is offered by the template-based electrochemical synthesis. By choosing the appropriate template and varying deposition conditions, all important sample parameters, such as length, diameter, crystallinity and composition can be varied with this approach. This advantage is well-known from electrochemical deposition of thin films. Over the last decades, several groups reported the electrochemical growth of bismuth telluride nanowires [50–61]. The employed techniques include all different deposition regimes: pulsed, dc, and galvanostatic. The most commonly employed template material is anodised alumina (AlO_2 - AAO), which offers high pore densities (up to $10^{10}/\text{cm}^2$), thick membranes ($\geq 100\text{ }\mu\text{m}$) combined with low channel diameters (≤ 20 to 200 nm) and high temperature stability [55].

AAO membranes need to be dissolved with acids or NaOH , in order to investigate the deposited nanowires. This can negatively influence the surface of the deposited wires, resulting e.g. in amorphous shells [55] around the wires. In the context of embedded bismuth telluride based nanowires, AAO exhibits the drawback of comparatively high thermal conductivity of 1.9 W/mK [62] at 300 K , hence acting as an effective thermal shunt in nanowire-membrane composite systems. First experiments have tried to reduce this drawback by replacing the alumina membrane by the epoxy resin SU-8 after electrochemical deposition [63]. Further template-based approaches include the electrochemical step edge decoration (ESED) on HOPG [56,61,64], where bismuth telluride lines with diameters of down to 115 nm and lengths exceeding $100\text{ }\mu\text{m}$ have been obtained at the same time.

Suffering from the drawbacks of commercially available polymer membranes,

such as low membrane thickness and large angular distribution of the channels, only few groups took the opportunity of directly using ion track-etched polymer membranes with low thermal conductivity as templates for the synthesis of thermoelectric nanowires. Koukharenko et al. [65] reported the electrodeposition of $\text{Bi}_{2+x}\text{Te}_{3-y}$ in 20 μm thick polyimide (Kapton HN). Furthermore, Xiao et al. [66] demonstrated the growth of ternary $(\text{Bi}_{1-x}\text{Sb}_x)_2\text{Te}_3$ in polycarbonate membranes purchased from Whatman Inc. With respect to the influence of the electrochemical deposition parameters for nanowire synthesis, only few investigations have been performed. In [50], the influence of varying concentrations of the cationic species in the electrolyte was explored, while in [55], the diameter of the channels in the templates has been briefly addressed as a parameter influencing the electrochemical growth process. With respect to the crystallinity of the nanowires, either polycrystalline or highly (015) and (110) textured arrays have been observed for the various deposition conditions. Furthermore, it has been demonstrated that reduced deposition temperature of 1-2 °C can increase the crystallinity of bismuth telluride nanowires, when grown by pulsed deposition [59].

Small diameters are not the only aspect for improvement of the thermoelectric performance, another keypoint of a good thermoelectric material must also be taken care of, the homogeneity of the deposited material. This particular detail also needs to be investigated for electrodeposition in reduced dimensions, where diffusion might differ from the experimental experience obtained from thin-film growth. Exemplary research on this topic was done by Wang et al. [50] on bismuth telluride nanowires deposited in 60 μm thick alumina template. The influence of the applied potential and the speed of a rotating disc electrode on the nanowire crystallinity and the Bi- and Te-concentrations over the wire length has been presented for Bi_2Te_3 wires with a diameter of 200 nm. Under static conditions and deposition at -140mV vs. SCE, the concentration of Bi was found to vary up to 0.275% per μm length.

A non-exhaustive overview over different reported electrodeposited $\text{Bi}_{2+x}\text{Te}_{3-y}$ nanowires and the corresponding templates is given in Table 2.1. Even though numerous works showed the formation of bismuth telluride based submicron wires, only few groups obtained nanowires with diameters below 40 nm, which

Deposition Method	Wire Diameter [nm]	Template	Ref.
dc	25, 50, 75	AAO	[55]
dc	25 - 260	PC	this work
dc	35	AAO	[59]
pulsed, dc, galvanostatic	40	AAO	[58]
dc	40	AAO	[60]
pulsed, dc	40, 60	AAO	[52]
dc	45	AAO	[51]
galvanostatic	50	AAO	[54]
dc	50	AAO	[57]
dc - galvanostatic	80	Polyimide (Kapton)	[65]
cyclic deposition	115 – 322	HOPG	[56]
dc	200	AAO	[50]
galvanostatic	28	AAO	[53]

Table 2.1.: Overview on electrodeposited nanowire arrays with given deposition technique, obtained nanowire diameters and used template for synthesis.

appears to be required for substantial enhancement of the thermoelectric properties [2, 11, 13, 67].

In this work, systematical investigations on the electrochemically grown Bi_2Te_3 nanowires in ion track-etched membranes are presented. By employing swift heavy ion irradiation for the template fabrication, it is possible to tune nanochannel diameters and number densities as well as the membrane thicknesses over a wide range. Due to the versatility of the combination of electrochemistry and polymer templates with highly oriented nanochannels, it was possible to fabricate cylindrical nanowires with minimum diameter of 25 nm and length of 30 μm . The influence of deposition temperature and channel diameter on the wire morphology and the preferential orientation of the nanowires is presented, indicating that the process conditions known from film and bulk growth need to be modified for Bi_2Te_3 nanowire growth. In addition, nanowires with diameters

of approx. 140 nm were also successfully grown in 60 and 100 μm thick polycarbonate membranes. This is of special interest, because it offers the comparison of recent results obtained via electrodeposition in AAO with the growth in ion track-etched membranes, giving an insight in the influence of membrane thicknesses and pore densities and hence detailing the information on the parameter space for the fabrication of well-defined thermoelectric nanowires.

3. Fabrication Method

In order to synthesize nanowire arrays with high aspect ratios, well-defined geometry and physical properties, a combination of electrochemical deposition with a template based approach was employed in this work. As known from thin films, electrochemistry offers high tunability of the nanowire properties, such as crystallinity, composition and morphology, whereas the ion-track etched polymer membranes provide high variability with respect to nanowire diameters, length, shape and number density. For the fabrication of the templates, polycarbonate films are irradiated with swift heavy ions. Along the ion trajectories, their energy loss leads to damage trails with altered chemical behaviour. In polycarbonate, these so-called latent tracks are very well defined and cylindrical in shape. In a suitable etching solution, the tracks offer significantly higher sensitivity to etching than the unperturbed polymer, resulting in a membrane with tunable nanochannel size and shape. Thereafter, these channels are electrochemically filled with bismuth telluride, resulting in submicron- or nanowire arrays with predefined properties.

3.1. Ion Track-Etched Membranes

3.1.1. Ion-Solid Interaction

In this work, amorphous polycarbonate (Makrofol N, Bayer) was chosen as a suitable membrane material for the electrodeposition of bismuth telluride nanowires. Polymer films with thicknesses of 10, 30, 60 and 100 μm were irradiated by heavy ions such as ^{197}Au , ^{206}Pb , and ^{238}U . The ions are highly positively charged and accelerated up to energies of 11.4 MeV per nucleon (MeV/u) in the UNILAC linear accelerator of GSI, with ranges exceeding 150 μm in polymers.

The ion fluence determines the degradation of the material and the density of nanochannels in the membrane. For the given purpose the fluence is varied from 10^7 to $5 \cdot 10^9$ ion per cm^2 .

When the ions pass through a solid, they interact with the atoms and the electronic system of the target. This leads to an energy loss of the projectiles along their trajectories and hence to energy dissipation within the solid. Depending on the various parameters of the ion-solid system, e.g. type of ion/solid and ion energy, different kinds of interaction phenomena occur within the target :

- Bremsstrahlung
- Cherenkov radiation
- Electronic energy loss
- Nuclear energy loss

In the case of heavy ions at specific energies of several MeV/u, bremsstrahlung is not observed. Cherenkov radiation does not occur since the ion velocity is about 5 % of the velocity of light. Assuming a refractive index of ≈ 1.6 for polycarbonate, the ion velocity should be in the order of 60% of the speed of light for Cherenkov radiation to be present [68]. The most dominant contribution is the Coulomb interaction between ions and target material. The interaction cross-section is a function of the ion velocity. Elastic collisions between the projectile and the target atoms dominate for low ion energies (≤ 0.01 MeV/u). This correlation is described by the nuclear energy loss $(dE/dx)_n$. For higher energies, electronic excitation and ionization processes gain in importance and dominate the ion-solid interaction. The energy loss in this velocity regime is called electronic energy loss $(dE/dx)_e$. A quantitative description per unit distance of the ions is possible via the Bethe-Bloch formula

$$\left(\frac{dE}{dx} \right)_e = \frac{4\pi \cdot e^2 \cdot Z_{\text{eff}}^2 \cdot Z_t \cdot N}{m_e \cdot v^2} \left[\ln \left(\frac{2m_e \cdot c^2 \cdot \beta^2}{I} \right) - \beta^2 - \delta - U \right] \quad (3.1)$$

with e being the elementary charge, m_e the electron mass, v the ion velocity, N the density of the target atoms, I the ionization energy of the target atoms, Z_{eff} the equilibrium effective charge of the projectile, Z_t the atom number of

the target element and β the velocity in units of the speed of light. When the contribution of electrons in inner atomic shells, as well as relativistic effects are negligible, the according correction factors U and δ can be discarded and the dependencies of the energy loss can be written as

$$\frac{dE}{dx} \propto \frac{Z_{\text{eff}}^2}{E} \cdot \ln \left(\frac{E}{I} \right). \quad (3.2)$$

When the charged particles penetrate the target, the ions may either capture or lose electrons, depending on their velocity compared with the orbital velocity of the electrons. Thus depending on this velocity, the ions possess an effective charge state [69], which can be described by

$$Z_{\text{eff}} = Z \left[1 - e^{-\frac{130 \beta}{Z^{2/3}}} \right]. \quad (3.3)$$

For high-velocity projectiles, the effective charge is approximately equal to the atomic number of the element, while at lower energies, the net positive charge of the incident ions is reduced. From the correlation of energy loss and effective charge state, it can be deduced that more energy can be deposited in the irradiated solid by employing high-energetic heavy ions. Depending on ion energy and charge state, the energy loss yields structural and compositional variations in the irradiated solid. For polymer membranes, e.g. polycarbonate (PC), polyethyleneterephthalate (PET), and polyimide (PI), this includes electronic excitation and destruction of chemical bonds [70, 71] or outgassing of volatile molecules [72]. Due to the structural properties of polycarbonate, the energy loss is radially isotropic around the ion trajectory. Therefore, the energy loss leads to cylindrical zones of highly damaged material with altered physical and often also chemical behaviour, the so-called latent track. With respect to the size of the latent tracks, investigations on the etching properties in 8- μm thick polycarbonate (Makrofol KG) [73] have shown the presence of a track core with a diameter of ≈ 10 nm and corresponding track halo, which can possess a diameter in the range from 20 to 200 nm. Similar sizes have also been found for ion irradiated PET [74].

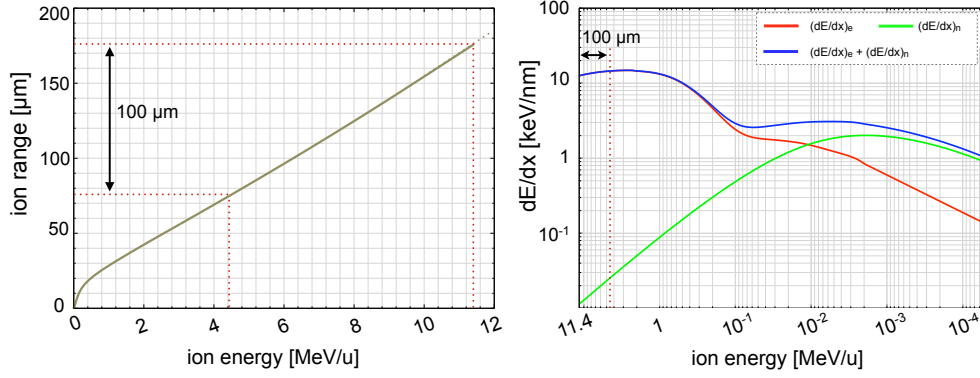


Figure 3.1.: Calculated values for projected ion range (left) and energy-specific energy loss (right) for Au ions in polycarbonate [75]. Maximum thickness of irradiated membranes is 100 μm.

The projected range of the ions R_p is determined by the kinetic energy of the particles E_0 and the specific energy loss within the solid :

$$R_p = \int_0^{E_0} \left(\frac{dE}{dx} \right)^{-1} dE \quad \text{with} \quad \left(\frac{dE}{dx} \right) = \left(\frac{dE}{dx} \right)_n + \left(\frac{dE}{dx} \right)_e, \quad (3.4)$$

where both, nuclear $\left(\frac{dE}{dx} \right)_n$ and electronic energy loss $\left(\frac{dE}{dx} \right)_e$ are taken into account. If the ions are accelerated to energies of 11.4 MeV/u¹ at the UNILAC, their projected ion range in PC is approximately 175 μm [75]. Furthermore, the electronic and nuclear energy loss have been evaluated by means of the SRIM code. The results are shown in Fig. 3.1. It can be seen that after penetration of a 100 μm thick PC, the electronic energy loss is still orders of magnitudes larger than the contribution from elastic collisions within the polymer and can be considered almost constant over the membrane thickness. For the application of polymer membranes as templates for nanowire synthesis, homogeneous energy loss along the ion trajectory is preferable, since the enhanced etching along the latent track is the key to the membrane formation. Measurements on PI (Kapton) have shown that track etching yields uniform channel size for energy losses of about 5 keV/nm, wide pore size distribution for 4.5 to 1.8 keV/nm, and for values below 1.8 keV/nm no etching was observed [76]. From the employed ion

¹corresponds to approx. 2.25 GeV for Au ions

energies and the correlation between ion velocity and energy loss, it can be seen that the homogeneity requirement is met for irradiation of stacks of polycarbonate foils with total thicknesses below 100 μm . This is well above the thicknesses of commercially available polymer membranes. In addition, the employed experimental set-up provides highly aligned channels, angular deviations of less than 1° have been reported indirectly, via XRD on single-crystalline embedded copper nanowires [77]. Mass-produced polymer membranes, which are usually fabricated for filtration purposes, can exhibit angular distributions of up to 30° . Prior to etching, a suitable treatment of our foils by UV light inhibits the strong cigar-like shape of the nanochannels, which is often observable in polycarbonate filters [78, 79].

3.1.2. Chemical Etching

In this work, polycarbonate was chosen as a suitable membrane for the electrodeposition of bismuth telluride nanowires. The employed polymer films were amorphous Makrofol N from Bayer with thicknesses of 30, 60 and 100 μm . In order to create nanochannels, the latent-track material is preferentially removed by an etching solution. The process can be described by the competition of the etch rate occurring along the latent track and isotropically in the non-irradiated bulk material, as displayed schematically in Fig. 3.2(a). The corresponding etch velocities are called track- and bulk-etching velocities (v_T and v_B). The resulting pore shape evidently depends on their ratio. For track etching rates being much larger than bulk etching rates, the resulting pores can be considered as almost cylindrical, whereas the conical character becomes the more dominant the larger the velocity ratio is. The opening angle of an etched pore can be described by

$$\alpha = \arctan\left(\frac{v_B}{v_T}\right) \quad (3.5)$$

The deliberate variation of the etching velocity ratio by alteration of the pre-etching treatment, modified etchants, e.g. addition of methanol [80], and etching from one or two sides, can lead to different pore shapes as depicted in Fig. 3.2(b)-(e).

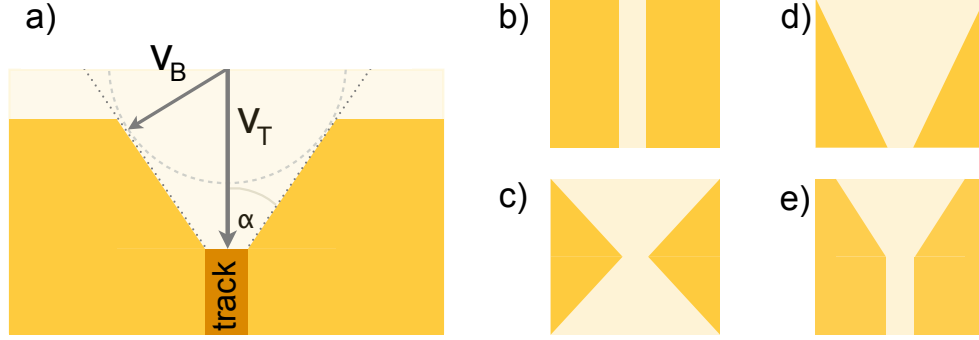


Figure 3.2.: (a) Schematic of the bulk and track etching velocities for etchant interaction with a polymer membrane. Possible geometries of nanochannels in polymer membranes : (b) cylindrical (d) conical (c) bi-conical (e) funnel-shaped nanochannels

The etching ratio is not only dependent on the polymer, but also on the ion species used for irradiation, the etching conditions, e.g. temperature, and a function of the foil thickness [81]. For the etching of tracks in polycarbonate aqueous sodium hydroxide solution (NaOH) is used. Prior to the etching process, the PC foils are exposed to UV light in air at room temperature for 60 min per side. This process is known to reduce the size distribution of the pores and to decrease the etching time needed for pore breakthrough [82, 83]. Via measurements by small angle X-ray scattering, the bulk etching rate in 30- μm Makrofol N films was determined to 21 nm min^{-1} in 5M NaOH at 333 K [83] and ranged between 25 and 30 nm min^{-1} for 6M NaOH at 323 K [84, 85], determined by measurements with SEM. It is known from prior works that aspect ratios as high as 1000 can be obtained under suitable etching conditions [86]. The multi-track foils, employed in this work, are etched in a thermostated beaker at 50 °C with stirred solution of 6M NaOH.

Polycarbonate membranes with cylindrical channels with diameters below 30 nm have been prepared and employed as templates for the electrochemical synthesis of nanowires. Scanning electron micrographs of pore openings on polycarbonate membranes are shown in Fig. 3.3. Furthermore, ion track-etching in membranes with thicknesses of 60 and 100 μm were used for the fabrication of long nanowires with lengths exceeding 60 μm .

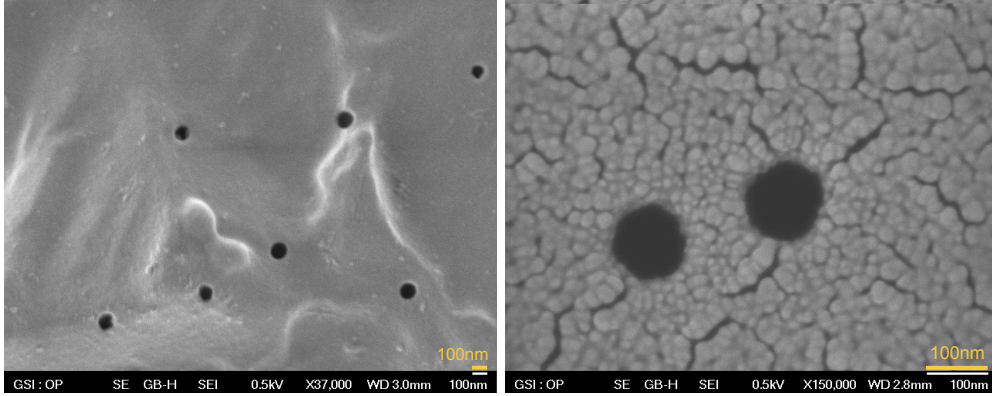
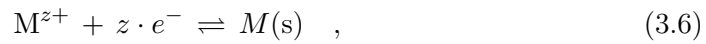


Figure 3.3.: SEM images of the pores in polycarbonate membrane without (left) and with (right) gold sputtered surface. The circular shape of the pore openings is clearly visible in both cases.

3.2. Electrochemical Synthesis

In electrochemical deposition, a solution of ions in a solvent is exposed to a gradient of the electric potential between at least two electrodes, or an electric current is forced between them [87]. For electrochemical growth of nanowires, the employed electrolyte is chosen such that reduction leads to the formation of a solid deposit on the cathode, or so-called working electrode. The reaction at the interface of the electrode and the electrolyte is described by



where M is an arbitrary ion with the charge state $z+$ and $z \cdot e$ specifies the amount of electrons needed for reduction to $M(s)$. An applied potential influences the reduction at the working electrode [88–90], hence alters the concentration gradient of the ions $\frac{dc}{dx}$ in the vicinity of the cathode and thereby tunes the mass flow J_{ion} , according to Fick's first law,

$$J_{\text{ion}} = -D \frac{dc}{dx} \quad , \quad (3.7)$$

with D being the diffusion coefficient of the investigated ion species. Our electrochemical system resembles a recessed nanoelectrode array, which leads to specific implications to the mass transport as compared to thin film growth [91,92]. For

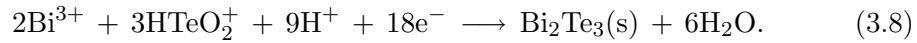
example, for high aspect ratio of the nanochannels, convection is omitted as a contribution to ion movement in the vicinity of the cathode.

As for the externally applied force which drives the electrochemical deposition, different current and potential conditions can be employed [87]: In galvanostatic mode, the current flow between working electrode and counter electrode is kept constant. In template based nanowire synthesis, a variation of the amount of contributing channels in the deposition process will give rise to altered current densities within the pores, and could thereby result in different chemical reactions, e.g. hydrogen evolution. For pulsed electrodeposition, the potential is periodically altered, starting with a potential at which material is deposited during a specific time span. Subsequently, the applied potential is changed to either partially dissolve the deposit, or to allow replenishing of the ion concentrations at potentials where the electrochemical system is at equilibrium and no reaction takes place. For composite systems such as Bi_2Te_3 , this approach includes the preferential dissolution of one of the two elements of the compound [93,94]. An alternative technique is the potentiostatic mode or dc-electrodeposition, where a constant potential is applied between the working electrode and a reference electrode in a 3-electrode setup or a counter electrode for a 2-electrode geometry. Under these conditions, the potential determines the chemical reaction, and the impact of deposition temperature and electrolyte concentration on the ion diffusion will be visible in the I - t curves, via increased or lowered currents and therefore the variation in growth rates of the deposits.

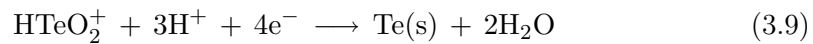
3.2.1. Deposition of Bismuth Telluride

A first description of the electrochemical deposition of Bi_2Te_3 films was given by Magri et al. [95] and Takahashi et al. [96]. With small variations in ion concentrations and pH values, their basic electrolytes are still the most widely used for thin film and nanowire synthesis. They employed nitric acid based aqueous solutions for the electrodeposition of films, demonstrating the influence of variations in the electrolyte composition under potentiostatic electrodeposition on Ti sheets [96] and the impact of changes in the current density on deposits on stainless steel for galvanostatic deposition [95], respectively. By cyclic voltammetry

(CV), Magri et al. further showed the differences between the electrodeposition from electrolytes, containing only one ionic species, i.e. either Bi or Te, and mixtures of these electrolytes. Thereby, they demonstrated that the required potentials for the compound deposition are less negative than for the reduction of the ions in single-element films. This approach has been picked up by several other groups [93,94,97] for detailed investigation of the chemical processes, associated with electrochemical deposition of bismuth telluride and its solid solutions with Bi and Te from nitric acid based electrolytes. For the electrodeposition in this work, the electrolytes were prepared by dissolution of Te powder or TeO_2 in concentrated nitric acid, subsequently mixed with $\text{Bi}(\text{NO}_3)_3 \cdot 5\text{H}_2\text{O}$ and further diluted with deionized Millipore water. The concentration of nitric acid was in the range of 1 to 1.5 M dependent on the desired concentration of Te in the solution. The concentration of bismuth and tellurium ranged from 2 mM $\text{Bi}(\text{NO}_3)_3 \cdot 5\text{H}_2\text{O}$ and 3 mM TeO_2 to 20 mM $\text{Bi}(\text{NO}_3)_3 \cdot 5\text{H}_2\text{O}$ and 32 mM TeO_2 . Concentrations found in literature are of similar amount, due to the low pH value needed to retain Te in solution and avoid precipitate formation. In general, the overall deposition of Bi_2Te_3 is described via the following chemical reaction,



A more in-depth analysis of the potential deposition processes by CV-measurements clearly indicated the diffusion and concentration of Bi^{3+} as a limiting factor in the formation of bismuth telluride [50,93]. The proposed deposition process for small negative and positive potentials with respect to the reference potential of a saturated calomel electrode (SCE) is :



and

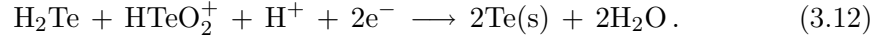


At more negative potentials, an additional reduction wave occurs in the CVs

at approx. -500mV vs. Ag/AgCl². This feature of the CV is interpreted as an intermediate step, where the direct reduction to solid Te is replaced by a two-step process with the formation of hydrogen telluride



and a subsequent reaction with the telluryl ion to form solid Te according to



By varying applied potential in potentiostatic, or current density in galvanostatic electrodeposition, it is possible to modify the reduction rates of the ions and hence alter the composition of the deposit. This has been demonstrated for the growth of thin films [26, 97–101] and for embedded wires with submicron diameters [50]. According to literature, increasingly negative potentials lead to the formation of Bi-rich Bi₂Te₃ [26, 98, 99, 102, 103]. The potential threshold for the transition between Bi-excess and deficiency is dependent on the applied conditions, e.g. ion concentration, temperature and potential, and hence varies for different employed settings [26, 50, 99, 101, 102]. Including additives, e.g. ethylene glycol, in the electrolytes has shown to influence the morphology, adhesion, and thickness of deposited films [99]. Variation of the pH-value by adding liquid ammonia has revealed that increased pH can slightly lower the grain size of Bi₂Te₃ from ≈ 150 nm for pH = 1 to almost 80 nm at pH = 3.5 [104].

3.2.2. Nanowire Growth

Even though the processes for the deposition on recessed nanoelectrodes is different from the deposition of thin films, due to influences of size restrictions [50, 91, 92, 105], i.e. changes in the diffusion coefficients and concentration gradients towards the cathodes, the concentrations of the different electrolytes were chosen similar to values presented in literature. The concentrations ranged from 2.5 mMol Bi and 4 mMol Te to 20 mM Bi and 32 mM Te.

In Fig. 3.4, the current-time curve for the electrodeposition of nanowires inside a nanochannel template is shown for the employed cell configuration. The

²The exact position of the reduction peak depends on the electrochemical system.

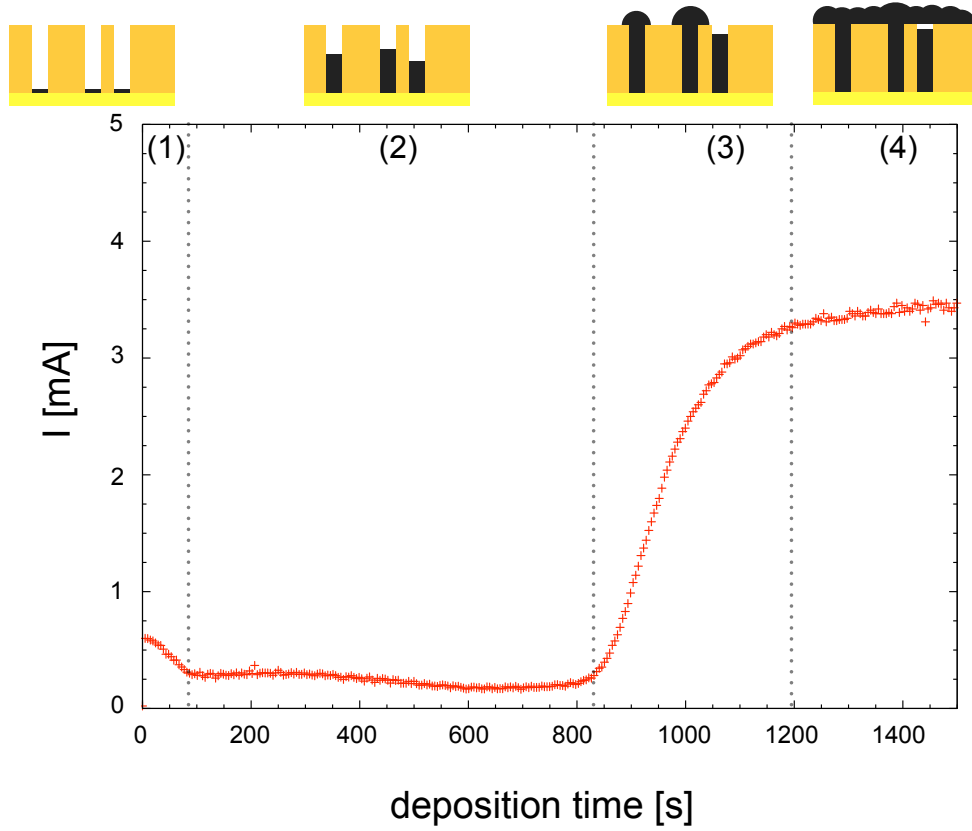


Figure 3.4.: Chronoamperometric curve for the DC-electrodeposition of nanowires in ion track-etched polymer membrane, with schematics for the different stages of the deposition process (1)-(4).

four different stages of growth are schematically depicted above. (1) In the beginning of the deposition process, a rather steep decrease of the measured current is observed. It arises due to the reduction of ions in the vicinity of the cathode, leading to the formation of nuclei, which act as seeds for the nanowires. Simultaneously to the diffusion of ions towards the cathode and their reduction, a depletion layer grows into the bulk solution. (2) During the growth within the nanochannels, a steady-state current is measured. (3) In the third stage, nanowires reach the pore openings, allowing for an increased supply of charged particles to the cathode. Due to a larger surface than the channel opening, caps quickly increase in size. The preferred reduction of the ions takes place at the caps rather than at recessed nanowire tips, until the caps finally cover

up non-completely filled channels. (4) In the stage dominated by cap growth, the current increases linearly with time until the diffusion zones for different caps overlap, the caps finally coalesce and form a continuous layer. Now the current curve saturates, depicting a steady-state linear diffusion, and the cathode finally behaves again as in the case of film deposition. Dependent on the intended application or experiment, the subsequent removal of the templates may be indispensable after the process of synthesis. The advantage of polymer membranes lies in their solubility by organic solvents, which are often chemically less aggressive towards the wires than strong acids or bases. Examples for a free-standing submicron-wire array and a hemispherical cap grown on top of a wire are shown in Fig. 3.5. In both cases, the samples were prepared by electrochemical deposition with electrolytes employed in this work.

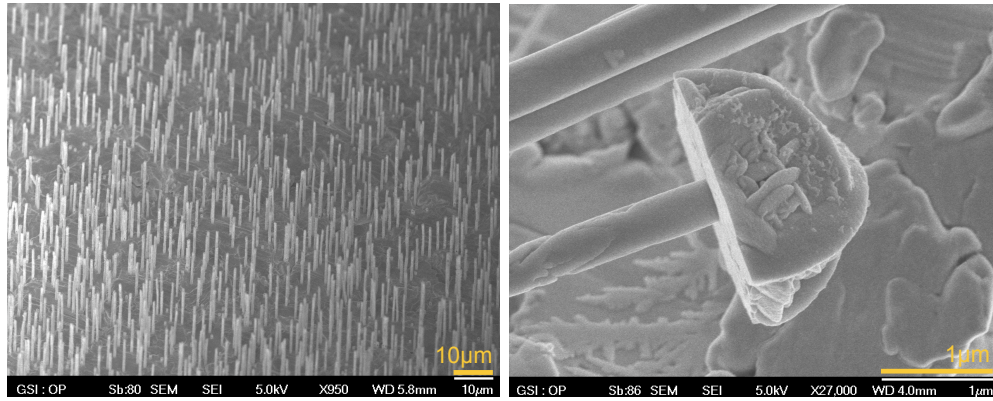


Figure 3.5.: (left) Freestanding $\text{Bi}_{2+x}\text{Te}_{3-y}$ submicron wires prepared by electrochemical deposition in PC templates and (right) submicron wire with attached cap.

4. Electrodeposition of Bi_2Te_3 Nanowires

While the electrodeposition of $\text{Bi}_{2+x}\text{Te}_{3-y}$ thin films is comparatively well-known [26, 95, 96, 98–100, 104] and few works have already dealt with the deposition in alumina templates [50–61], no systematic work has been performed on ion track-etched membranes. Prior to the description of the structural and compositional analysis of the nanowires, the membrane fabrication, as well as the influence of the various growth parameters on the synthesis is demonstrated. At first, the correlation of the etching time with the pore diameters will be demonstrated for the well-characterized 30- μm templates and the thicker membranes, which are of special interest for nanowire-based thermoelectric piles for sensorics. Then the employed electrochemical setup and the chosen experimental conditions are briefly described, followed by the presentation of the influence of various electrodeposition parameters, e.g. ion concentration, deposition potential, and temperature, on the growth rates of nanowire arrays. Furthermore, the beneficial impact of prolonged growth process by temperature reduction is discussed in terms of the filled nanochannel volume.

4.1. Fabrication and Characterization of Templates

With respect to the diverse motivation for the growth of $\text{Bi}_{2+x}\text{Te}_{3-y}$, i.e. application in sensorics and model systems for low-dimensional thermoelectricity, ion track-etched membranes fabricated at GSI are suitable to offer both, sub-micron diameter wires with length close to 100 μm , as well as high aspect ratio nanowires with diameter of approx. 30 nm at length of 30 μm . All irradiations were performed with 11.4 MeV/u Au ions to eliminate the influence of the ion

species-dependent energy loss. For the given ion energy, it is approximated that the energy loss is sufficiently large to leave homogeneous damage trails along the ion trajectory and that this assumption is also valid for membranes with thicknesses of 60 and 100 μm (see Fig. 3.1). For irradiation, membranes were stacked to not exceed maximum thicknesses of 100 μm . Etching was performed

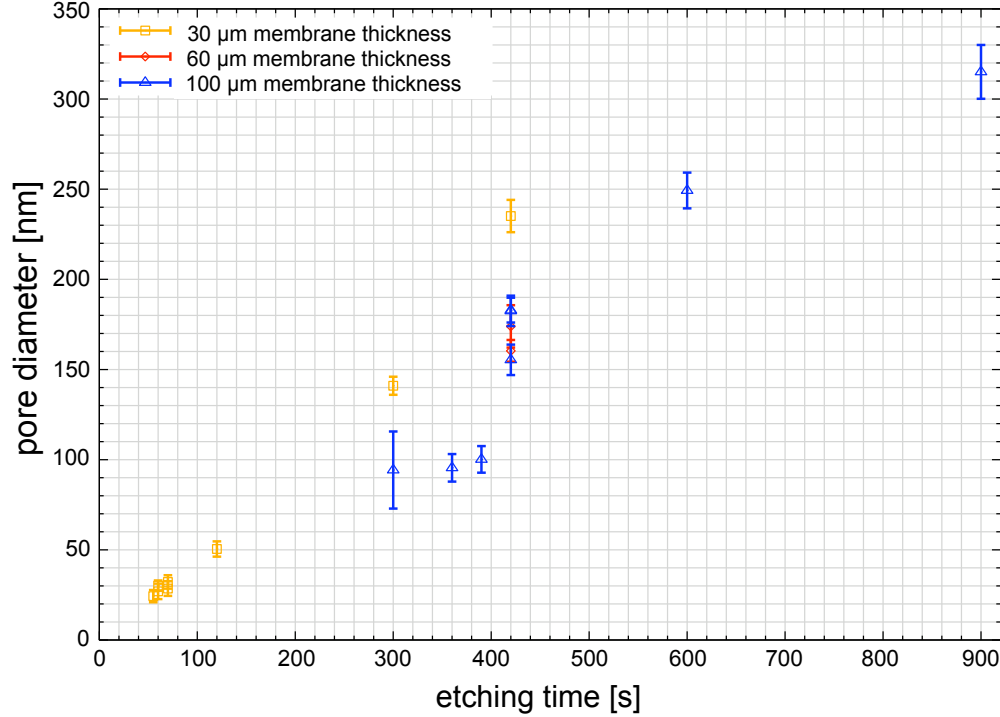


Figure 4.1.: Pore opening diameter dependence on etching time and membrane thickness for etching of 30, 60 and 100 μm thick Makrofol N foils in 6 M NaOH at 50°C.

in a thermostated bath of 6 M NaOH at 50°C. The pore openings of the templates were determined by SEM measurements with a JEOL JSM-7401F. In case of charge build-up on the sample surfaces, the polymer was coated with a thin sputtered layer of Au, which has shown to only minimally alter the diameter of the pore mouth.

Fig. 4.1 shows the correlation between etching times and the diameter of the nanochannel opening for the various membranes. For 30- μm membranes, this correlation is well-known [84–86]. Depending on small variations of the etching temperature, the channel diameter being widened with approx. 30 nm per minute etching time. For the measurements on embedded nanowires in 60 μm ,

only one set of membranes was used, which was etched specifically for 7 min. Therefore, no additional samples are included in the graph. Even though all membranes are amorphous polycarbonate from one supplier, the etching curves exhibit one distinctive difference. Counter to the expectation, etching over specific times did not result in similar, but significantly smaller pore openings in thicker membranes. This can not be solely explained by variation of temperature or an aging effect of the employed solution, even though these parameters are known to change the etching properties. In this case, it is likely that mass transport of the etchant and the etched material are different than in the case of 30- μm membranes. Thickness dependent variations of track to bulk etch velocity have also been observed in polycrystalline polycarbonate foils [81].

For etching times shorter than 6 minutes, so far no successful deposition was possible for thick templates, therefore, no results are shown for these conditions. For slightly longer etching times of 6.5 minutes, nanowire coverage indicated that a large amount of pores were not yet completely etched though. These observations suggest that the obtainable aspect ratio for cylindrical wires is not as high as in the 30- μm membranes for the used etching conditions. For an identical aspect ratio, cylindrical wires with diameters of 100 nm should be obtainable in thicker membranes. This was not observed, homogeneous nanowire growth was only apparent after etching the membranes for at least 7 minutes. By homogeneously filling the channels by electrodeposition, a replica of the channel is formed. Thereby the indication of deviation from cylindrical shape of the nanochannels was further supported by measurements on fragments of nanowires, which were grown in samples etched for 7 min and exhibited noticeable conical shape for diameters ≥ 100 nm. Slightly differing pore sizes on both sides of the membranes and a slightly biconical shape of the wires for short etching times show the limitations of use of thick membranes as templates for very thin wires.

Nonetheless, it is possible to grow long nanowires with considerably small variations in the nanowire diameters as exemplarily shown in Fig. 4.2. The displayed sample was grown in a 100 μm thick PC membrane, which was etched for 7 min in 6 M NaOH. The length of the marked wire fragment is ≈ 50 μm and larger fragments are rarely observed. For a fragment of this length, which is half

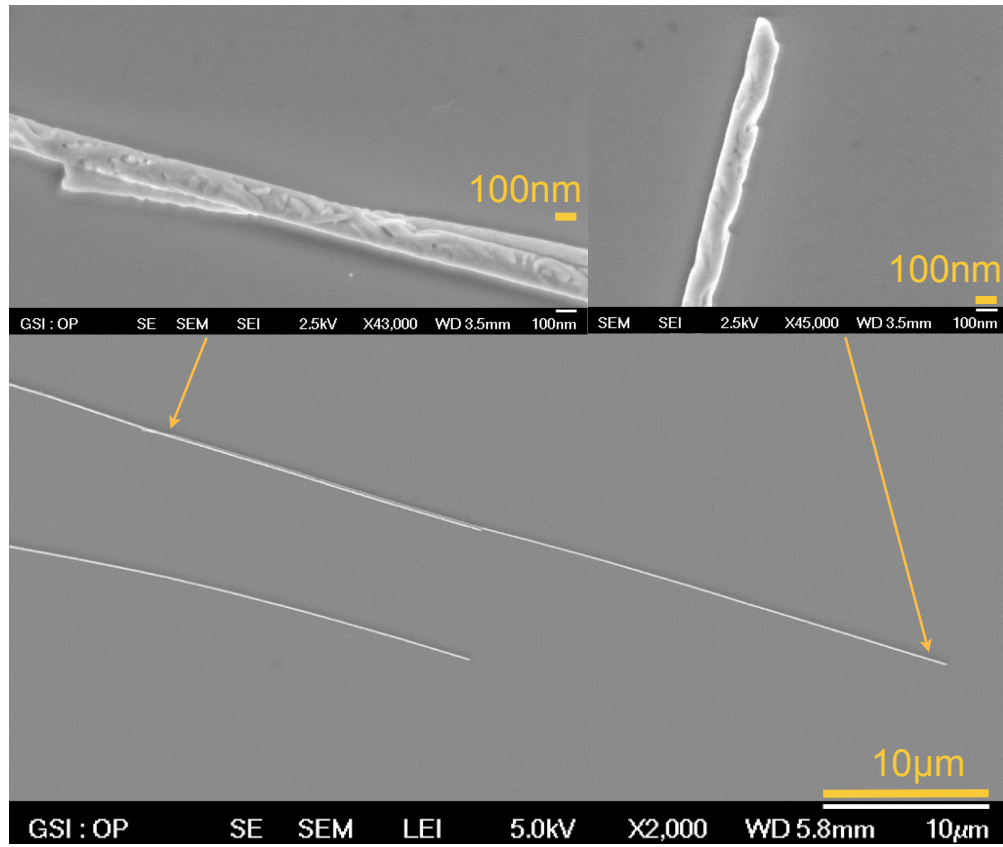


Figure 4.2.: SEM image of a 50 μm long $\text{Bi}_{2+x}\text{Te}_{3-y}$ wire fragment on a Si wafer. The wires with an approximated diameter of 140 nm were grown at -100 mV vs. SCE at RT. An enlarged view on the two tips is shown on top of the overview.

the membrane thickness, a diameter reduction from ≈ 130 nm to ≈ 100 nm was measured. Since wires under the described growth conditions break easily, it is not possible to determine from which segment within the nanochannels the wire fragments originate. Hence, acquisition of larger statistics on the diameter variation along the wires and determination of the average nanowire diameter is not practicable under the present conditions¹.

In comparison, for nanowires in 30- μm polycarbonate membranes, aspect ratios of 1000 have been determined, i.e. wires with a diameter of 30 nm are still cylindrical. With respect to the lowest obtainable diameter, the lower etching threshold for 30 μm thick membranes is 55 s, which resulted in an average diam-

¹Deposition of a less brittle material could be a solution to this problem.

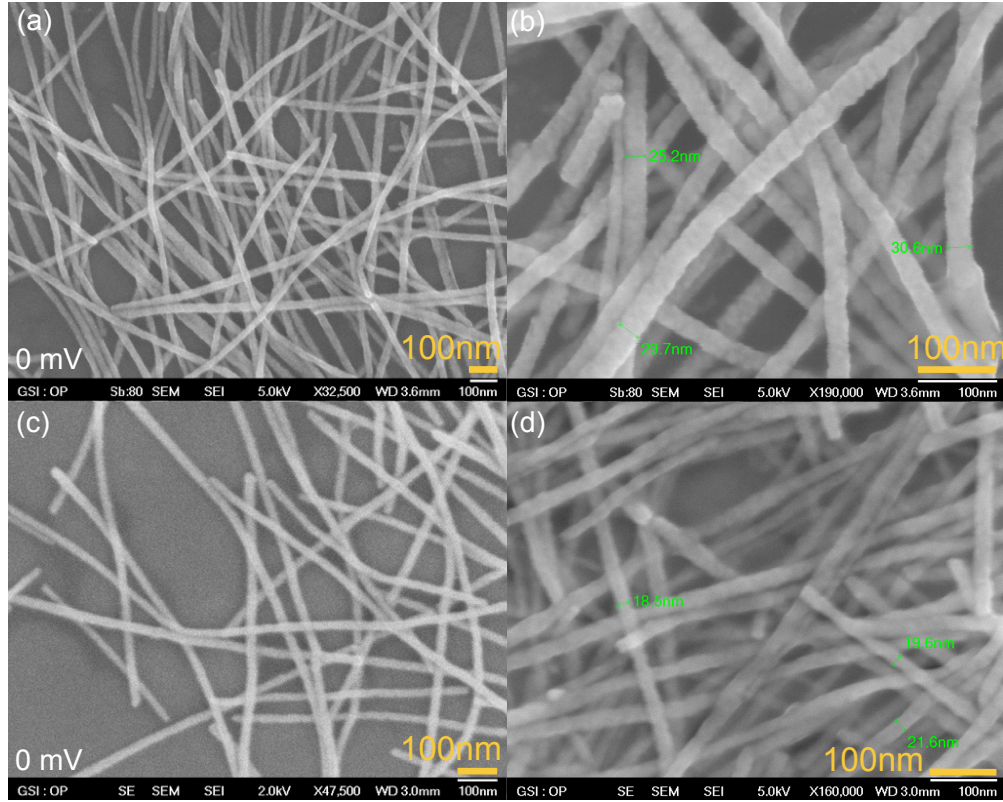


Figure 4.3.: SEM images of $\text{Bi}_{2+x}\text{Te}_{3-y}$ nanowires with the smallest fabricated diameters.

The wires were grown in 10- μm thick ion track-etched polycarbonate membranes. In images (a) and (b), the diameter is found to be ≤ 30 nm. The sample shown in (c) and (d) also exhibited wires with diameters ≤ 20 nm.

eter of 24.3 nm. An increase of the etching time by 15 s has shown to produce pores with diameters of approx. 30 nm, thereby demonstrating the extent of the time window for the fabrication of thin nanowires.

In Fig. 4.3, an additional example for the wide range of possible variation of the nanochannel size is demonstrated, i.e. the present lower limit for the diameters of electrochemically grown Bi_2Te_3 nanowires in ion track-etched polycarbonate membranes. By employing 10 μm thick membranes, it was possible to further reduce the smallest diameters below 20 nm. Due to the presence of polymer residue on the wires, it can be assumed that the actual wire diameters are even smaller by a few nm. However, due to practical considerations, e.g. membrane stability and nanochannel alignment, most investigations were

performed on 30 μm thick membranes. These parameters are especially important for the measurement of embedded nanowires by X-ray Diffraction Analysis (XRD), where the necessity of a fixed geometry is evident.

4.2. Experimental Set-Up for Electrochemical Deposition

The electrochemical deposition of bismuth telluride is performed in potentiostatic mode, and the time transient of the deposition current is monitored. To guarantee the stability of the system, a commercial potentiostat (EG&G Princeton Applied Research Potentiostat Model 263) is employed in combination with a 3-electrode setup including a saturated calomel electrode (SCE)² (cf. Fig. 4.4). Both, the counter electrode and the mechanical support of the working electrode are Pt-disks with diameters of approximately 15 mm, where the active area of the working electrode is specified to 0.95 cm². The electrodes and the sample are mounted in a thermostated glass cell from Radiometer Analytical with a volume of 500 ml. During the electrodeposition, the temperature of the solution is kept constant by water cooling/heating with a Huber ministat, to reduce the influence of temperature fluctuations on the fabrication process. In this 3-electrode setup, the potential between working electrode and a well-defined reference electrode is continuously monitored and kept constant at a predefined value. If not mentioned explicitly, all deposition potentials in this work are given with respect to the SCE reference potential. For optimal conditions, e.g. to minimize ohmic drops, the tip of the reference electrode is positioned as close as possible to the sample, without interfering with the mass transfer in the electrolyte.

Prior to the electrodeposition of the compound, gold was sputtered on the ion-track etched membranes for 3.5 minutes in an argon atmosphere with an Edwards S150B sputter coater. From SEM measurements, it can be seen that the thickness of the contact layer is in the order of 40-50 nm (see Fig.4.5). It can also be concluded from these images, that the sputtering process leads to Au ring electrode formation in the vicinity of the pore mouth. For pore diameters

²Electrode potential : 248 mV vs. normal hydrogen electrode (NHE) at 20°C

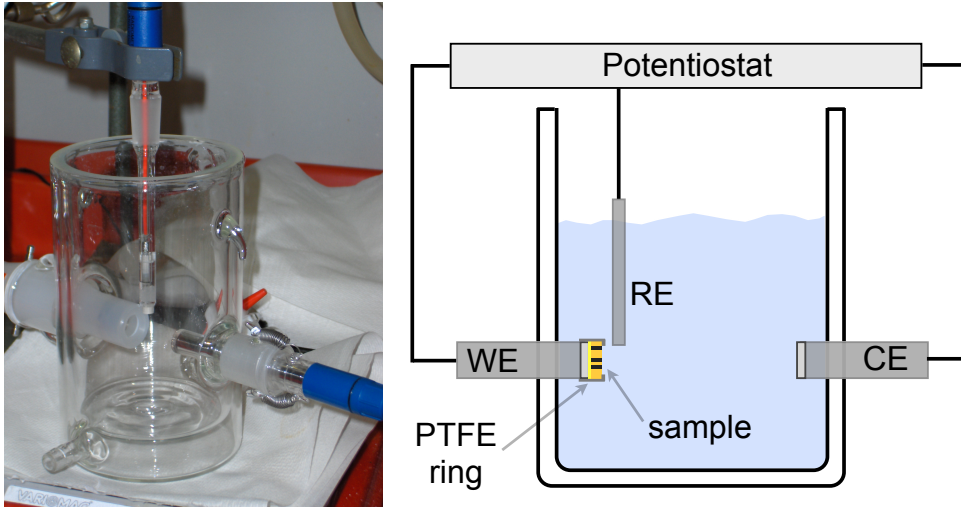


Figure 4.4.: Experimental set-up for the electrochemical deposition (left) and schematic of an electrode set-up (right). The potentiostat keeps the potential between the reference electrode (RE) and the working electrode (WE) constant, while the current between the counter electrode (CE) and WE is monitored. A polymer ring made of PTFE is used to keep the sample fixed and avoid leakage currents.

in the order of 20 nm and larger, the backlayer is not closing the nanopores, but offers a thin, uniform, and nanocrystalline cathode for the electrodeposition.

In previous experiments, this thin Au coating was often stabilized with additional metal layers. This approach has also been tested in the framework of the shown measurements. However, due to the interactions with the electrolyte, a reinforcement of the cathode by electrochemical deposition of Cu has led to the presence of copper impurities in the order of several at% in the deposits. Employing thin-film growth of Au for the stabilization of the template has also not exhibited successful results, because of problems with the homogeneity of the deposition process. The reason for this effect possibly arose from fast growth rates and the formation of cavities between the sputtered and the electrodeposited layer.

One additional experimental setup has been employed to circumvent the deposition on the bare sputter-coated layer. Prior to the etching of the channels, the cathode was prepared and electrochemically reinforced by an additional gold layer in a 2-electrode setup [84–86]. In this case, the deposited layer as well as

the sputtered cathode have a closed surface. Subsequently, the channels were etched from the side opposite to the cathode in the experimental same set-up. Even though it was possible to obtain cylindrical wires in several cases, as shown in sec. 5.1, the ratio of channel diameter and etching time was not sufficiently reproducible for further measurements.

Deposition on the sputtered cathode has led to the best results with respect to the homogeneity of the growth process and the absence of impurities, and was therefore preferred for the nanowire synthesis.

Because single-crystalline growth is enhanced for electrodeposition at elevated temperature for dc-electrodeposition, samples were also prepared at elevated temperatures of 42 and 48°C. With the presence of 1 M HNO_3 in the electrolyte, most of the deposited nanowires have already been dissolved again, before it was possible to take the templates out of the electrochemical cell. During deposition, the samples grew black or grey as normal, but when it was possible to remove them, the samples appeared solely golden, indicating the dissolution of nanowires. Furthermore, the sputtered cathode was not mechanically stable and was easily removable by sprays of distilled water in several samples. Therefore, deposition temperatures were chosen in the range from 4 to 35°C.

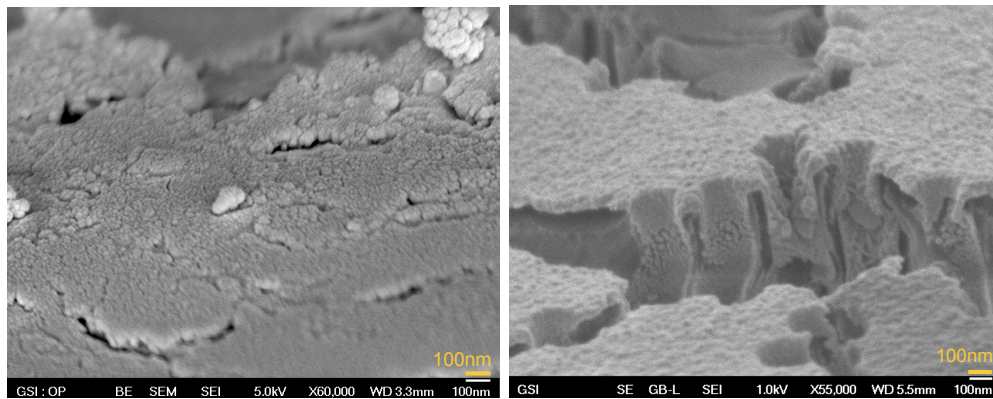


Figure 4.5.: (left) SEM view of a sputtered Au layer. The granular structure of the thin film is clearly visible. (right) Cross-section SEM micrograph of an ion track-etched PC membrane with the sputtered Au contact layer which serves as the cathode in the electrochemical deposition. The gold layer is discontinuous in both cases, caused by stress induced fracture as a result of the preparation procedure for SEM imaging.

4.3. Control of Growth Rates

The process for deposition on recessed nanoelectrodes differs from that for deposition of thin films due to the reduced nanoelectrode surface and the high aspect ratio of the channel [50,91,92,105]. Changes in the diffusion coefficients and concentration gradients towards the cathodes [106] have been published for the electrodeposition of Co nanowire arrays. In addition, it should also be noted that the active area is strongly reduced as compared to film deposition or deposition in AAO. For the employed ion track-etched templates usually around 2% of the surface is covered by pores, in AAO it can be in the order of 70 to 80%.

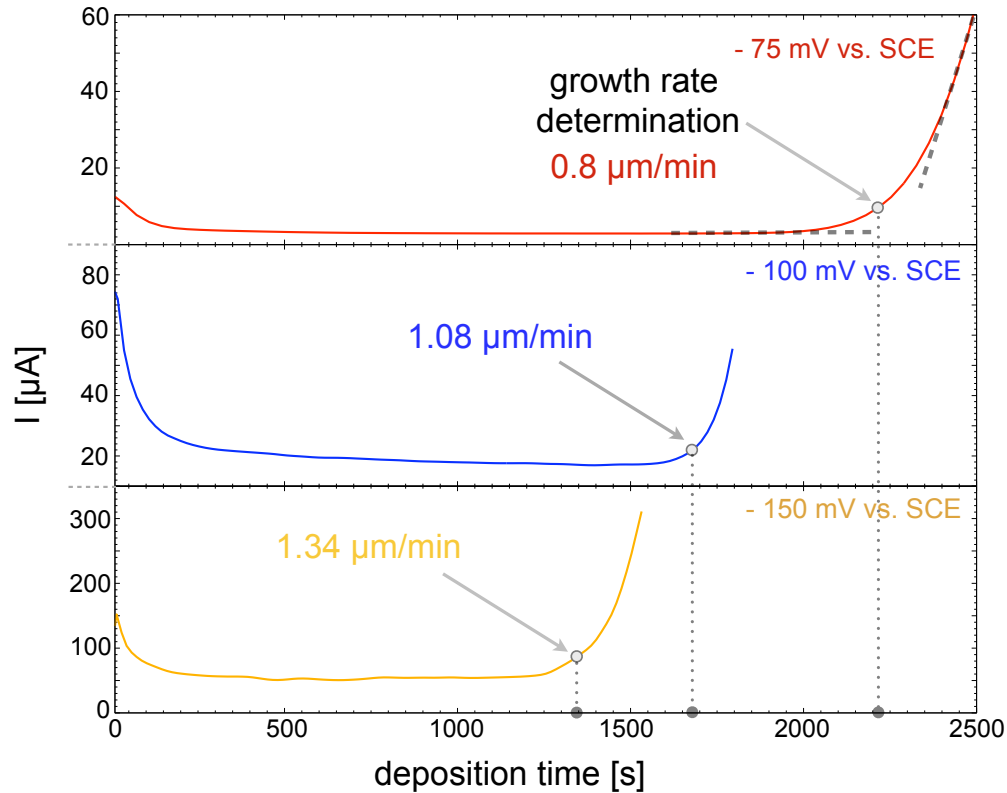


Figure 4.6.: Growth rates in 30- μm thick PC templates with nanochannel diameters lower than 40 nm as a function of the applied potential. The electrolyte concentration was 5 mM Bi and 7.5 mM Te, and all depositions were carried out at room temperature.

The growth rate is calculated as the ratio between the pore length and the time measured for the transition between region (2) and (3) of the nanowire

growth (see Fig. 3.4). This is determined from the onset of the cap growth in the $I-t$ curve, which is visible by an increase of the measured reduction current. Fig. 4.6 shows exemplary deposition curves for nanowires with diameters lower than 40 nm. For determination of the maximum growth velocity, the onset of cap growth is assumed to be half the time difference between the deviation of the measured current from the extrapolated steady state current and the onset where the current increases linearly as a function of time during dominant cap growth. This is schematically depicted by the marked points in the deposition curves. In Fig. 4.6, it can be clearly seen that more negative deposition potentials reduce the duration of the fabrication process. The accuracy for the onset time for cap growth is estimated from repeated experiments with identical growth parameters. From multiple investigation, measurements can be assumed to be reproducible with relative deviations less than 10%. The influence of the electrolyte concentration on the growth velocity of submicron wires (diameter approx. 400 nm) had been evaluated in the early stage of the experiments, i.e. on samples grown on substrates reinforced by copper and gold. Similar growth rates were obtained for the various substrates at an electrolyte concentration of 5 mM Bi and 7.5 mM Te. Fig. 4.7 shows the results for investigated concentrations ranging from 2.5 mMol Bi and 4 mMol Te in 1 M HNO_3 to 20 mMol Bi and 32 mMol Te in 3 M HNO_3 . Because the samples with deposition potential more positive than -75 mV were specifically grown for XRD measurements, the growth process was terminated before the onset of the cap growth was visible. Hence the data points were not included in the discussion, but it should be noted that, in a first approximation, the results are in accordance with the presented findings.

We observe enhanced growth rates with increasing ion concentration and increasingly negative potentials. This indicates that the amount of reduced ions depends on both, the diffusion of ions towards the cathode and also on the applied potential. This tendency is observed independently from the employed electrolyte. In order to maintain comparatively high element concentrations and slower growth rates, and thus reproducible growth conditions, all subsequent experiments were conducted with an electrolyte concentration of 5 mM Bi and 7.5 mM Te in 1 M HNO_3 under thermostated conditions. The HTeO_2^+

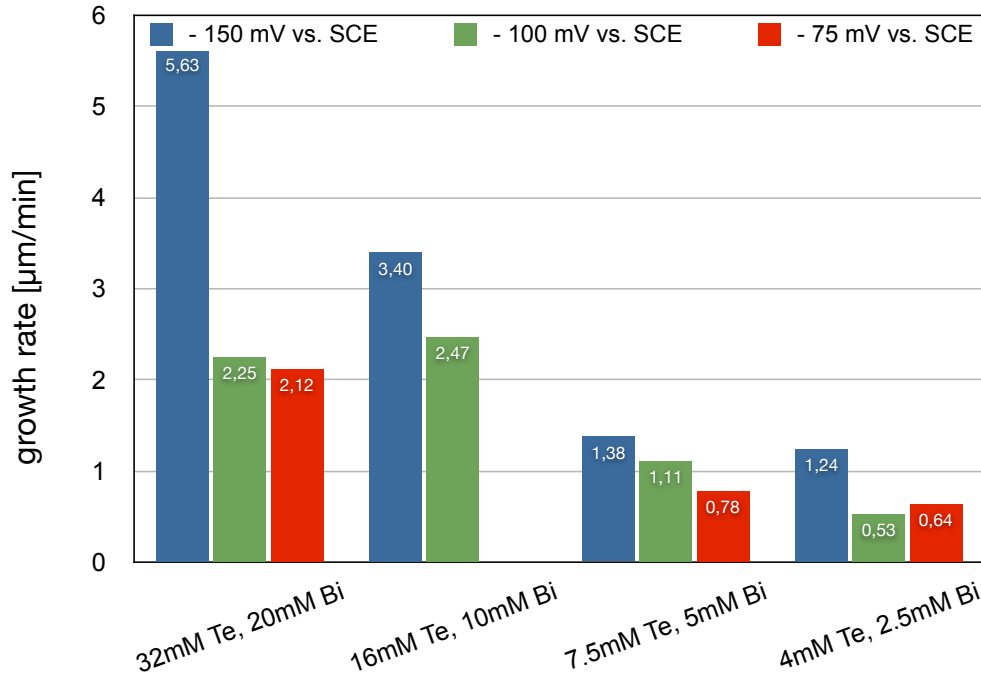


Figure 4.7.: Growth rates in 30- μm thick PC templates as a function of the applied potential and electrolyte concentration. All channel diameters exceed 200 nm.

ions in the solution were obtained by dissolution of TeO_2 in concentrated nitric acid.

Data presented in Tab.4.1 evidences the influence of the channel diameters and the deposition temperature on the growth rates. By direct comparison of the maximum growth rates for different nanochannel diameters, but fixed deposition potential of -100 mV vs. SCE, it can be seen that the channel diameter is not a relevant factor under the given conditions. Temperature on the other hand significantly reduces the observed time until cap growth starts, and is an important factor for the tuning of nanowire properties in dc-electrodeposition.

Recent publications reported on the influence of elevated temperatures which improved the crystallinity of metal nanowires, like Cu [107], Bi [108] and Au [109]. The positive effect of lowered deposition temperature on the crystallinity of bismuth telluride nanowires under pulsed condition and the formation of uniform growth fronts has also been recently demonstrated [59]. Hence, from a practical point of view, not only potential, but also temperature determines

Membrane Thickness [μm]	Pore Diameter [nm]	Growth Rate [$\mu\text{m}/\text{min}$]	
		($T = 4^\circ\text{C}$)	($T = 20^\circ\text{C}$)
30	25	0.65	1.11
30	30	0.72	1.13
30	50	≤ 0.67	1.14
30	250	0.65	1.11

Table 4.1.: Influence of channel diameter and temperature on growth rate for fixed deposition potential of -100 mV vs. SCE. The relative uncertainty of the growth rates is approx. 10 %.

the growth rates in our experiments due to its influence on the diffusion of the ion species. While no impact of the changed diameters is visible in the comparison in Tab. 4.1, a reduction by almost 50% is apparent for the reduction of growth temperature from 20 to 4°C , which is a similar extent as for the pulsed deposition of Bi_2Te_3 in AAO [59]. To demonstrate that the observed growth rate reduction is predominantly due to diffusion and not simply an effect of the temperature dependency of the reference potential, the correlation between temperature T and reference potential E was evaluated for our experimental conditions. According to the equation for the temperature dependence of the potential of a SCE [91],

$$E = 0.2412 - 6.61 \cdot 10^{-4}(T - 25) - 1.75 \cdot 10^{-6}(T - 25)^2 - 9 \cdot 10^{-10}(T - 25)^3,$$

a temperature reduction by 15°C should yield an approximative shift of the reference potential by $+14\text{ mV}$, under the assumption that the reference electrode is in full thermal equilibrium with the solution. Since the temperature of the reference electrode cannot be precisely determined, the potentials were not corrected with respect to temperature and, thus, small temperature dependent variations of the reference potential are possible. A comparison of the temperature related variation of the growth rates (Tab. 4.1) with the potential induced changes (Fig. 4.7) shows that the temperature influence is more pronounced than a potential shift by 14 mV . In addition, the growth rates were determined for the Bi_2Te_3 deposition in membranes with thicknesses of 60 and

100 μm and pore openings of 140 to 180 nm. Since the pore diameter has not shown an influence on the growth rates in 30 μm thick membranes, it is possible to compare the value to the observed velocities in thick membranes. The results are shown in Tab. 4.2 and demonstrate that increased nanochannel length alone also lowers the deposition rate significantly. An increase in channel length from 30 to 100 μm leads to a reduction by more than 50 % for both, deposition at 4°C and at room temperature. This tendency is expected for a diffusion controlled process in recessed nanoelectrode arrays.

T_{dep} [°C]	Etching Time [min]	Growth Rate [$\mu\text{m}/\text{min}$]		
		30 μm membrane	60 μm membrane	100 μm membrane
4	7	0.65	-	0.27
20	7	1.11	0.71	0.50

Table 4.2.: Influence of membrane thickness and deposition temperature on growth rate for fixed deposition potential of -100 mV vs. SCE. The relative uncertainty of the growth rates is approx. 10 %.

Under the given growth conditions, growth rates exceed the values obtained for Bi_2Te_3 deposition in AAO membranes. Pulsed electrodeposition [59]³ in 75- μm membranes at low temperatures has shown to exhibit growth rates as low as 0.045 $\mu\text{m}/\text{min}$. At similar temperatures and for 60- μm AAO membranes, slightly lower concentrations (2.5 mM Bi and 3.3 mM Te) in a dc-growth process have exhibited velocities of the order of 0.03 $\mu\text{m}/\text{min}$. This corroborates the fact that the channel length is also an interesting parameter, which could be vital in the comparison of results obtained by electrodeposition in different templates.

4.4. Determination of Filling Ratios

In order to determine the influence of the prolonged deposition times, by reduction of the deposition temperature, the fraction of the filled pore volume f_V was exemplarily estimated on several samples. This consideration can offer

³The ratio of 'active' to 'relaxation' potential was 1:2.

some insight in the efficiency of the deposition and the influence of deposition parameters on the growth process.

By considering Faraday's law [89] and assuming the synthesis of stoichiometric Bi_2Te_3 nanowires, it is possible to determine the amount of deposited material by evaluation of the accumulated charge during electrochemical wire growth. For the given compound system, deposition potential and temperature are likely to influence the composition of the deposited semiconductor. Hence, the determination of the filling ratios is accompanied by indefinite accuracy, due to the different charge states of the Bi^{3+} and HTeO_2^+ ions. Please note that if a change in the deposition conditions would largely change the composition of the deposit, the filling ratios could include large systematic errors. However, since indications on large compositional changes are found neither in literature nor in our measurements, it is always assumed that Bi_2Te_3 was formed and deviations from this equilibrium concentration have only minor influence on the determined values. The amount of deposited material in mole N is given by

$$N = \frac{Q}{n_{\text{dep}} \cdot F} = \frac{\int I dt}{n_{\text{dep}} \cdot F}, \quad (4.1)$$

where Q is the charge calculated from the integration over the measured deposition current and $n_{\text{dep}} \cdot F$ is the charge equivalent to 1 M of the deposit. F is the Faraday constant (96485.3 C/mol), and n_{dep} is the amount of electrons associated with the reduction of the ions, which is 18 for the deposition of Bi_2Te_3 (see equ. 3.8). The volume per mole of bismuth telluride V_{mole} is determined from the molar mass and the mass density of Bi_2Te_3 and amounts to $10^4 \text{ cm}^3/\text{mol}$. The filling fraction of the pore volume is given by the ratio of the experimentally determined volume of the deposit V and the theoretical maximum volume V_{pores} occupied by etched nanochannels :

$$f_V = \frac{V}{V_{\text{pores}}} = \frac{Q \cdot V_{\text{mole}}}{n_{\text{dep}} \cdot F} \cdot \frac{1}{\Phi \cdot A_{\text{dep}} \cdot \left(\frac{1}{4}\pi d_{\text{nw}}^2 \cdot t_{\text{M}}\right)}. \quad (4.2)$$

The amount of nanochannels is given by the ion fluence Φ and the area exposed to the electrolyte A_{dep} . The volume of the single channel is determined by the membrane thickness t_{M} and the pore/nanowire diameter d_{nw} .

Since f_V depends on many different experimental parameters, it is of more use to compare the influence of the deposition temperature on the determined charge for specific samples, where the templates underwent identical preparation steps in parallel, i.e. ion irradiation and etching. In that case, variations due to inhomogeneity of the ion beam, ion fluence, membrane thickness and active area for electrodeposition can be neglected. Tab. 4.3 presents a comparison of the deposited charges and the estimated filled fraction of the total pore volume. From the presented data, it can be deduced that by reducing the deposition temperature to 4°C, a tendency to improved filling of the polycarbonate membranes is visible.

The comparison of the deposited charge in thicker templates indicates an opposite trend. With respect to the determined filling ratios, it is necessary to consider the percentage of pores in which nucleation and subsequent nanowire growth occurs. Otherwise it is difficult to elaborate the homogeneity of nanowire growth in the given samples. For larger pore diameters, first exemplary measurements were undertaken to determine the percentage of pores in which nucleation occurs, by taking advantage of the sputtered cathode used for electrodeposition. As shown before, the cathode is not covering the nanochannels, hence the pore opening that is linked to the ring electrode for electrodeposition, is still visible in SEM. The idea is to use the electron beam to ionize atoms within the channels and analyze the emitted x-rays by energy dispersive x-ray analysis (EDX). If nucleation took place at the cathode, signals from Bi and Te will be visible in the EDX-Spectra. Since EDX spectra are always obtained from the excitation of a volume that is larger than the point resolution of the exciting electron beam, low acceleration voltages are used for the electrons. Thereby it is possible to keep the excited volume within the nanowire-polymer composite to a minimum. It is assumed that the electron beam is focused to the middle of a nanochannel. For excitation with 8 keV electrons, the width of the excited volume in elemental Te is approx. 120 nm⁴, hence only the Bi and Te in the wires or the gold on the channel walls should be excited for well separated channels.

An example of this measurement procedure is shown in Fig. 4.8 for two pore openings on the Au cathode. EDX analysis suggests that nucleation of Bi₂Te₃

⁴This value would be lower under the assumption of the denser bismuth telluride.

E_{dep} [mV vs. SCE]	d_{nw} [nm]	Q (20°C) [C]	Q (4°C) [C]	f_V (20°C) [%]	f_V (4°C) [%]
30 μm thick membrane					
- 100	24.3	0.035	0.054	14.76	22.77
- 75	29	0.088	0.110	24.35	32.57
- 100	30	0.073	0.074	20.20	20.47
- 100	245	0.520	0.740	21.97	32.12
60 μm thick membrane					
- 100	-	0.516	0.353	-	-
100 μm thick membrane					
- 100	-	0.546	0.378	-	-

Table 4.3.: Deposited charge Q in different membranes with the given pore openings and estimated percentage of filled volume fraction f_V for electrodeposition at 4 and 20°C. Due to slight variations in the channel diameter in thicker membranes, only the deposited charge is given.

only took place on one of the ring cathodes. This shows that, despite their spatial proximity, signals were separable and stray radiation can be omitted. Comparative measurements were made for the two 100 μm thick samples, where the deposited charge for room temperature deposition was found to be higher than for low temperature deposition (Tab.4.3). For the sample deposited at 4°C, only 22% of the pores exhibited clear presence of Te, while for the sample grown at room temperature, this fraction was estimated to 63%.

For the given samples, this indicates that even though lower charge was deposited in total for lower deposition temperature, the pores are more homogeneously filled, since a significantly lower percentage of pores exhibit signs of nanowire growth. It is suggested that the percentage of nanochannels in which nucleation takes place can be an important factor for the determination of the homogeneity of the deposition process. For future measurements, a suitable technique should be employed to assess a larger variety of growth conditions, including smaller wire diameters and higher pore densities.

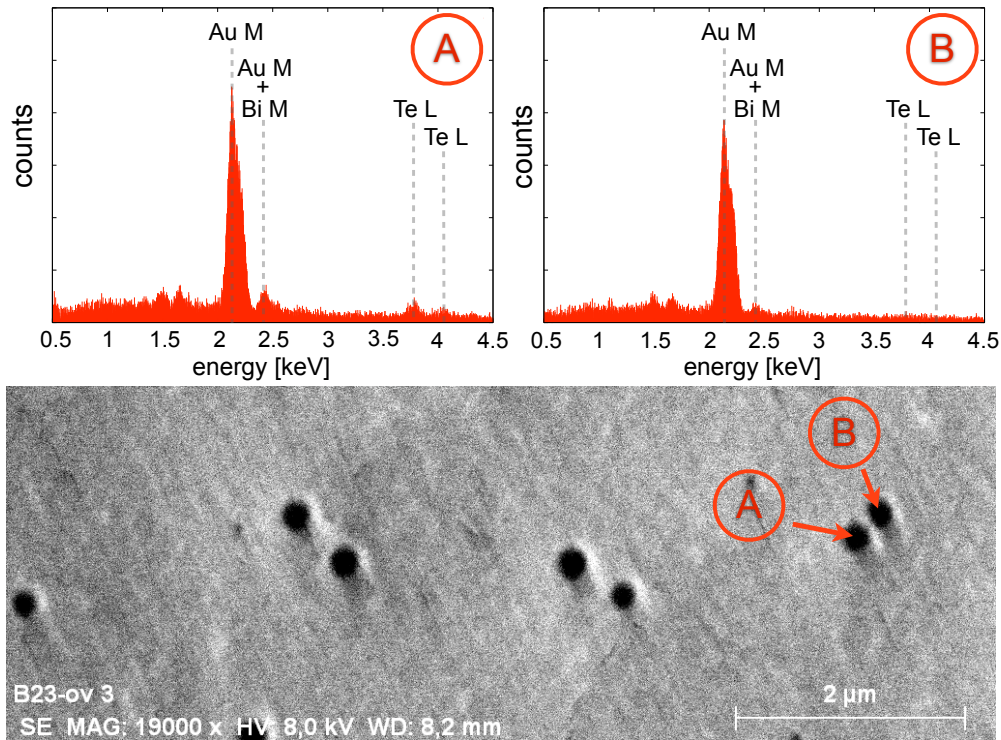


Figure 4.8.: Comparison of EDX-spectra obtained on two separate pores on the sputtered *Au* cathode of a 100-μm membrane, which was etched for 7 min. EDX on pore B did not reveal any indications of the presence of Bi_2Te_3 , while pore A exhibits traces of Bi_2Te_3 . With the employed settings no stray signal from nanowires in neighboring channels was visible.

Conclusions

Dependent on the potential field of application of the grown Bi_2Te_3 nanowires, polycarbonate foils of various thickness (10, 30, 60 and 100 μm) were prepared as templates by heavy ion irradiation and subsequent etching in NaOH. The correlation between the etching times and the observed pore diameters was presented in this chapter.

Under identical preparation conditions, pore openings in thicker membranes have exhibited lower diameters than the 30-μm membranes. The reasons for this behaviour are under investigation.

From SEM measurements on long nanowires and wire fragments, it is evident

that the present etching conditions are not yet adjusted to obtain strictly cylindrical wires, while cylindrical wires with aspect ratios of 1000 are known to be feasible in 30- μm membranes. Due to their slightly conical shape, aspect ratios were not yet determined for long wires, but can be assumed lower than for wires grown in thin membranes.

Electrochemical deposition from nitric acid based Bi_2Te_3 electrolytes was successfully performed in membranes of all thicknesses. Synthesis with diameters below 30 nm are possible in 30- μm templates, while deposition in thick membranes (60 and 100 μm thickness) was only successfully conducted in templates with minimum pore openings of approx. 140-180 nm.

From the determination of the onset of cap growth in the $I-t$ curves of the electrochemical deposition, it was possible to investigate the influence of the various deposition parameters on the growth process. Reduced ion concentrations in the electrolyte, as well as reduced deposition potentials were suitable means to lower the growth rates significantly. A reduction was also observed, when fixed growth conditions were employed and only the channel length was increased by changing the membrane thickness. An increase from 30 to 100 μm , which is a common length for AAO membranes, has exhibited growth rate reduction as large as 50% for both, deposition at RT and 4°C. Furthermore, a reduction of approx. 40% was realised by lowering the deposition temperature to 4°C in thin templates. This has shown beneficial influence on the efficiency of the synthesis, which was evaluated in the form of the filled volume fraction. This value was estimated from the deposited charge and the theoretically available maximum nanochannel volume. Lowered temperature prolongs the growth process by reduction of the ion diffusion and has shown to enhance the percentage of filled volume.

5. Morphology and Structure

As presented in the sections on Bi_2Te_3 bulk material and nanowires, as well as the considerations on the influence of the various material-specific properties, e.g. anisotropy in electrical and thermal conductivity or enhanced phonon scattering by low-dimensionality, on ZT , morphological and structural properties of Bi_2Te_3 are of great importance for the enhancement of the thermoelectric properties. In order to elaborate the influence of deposition parameters on morphology, high resolution scanning electron microscopy (HR-SEM) was employed to characterize the surface roughness of nanowires and the texture of caps. For the determination of preferential orientation of embedded electrodeposited nanowires and to establish a correlation to the observed morphological changes, X-ray diffraction (XRD) was employed. Finally, single nanowires with small diameters were analyzed by means of high resolution transmission electron microscopy (HRTEM), with respect to crystallinity, morphology, and identification of interplanar spacings, to validate the formation of Bi_2Te_3 nanowires.

5.1. Scanning Electron Microscopy

Scanning Electron Microscopy (SEM) is used to determine the nanowire diameters and the influence of various deposition parameters on the nanowire morphology. Further, SEM allowed the investigation of systematic changes in the appearance of the nanowire caps. Depending on the deposition conditions, growth rates as well as the morphological appearance of the nanowires and caps can change significantly. The impact of the deposition conditions is demonstrated on samples that were grown with an ion concentration of 5 mM Bi and 7.5 mM Te, where the Te content was prepared from oxidation of pure Te powder. The employed templates were prepared by etching from one side, as described

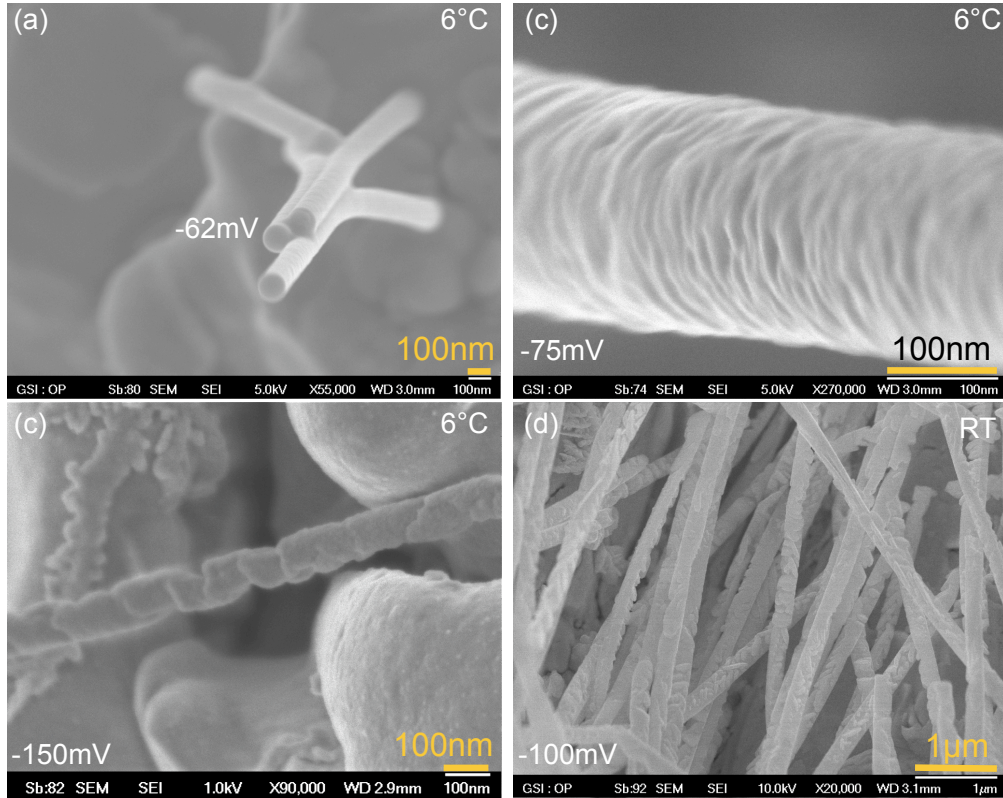


Figure 5.1.: Observation of increased surface roughness for low-diameter $\text{Bi}_{2+x}\text{Te}_{3-y}$ nanowires by potential variations in low-temperature electrodeposition at 6°C ((a) and (b)) and influence of the temperature and potential on deposition in larger channels ((c) and (d)).

in sec.4.2. Fig.5.1 shows the influence of the deposition potential for wires with diameters below 100 nm ((a) and (b)). While nanowires are cylindrical and exhibit a smooth surface for deposition at -62 mV at 6°C , an increasingly negative deposition potential of -150 mV leads to an enhancement of the surface roughness, and the corresponding nanowires appear to consist of a set of barely connected grains. Even the lowered growth rate observed in low-temperature deposition can not compensate the influence of the applied potential. For wires with larger diameters of ca. 200 – 300 nm, the influence of temperature is clearly demonstrated for deposition at -75 mV and -100 mV in Fig.5.1 (c) and (d). At -75 mV vs SCE, the reduction of the fabrication temperature leads to a smooth wire morphology. The roughness of the wires is also increased at more negative potentials and higher growth rates, as shown in Fig.5.1 (d). For the given elec-

trochemical system, the modification of the nanowire surface roughness is found to be possible by variation of the potential and temperature.

In the case of cap morphology, samples were grown with an electrolyte with the same concentrations. The Te concentration of 7.5 mM in the electrolyte was obtained from dissolution of TeO_2 . Fig. 5.2 displays the influence of the deposition potential on nanowire caps. The dominant morphologies are shown with corresponding deposition parameters. Fig. 5.2 (a) - (c) shows caps grown on top of nanowires with diameters ≤ 30 nm, the morphology of the nanowires was also investigated by HRTEM (see sect. 5.3). For these cap sizes ≤ 10 μm , the observed shape is similar for varied potentials. A distinct texture is only indicated for deposition at -150 mV, where several grains appear to have a square base area. This could result from overgrowth of more textured caps, as the one shown in Fig. 5.2 (f). Fig. 5.2 (d) - (f) gives examples of caps on nanowires with diameters ≥ 140 nm. Clear differences in the structure of the cap surface are visible for caps with sizes ≥ 10 μm . This is in accordance with the observation of the surface structure of the nanowires in Fig. 5.1. A transition in the morphology seems to be present at approx. -75 mV in combination with a reduced deposition temperature. The cap and nanowire roughness is reduced for less negative potentials, while more negative potentials yield rough nanowires and strongly textured caps. A similar tendency was reported for the behavior of electrodeposited thin films [26, 100]. In the work of Michel et al. [26], electrodeposition at -40 mV vs. SCE led to smooth Te-rich deposits, while deposition at -100 mV vs. SCE exhibited rough Bi-rich films. Tittes et al. [97] also found a correlation between morphology and elemental composition, however they reported rough Te-composites and smooth Bi-rich compounds.

Fig. 5.3 shows caps grown on wires with large diameters ≥ 140 nm. From the shown caps it can be deduced, that for increasing cap size, the original texture might become masked due to the different diffusion regime on top of the membranes, as compared to the ion mass flow within the pores. If crystallinity of the wires is reflected in the morphology of the caps, their size should hence be chosen as small as possible, where variations in the growth process due to change in the different contributions of charge supply (migration, convection, and diffusion) are not pronounced.

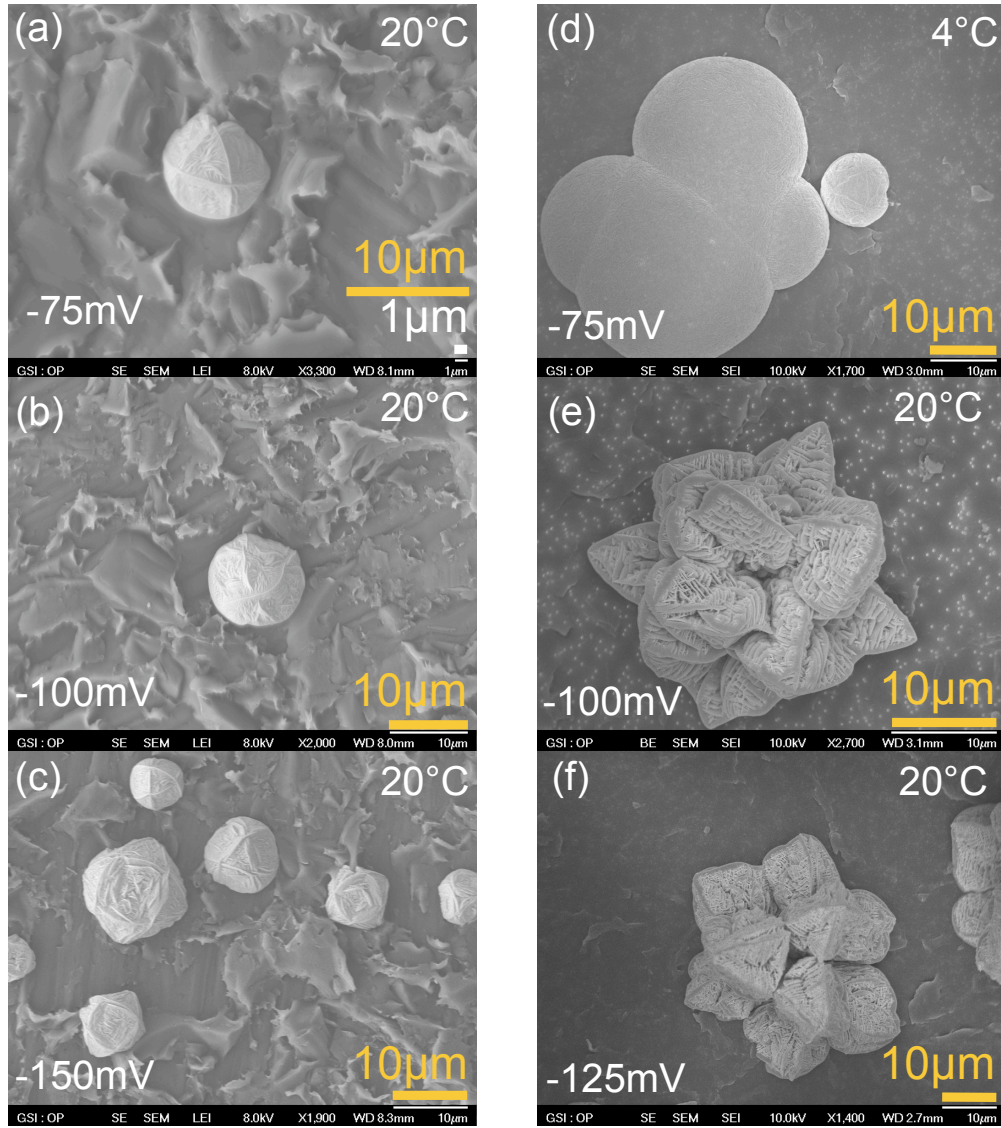


Figure 5.2.: Dominant cap morphologies for several samples grown under the given deposition conditions. In (a) to (c) the nanowire diameters were ≈ 40 nm, in (d) to (f) the pore opening diameter was ≥ 140 nm.

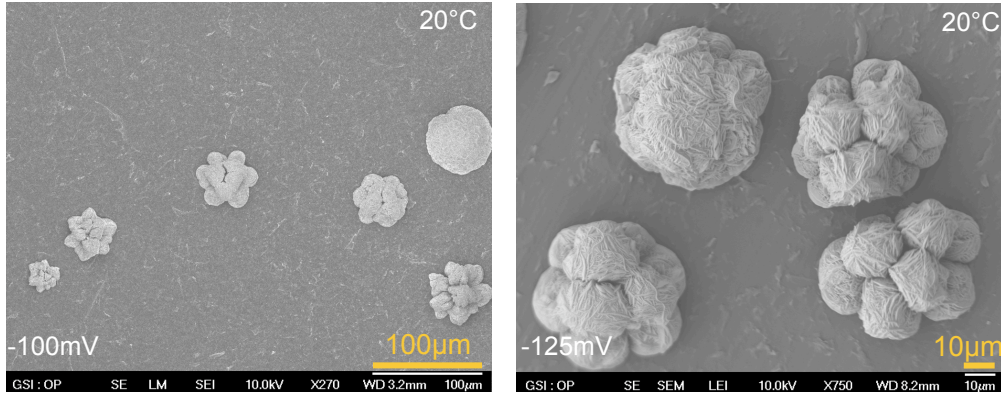


Figure 5.3.: SEM images indicating the change of cap morphology with increasing size under the given electrochemical deposition conditions. The size of the pore openings was ≥ 140 nm. Dominant cap morphologies for several samples grown under the given deposition conditions. With increasing size, strong texture is no longer observed.

Morphological differences in nanowires and caps are potential- and probably size-dependent. In combination with the established correlation between film roughness and elemental composition [26, 93, 100], SEM measurements indicate that the chosen deposition conditions could offer the controlled growth of either Bi-rich or Bi-deficient Bi_2Te_3 . Since the diffusion of Bi^{3+} is assumed to be the limiting contribution to the growth of Bi_2Te_3 [50, 93], the potential dependent ratio of the ion concentrations at the electrolyte-cathode interface is likely to be also related to the transition from smooth to rough nanowires, in analogy to thin-film growth. The onset of this transition could hence be tuned by variation of the Bi concentration in the electrolyte. The change of the composition of 200-nm diameter nanowire arrays as a function of the ion concentration has been demonstrated by Wang et al. [50] for deposition at a fixed potential. The morphology was neither analyzed in detail nor compared to observations of thin films. However, they reported on increased surface roughness of deposits grown at negative potentials ≤ -200 mV and found that the change of deposition potential was linked to an increase of the Bi content and the formation of Bi-rich wires. Comparative XRD measurements showed that Bi-rich rough wire arrays showed preferential (015) reflexes, while for Te-rich compounds wires, the (110) reflex was dominant. Similar observations have also been made from measurements on electrodeposited thin films [101, 102],

where increasingly negative potentials have additionally shown the transition from n- to p-type conductivity. In case that the correlation between structure and composition does not hold for smaller nanochannel diameters, changed deposition conditions still allow for selective variation of morphology, which alone can be of considerable value to the tunability of scattering processes of charge carriers, as well as phonons [4, 5, 8, 40, 41].

5.2. X-Ray Diffraction

To avoid the influence of caps on the diffractograms of embedded nanowires, the deposition process was interrupted when indications of cap growth, i.e. increased currents, became visible in the recorded $I - t$ transients. In XRD, monochromatic X-rays are diffracted from crystal lattice planes according to Bragg's Law (see Fig. 5.4 (left))

$$2d_{hkl} \cdot \sin \theta = n \cdot \lambda \quad (5.1)$$

with d_{hkl} being the distance of adjacent lattice planes, h, k, l the Miller indices, θ the diffraction angle, λ the wavelength of the x-rays, and n an integer. For fixed wavelength, it can be directly seen, that the diffraction angles are a function of the crystal orientation and interatomic distances. The wavelengths of the employed X-rays are $K_{\alpha 1}$ ($\lambda = 1.788965 \text{ \AA}$), $K_{\alpha 2}$ ($\lambda = 1.79285 \text{ \AA}$) for Co anodes and $K_{\alpha 1}$ ($\lambda = 1.54060 \text{ \AA}$), $K_{\alpha 2}$ ($\lambda = 1.54443 \text{ \AA}$) for Cu anodes. Measurements with Co K_{α} radiation were made on a STOE four-circle diffractometer with a graphite monochromator at the department of materials and geosciences of the TU Darmstadt, analysis with a HZG 4 diffractometer with Cu K_{α} radiation was performed at GSI. In all cases the $K_{\alpha 2}$ -lines were not eliminated. Since the energy difference between the two X-ray lines is negligible as compared to their total energy, the two lines add up to higher beam intensities, which is very helpful for analysing small volumes, as it is the case in the measured nanowire-polymer-composites. If not explicitly mentioned, diffractograms are scaled to plot diffraction angles according to a measurement with a Co anode. Thus, scans obtained from a Cu anode are scaled accordingly. While peak positions are then comparable for different diffractograms, this is not valid for the peak

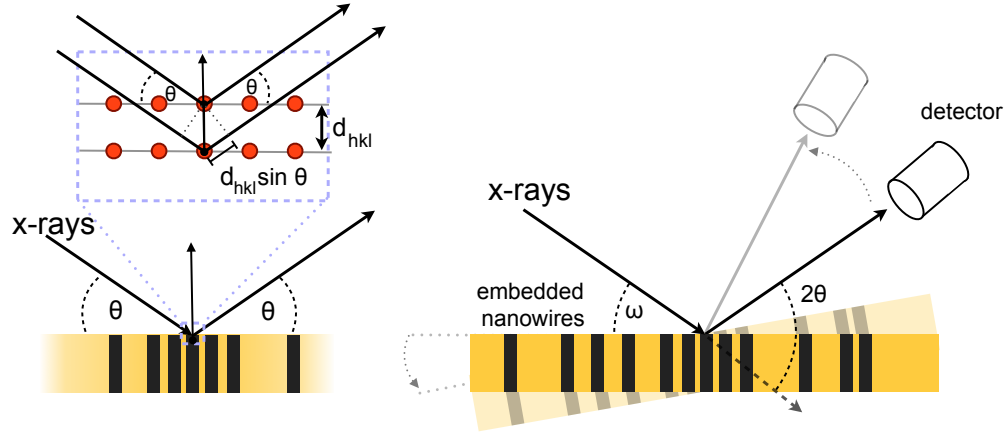


Figure 5.4.: Schematic of Bragg condition for x-ray diffraction measurements (left) and basic set-up for recording an ω - 2θ -diffractogram (right).

intensities. In case $\omega - 2\theta$ -scans were performed with different wavelength, it is mentioned in the context. Furthermore, it should be noted that in the case of the HZG 4, Cu peaks could arise due to stray radiation from the sample holder and coincide with the diffraction on the (205) plane of Bi_2Te_3 . The sample holders in the diffractometer with Co anode do not contain copper, thereby the reflex found at $\approx 59^\circ$ is sample-related. All diffraction measurements were conducted in reflection geometry as depicted in Fig. 5.4. In this configuration, Bragg diffraction occurs on planes which are aligned perpendicular to the wire axis. The corresponding direction in reciprocal space is determined by the orientation of the (hkl) planes and is written as $\langle \text{hkl} \rangle$. For orientation in real space, the exact lattice parameters a, c of the hexagonal cell should be known and the direction would be given by $\left[2h + k, h + 2k, l \frac{3}{2} \left(\frac{a}{c} \right)^2 \right]$. In the case of the (110) plane, the direction in real space is [110]. Since this not easily transferable for the occurring (015) and (205) reflexes, directions are therefore uniformly given by $\langle \text{hkl} \rangle$.

For the X-ray diffraction measurements, the sample is tilted by an angle ω with respect to the incoming X-ray beam, while the detector is moved by an angle of 2θ ($\theta = \omega$) with respect to the transmitted beam. The axis of rotation is perpendicular to the plane spanned by the incoming and the diffracted X-ray beam.

Prior to XRD measurements, the sputtered Au cathode was selectively removed by means of a KI/I₂ etching solution. In few cases, the etchant did not completely dissolve the electrode, hence a potential reflex from the (1010) plane of Bi_{2+x}Te_{3-y} overlaps with a Au peak in the diffractogram and was not considered for the texture discussion. The texture coefficient is given by

$$TC_{(h_i k_i l_i)} = N' \frac{I(h_i k_i l_i) / I_0(h_i k_i l_i)}{\sum_{n=1}^{N'} (I(h_n k_n l_n) / I_0(h_n k_n l_n))} \quad , \quad (5.2)$$

where hkl specify the lattice planes in the notation for the hexagonal lattice, I denotes the measured reflex intensity, I_0 is the normalized reflex intensity in a polycrystalline sample, and N' is the number of considered peaks. For texture coefficient determination, the experimental signal intensity of polycrystalline Bi₂Te₃ from Francombe et al. [25] was considered. For $TC_{hkl} \geq 1$, a preferential orientation of grains is observed within the sample.

The limited scattering volume and orientation of crystallites in the nanowires prevent precise determination of the Bi-Te phase, because the peak positions which most clearly deviate for different phases, exhibit only small peak intensities even in polycrystalline material. An exemplary comparison between a sample with embedded nanowires and powder diffraction patterns for Te [110] and three different Bi-Te phases [111–113] are shown in Fig. 5.5. In addition, the peak positions calculated from the lattice parameters published in [25] are included to demonstrate the influence of variations in the lattice dimensions on the peak positions of bismuth telluride. The shown experimental data corresponds to a sample grown at -100 mV at 4°C with an average nanowire diameter ≥ 200 nm. For all measurements the signal intensities are given in counts per second (cps) on an arbitrary scale. The increasing intensity at low angles is attributed to a broad peak centered around 17°, which originates from the crystallinity of the polycarbonate [70]. Based on the comparison with the powder diffraction data in Fig. 5.5 and the assumption that only one phase is present in the electrodeposited nanowires, the occurrence of pure Te or Bi, and of Bi-rich phases with a Bi to Te ratio ≥ 1 were excluded for the investigated samples.

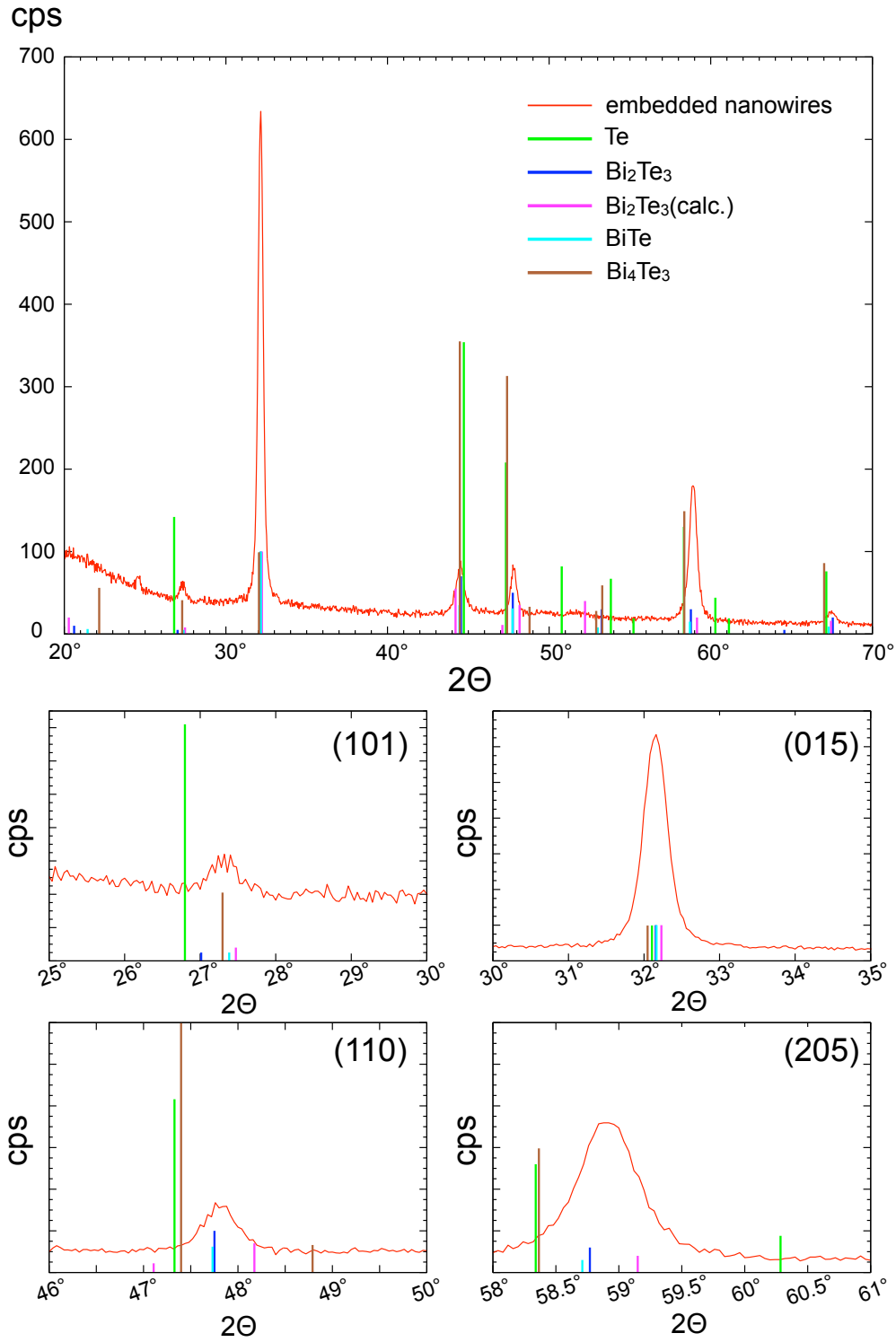


Figure 5.5.: Peak positions and signal intensities of ω - 2θ scans for $\text{Bi}_{2+x}\text{Te}_{3-y}$ nanowires embedded in PC template, Te and various $\text{Bi}_{2+x}\text{Te}_{3-y}$ compounds, including comparative peak positions of tabulated values and calculated peak positions for Bi_2Te_3 with lattice parameters $a = 4.3835 \text{ \AA}$ and $c = 30.487 \text{ \AA}$ [25]. Enlarged views are displayed for the most common peaks visible in diffractograms of different samples, measured with $\text{Co } K_\alpha$.

5.2.1. Membrane Thickness - Influence on Preferential Growth

As has been shown in the section describing the electrodeposition of the nanowires in membranes of various thicknesses, the channel length influences the limiting currents for electrodeposition. XRD investigations help to elaborate to which extent the effect of membrane thickness influences composition and structure of the deposited compound structures. A comparison of diffractograms for nanowires embedded in membranes with different thicknesses is shown in Fig. 5.6. The other sample parameters were chosen identical, e.g. 7 min etching at

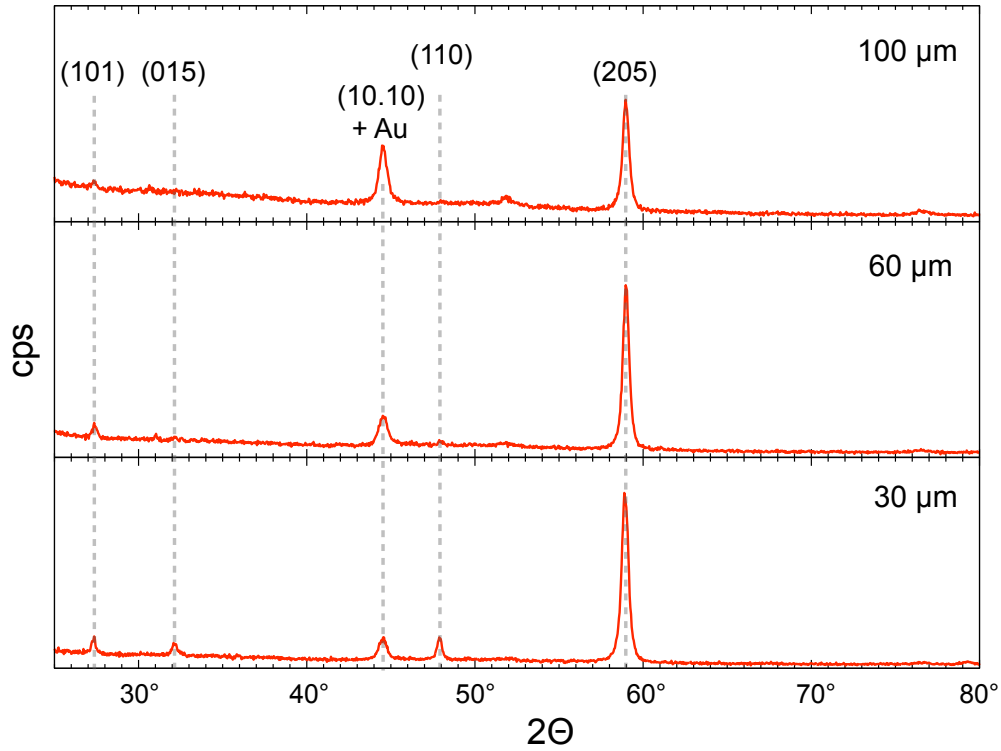


Figure 5.6.: Diffraction patterns for $\text{Bi}_{2+x}\text{Te}_{3-y}$ nanowires embedded in membranes of different thicknesses with comparable channel number densities and diameters. The nanowires were deposited at -100 mV vs. SCE, at RT. The 30- μm thick sample was measured with Cu anode, the angles are transformed to be comparable to the two other samples.

50°C and deposition at -100 mV vs. SCE at RT. Under the given conditions, this yielded pore openings from 140 to 180 nm in the thick membranes and 260 nm for membrane of thickness 30 μm . In all samples the (205) peak is dom-

inant. In powder diffractograms of Bi_2Te_3 , the intensity of this reflex amounts to 30 % [112] or 20 % [25] of the maximum peak intensity of polycrystalline samples. Thus, the samples are preferentially oriented with the (205) planes parallel to the membrane surface. Despite the presence of the Au-peak, the appearance of other reflexes (015) and (110) indicates that for reduced membrane thickness of 30 μm a more polycrystalline growth takes place under the given conditions. Even though the deviation is not very pronounced, it is evident that the growth process is likely to depend on the employed membrane thickness. This can also be seen, when comparing samples deposited at room temperature with an applied potential of -40 mV in 30- μm membranes (see Figs. 5.12 and 5.11) and in a 60- μm membrane (see Fig. 5.9).

While the (205) reflex is clearly dominant in the thicker membrane, deposition in thinner membranes is correlated with a significant reduction of $TC_{(205)}$. The difference between the 60- and 100- μm membranes is not as pronounced as the difference to the thin templates, despite the significantly reduced growth rates.

5.2.2. Channel Diameter - Influence on Preferential Growth

With respect to the observations on variation of nanowire roughness by SEM and TEM, the influence of the nanochannel diameter on crystallinity of electrodeposited wires was conducted. Even though several publications on bismuth telluride nanowires have appeared within recent years, only one research group [55] demonstrated for one fixed potential that the channel diameters in AAO membranes influence the texture of Bi_2Te_3 nanowire arrays.

Since the ratio of bulk to track etching rate also determines the minimum diameter obtainable in ion-track etched membranes, investigations on the influence of the nanochannel diameter were only conducted for 30- μm thick PC. All samples were deposited at -100 mV vs SCE, and the pore openings were 30, 50, and 260 nm for samples grown at RT. For electrochemical deposition at 4°C, the determined diameters were 30, 60, and 260 nm. The results of the ω -2 Θ scans are shown in Fig. 5.7, samples deposited at RT are marked in red, wires grown at 4°C in blue, respectively. From the diffractograms, it is clearly visible that reducing the diameter favors orientations with the (015) planes parallel

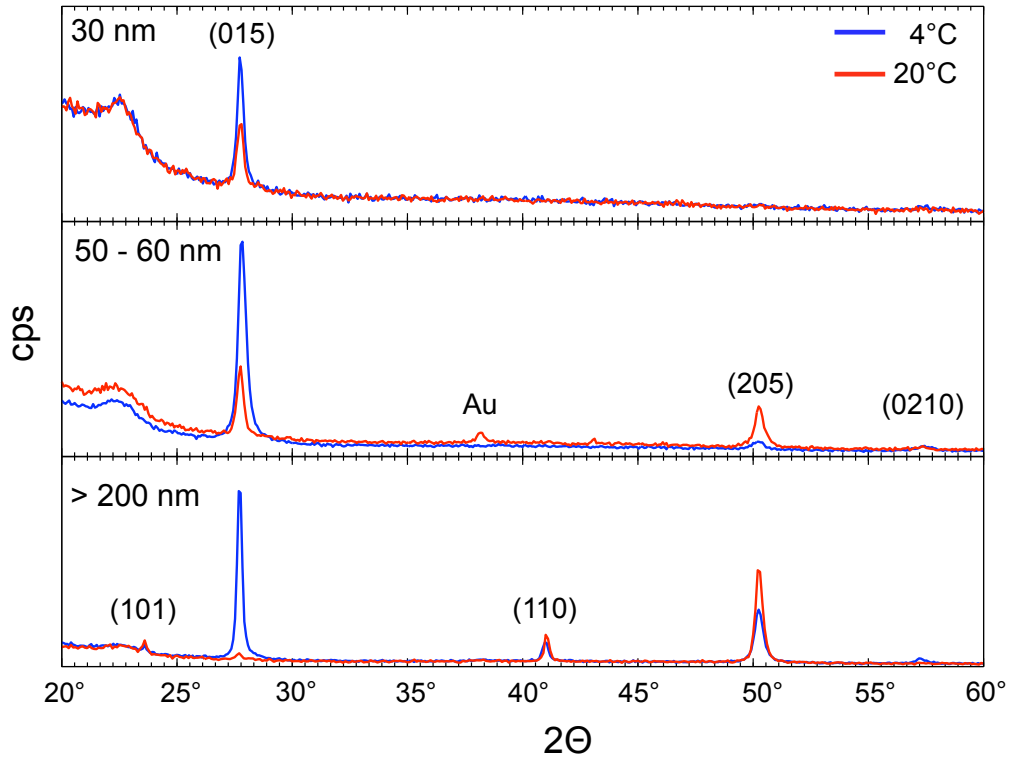


Figure 5.7.: Diffractogram of $\text{Bi}_{2+x}\text{Te}_{3-y}$ nanowires embedded in 30- μm thick polycarbonate membranes. The nanowires were grown at -100 mV vs. SCE at RT (red) and 4°C (blue), respectively. The diameters vary from 30 to 200 nm. ω -2 θ -scans were performed with a Cu anode.

to the membrane surface, because the intensity of the (015) peak is increasing, while the (205) reflex is reduced for smaller diameters. Albeit the (110) and (101) reflexes are observable in nanowires with diameters exceeding 200 nm, the corresponding peaks in the diffractograms vanish for lower diameters. For depositions at 4°C, the influence of the wire diameter is similar to the observed effect for room temperature depositions. However, the favored grain orientation with $\langle 015 \rangle$ texture is already more pronounced at larger diameters than in the case of RT deposition.

For comparison, an additional set of wires was deposited at ± 0 mV vs. SCE. The wire diameters range between 50 and 60 nm for two of the samples, the other embedded arrays exhibit diameters of 140-150 nm. Diffractograms were taken with a setup with a copper anode and are presented in Fig. 5.8. Independently

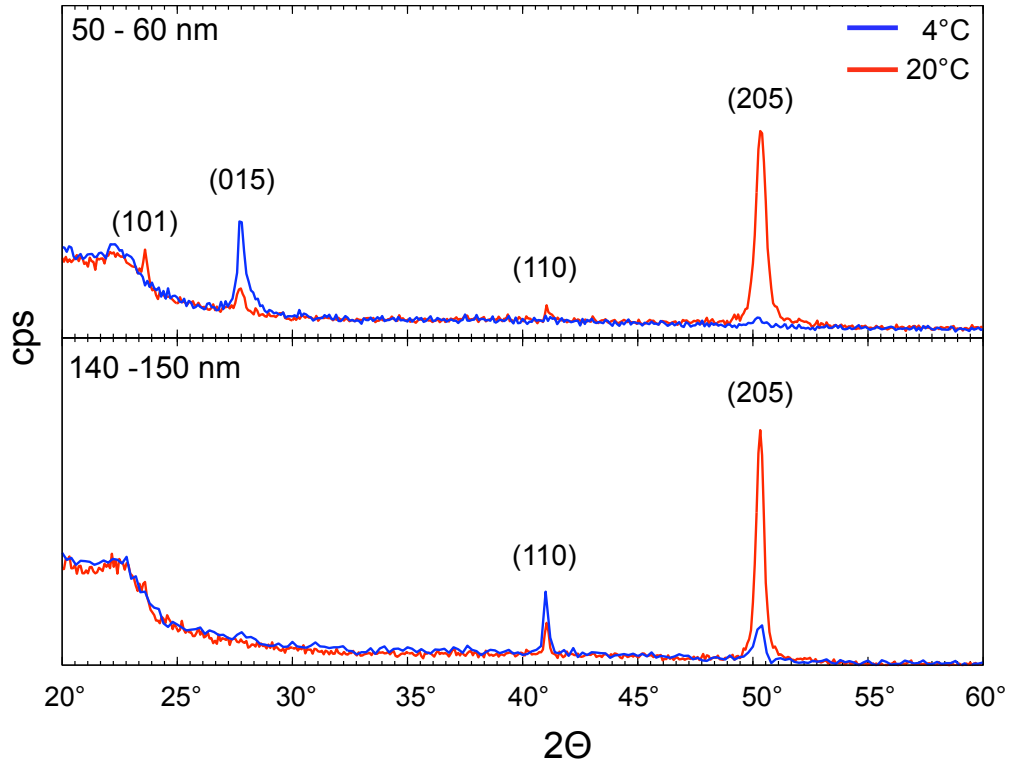


Figure 5.8.: Diffractogram of $\text{Bi}_{2+x}\text{Te}_{3-y}$ nanowires embedded in 30- μm thick polycarbonate membranes. The nanowires were grown at ± 0 mV vs. SCE at RT (red) and 4°C (blue), respectively. Average wire diameters of the respective sets are given in the graph. ω -2 Θ -scans were performed with a Cu anode.

from the growth temperature, thicker nanowires only show signs of the $\langle 015 \rangle$ and $\langle 205 \rangle$ texture in XRD. For thinner wires deposited at room temperature, two more orientations become visible in the diffractograms, the (101) and (015) reflexes appear. Under lowered deposition temperature, all peaks are reduced in intensity, except for the (015) peak which, in comparison, increases in signal strength. In addition, grains with $\langle 205 \rangle$ orientation remain barely visible in the $\omega - 2\Theta$ scan for the embedded array with thin nanowires.

As shown for the wires deposited at -100 mV (Fig. 5.7), growth at ± 0 mV also shows the tendency that smaller diameters favor the $\langle 015 \rangle$ orientation of grains. This influence of the channel diameter indicates that the deposition parameters used for thin films and bulk samples might not be easily transferable to very narrow channels. Preferential orientation of nanowires can be tuned not only by

the deposition conditions, e.g. electrolyte concentration, potential, and growth temperatures, but also as a function of the nanochannel diameter in ion track-etched membranes.

5.2.3. Deposition Temperature - Influence on Preferential Growth

In addition to the shown impact of membrane thickness and nanochannel diameter on the preferential orientation of the nanowire arrays, the influence of the deposition temperature was investigated by XRD. This is of special interest in the context of the effective reduction of the growth rates for low-temperature growth. Fig. 5.9 shows the effect of temperature variation from 4 to 35°C for nanowire arrays electrochemically grown in 60- μm thick membranes at a fixed potential of -40 mV vs. SCE.

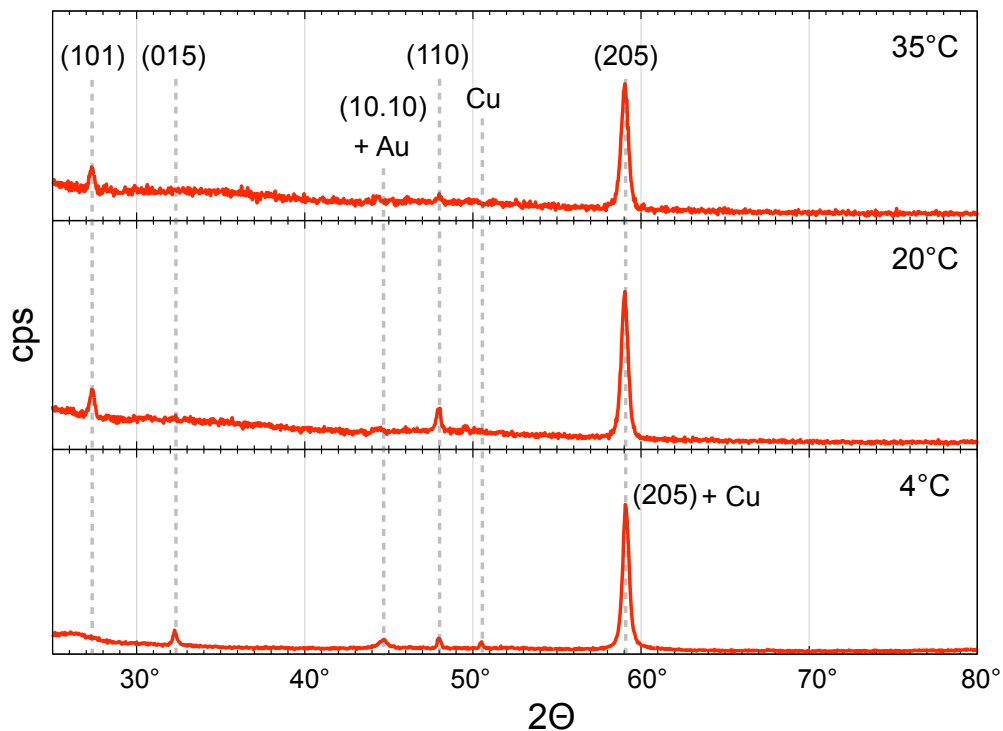


Figure 5.9.: Diffractograms of nanowires embedded in 60- μm thick polycarbonate membranes, electrodeposited at -40 mV vs. SCE. The deposition temperatures were 35, 20, and 4°C, respectively. The pore openings ranged between 140 and 170 nm. Cu K_{α} radiation was employed for the measurement of the latter sample.

The $\omega-2\Theta$ -scan for the sample grown at 4°C was obtained from measurements with Cu anode, so diffraction angles were scaled according to the wavelengths of the x-ray sources as discussed before. As for the previously shown samples, the (205) peak is dominant in all of the samples and the (101) reflex is clearly present for deposition at room temperature as well as 35°C. In both cases, the intensities of the reflexes are higher than expected from polycrystalline samples. A reduction of the deposition temperature from 35°C to 20°C resulted in an increase of the (110) peak, further temperature lowering brought about the appearance of the $\langle 015 \rangle$ texture, whereas reflections from (101) were no longer present. Despite the contribution of the copper sample holder in the last sample, a clear change in texture was observed by lowering the deposition temperature.

In measurements of other sets of samples (see Figs. 5.7 and 5.8), the reduced deposition temperature is correlated with a reduction of the dominant reflex ((205) for thicker wires) and the appearance or enhanced growth of grains with a different texture ($\langle 015 \rangle$ or $\langle 110 \rangle$), indicating that the nanowire crystallinity changes due to deposition temperature variation. A summary of evaluated texture coefficients for wires deposited at either RT or 4°C in 30- μm thick membranes is given in Fig. 5.10. From the shown data, it can be clearly seen, that lowered deposition temperature reduces the $\langle 205 \rangle$ texture for all sets of growth conditions. In addition, either the (015) or the (110) reflex increases in signal intensity in direct comparison. Based on the observation of the temperature dependent texture improvement, rocking curves were taken in addition to the $\omega-2\theta$ -scans, to further investigate the angular dispersion of a specific crystal orientation. Rocking curves are taken with a fixed detector at a diffraction angle θ of specific lattice planes, while χ or ω are varied. χ is the angle that describes the tilt of the sample with respect to the plane spanned by incoming and diffracted X-ray beam for fixed angles ω and Θ . In all cases, very broad peaks with an estimated minimum of the full width at half maximum of 7 – 10° have been found, showing that albeit a preferential growth direction appears to be present, the samples are not single-crystalline, and grains differ slightly in orientation. As compared to previously published results on single-crystalline nanowires, which were electrochemically grown in ion track-etched membranes, sample prepara-

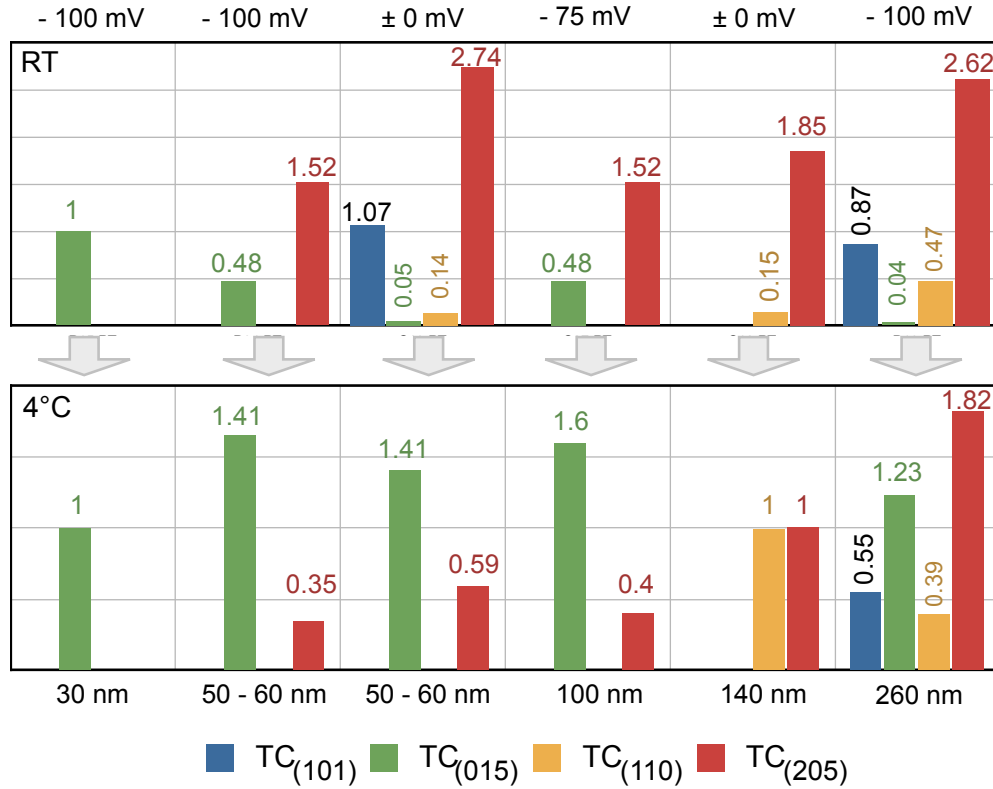


Figure 5.10.: Overview on the influence of lowered deposition temperature on nanowire texture. In the upper part, the extracted texture coefficients for the different orientations are given for deposition at room temperature, the corresponding values for growth at 4°C are shown below. The fabrication conditions, e.g. potentials and nanochannel diameters are noted above and below the histograms, respectively. The number of evaluated peak lines is given by the sum of TC_{hkl} . $TC \leq 1$ indicates less signal intensity than expected from the corresponding lattice plane in a polycrystalline sample.

tion in this work does not include use of an additionally reinforced cathode for increased mechanical stability. Therefore, it can not be excluded, that external stress has influenced the angular dispersion of the observed grain orientations.

5.2.4. Deposition Potential - Influence on Preferential Growth

One of the many advantages of thin film synthesis by electrodeposition is the possibility to easily tune crystallinity and composition of a compound system by adjustment of either the concentration of an electrolyte or the variation of

the deposition potential. In both cases, the different diffusion properties of the ionic species inside the electrolyte are the key for success. As shown in Fig. 5.7, the preferential orientation for deposition at -100 mV is either with the (015) or (205) plane perpendicular to the wire axis. Figs. 5.12 and 5.11 show that applying more positive potentials can lead to a similar effect as lowering the temperature, i.e. a reduction of the (205) reflex in benefit of either the $\langle 015 \rangle$ or $\langle 110 \rangle$ texture.

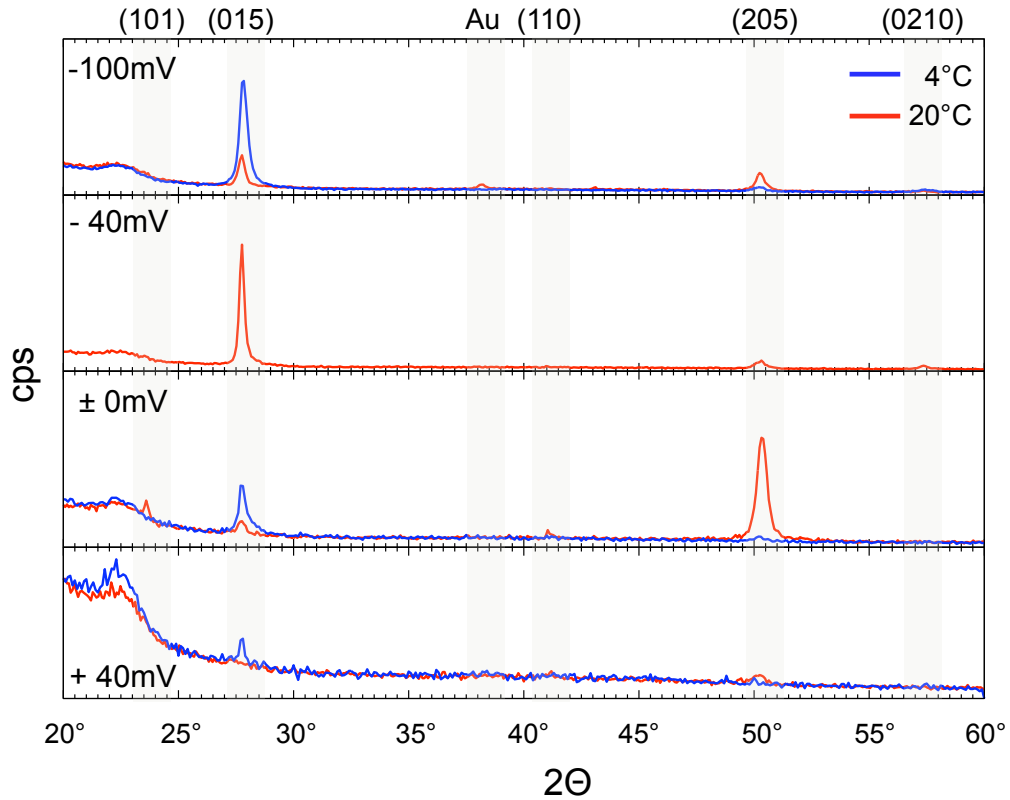


Figure 5.11.: Diffractograms of $\text{Bi}_{2+x}\text{Te}_{3-y}$ nanowires embedded in polycarbonate membranes. Pore diameters range from 50 to 60 nm.

In Fig. 5.11, it is demonstrated that the preferential growth direction of 50-60 nm diameter wires is not changing considerably for potential variation from -100 to -40 mV. $\langle 015 \rangle$ texture occurs throughout the set of employed growth conditions, while deposition temperature reduction yields similar peak intensity ratios as obtained by tuned potential. For the array deposited at ± 0 mV and RT, the (205) reflex is more pronounced again, but different orientations are also

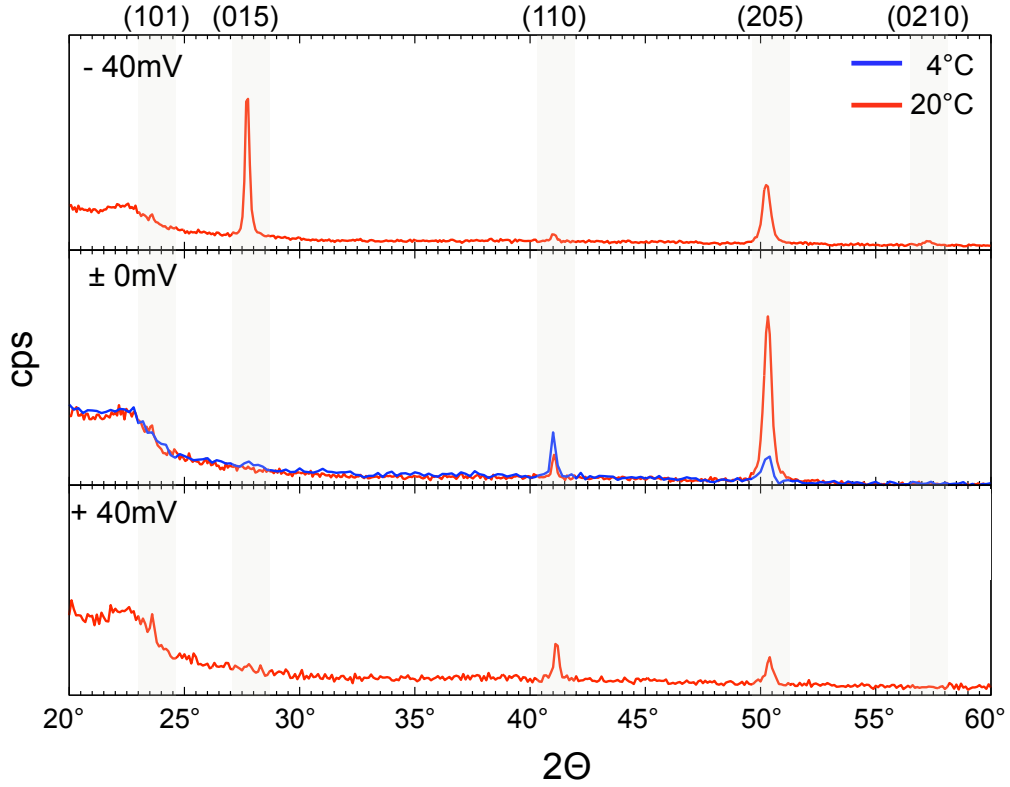


Figure 5.12.: Diffractograms of $\text{Bi}_{2+x}\text{Te}_{3-y}$ nanowires embedded in 30 μm thick polycarbonate membranes. The average nanowire diameters are approx. 140 nm.

present. Lowering the temperature led to the disappearance of the additional (101) and (110) reflexes and the increase of the (015) peak, as readily observed for different samples grown at -100 mV. For samples grown at +40 mV, only small signal intensities were measured, but it can still be seen that the shift to more positive potential results in the appearance of a grain orientation of the (015) planes perpendicular to the wire length for deposition at low temperature. In room temperature growth the (205) peak is only vaguely observed.

Similar observation with respect to the interplay of potential changes and deposition temperature are made for wires with a diameter of 140 nm (cf. Fig. 5.12). Lowering the deposition temperature at 0 mV leads to the reduction of the (205) reflex, while the (110) is increasing in intensity. Similar texture coefficients are observed, when the potential was chosen more positive, i.e. +40 mV vs. SCE. This also brought about an increase of the intensity of the (101) reflex, which was

only barely visible for more negative potentials. Measurement of the samples grown at -40 mV vs. SCE showed the presence of multiple grain orientations, i.e. $\langle 101 \rangle$, $\langle 015 \rangle$, $\langle 110 \rangle$, and $\langle 205 \rangle$. The same set planes is observed at more positive potentials for smaller nanochannel diameters, ± 0 mV for 50 – 60 nm and at more negative potentials for large nanochannel diameters, -100 mV for diameters exceeding 200 nm. This also demonstrates the correlation between the different deposition parameters. The influence of the potential is more obvious for the nanowires with a diameter of 140 nm, because the preferential $\langle 015 \rangle$ orientation for lower potentials is replaced by reflexes from the (110) lattice planes. Additional measurements on the influence of the deposition potential were also conducted for embedded wires with small diameters (30 nm, 30 μ m membrane), where a variation from -100 to -150 mV showed no change in the preferred (015) orientation. Investigations on thick membranes¹ (≈ 140 nm diameter, 60 μ m membrane) corroborate the shown findings on relative peak reduction of the $\langle 205 \rangle$ orientation by variation of the deposition potential. However, unlike for thin wires, the (110) reflex was previously barely visible as an additional orientation at -100 mV. Even though a preferred growth with (110) planes perpendicular to the wire axis was not possible for thin wires, it can be seen that more positive potentials lead to disappearance of the (015) and appearance of the (110) reflex in the diffractograms in larger nanowires. Based on the shown measurements, it is suggested that the potential needs to be more positive for the $\langle 110 \rangle$ orientation to appear in wires with diameters of 50 – 60 nm.

From observations of the influence of temperature and potential on texture, growth rates and the indications on filling ratios, it is proposed that the increased intensity of the (205) reflex with respect to a polycrystalline sample is related to the fast growth rates observed for the deposition in PC membranes in comparison to other templates. However, solely the reduction of the growth velocity by reduced process temperature is not sufficient to explain the decrease in the intensity of the (205) reflex, because it is even further reduced for deposition in thick membranes, yet the (205) peak is dominant for growth at -40 mV, independently from the employed temperature.

The texture in Bi₂Te₃ thin films is known to change with increasing film

¹compare Figs. 5.6 and 5.9

thickness [114]. Therefore, the observed (205) reflex could be an indication of a preferred growth orientation for the first few μm wire length, associated with the use of the sputtered gold cathode under the given deposition conditions. The assumption that the increased growth temperature also increases the fraction of channels in which nanowire growth takes place, would support this idea, because the (205) reflex is mostly dominant in samples grown at room temperature. Deposition at lower temperature could imply fewer nanochannels in which nucleation takes place. In combination with slower growth, this would lead to increased average length, and a reduced (205) signal could be visible in the diffractogram. From this consideration, this orientation could be an indication of homogeneity of the growth process. This assumption is difficult to compare with literature, since mostly thick AAO membranes are employed, which is correlated with a long-time growth process, and different substrates can lead to different preferential orientations in the beginning of the growth. Comparative measurements with different substrates could help to complement these observations. Furthermore, it should be mentioned that this effect is predominantly of importance for deposition in PC templates with larger channel diameters ($\geq 100\text{ nm}$), where lowered deposition temperatures were not sufficient to change the preferential growth direction distinctively. For the sample sets with smaller diameters temperature, reduction leads to $TC_{(015)} \geq 1$, which could not be observed for wires with large diameters.

Grain sizes

In order to investigate whether diameter- and temperature-related changes of the texture are correlated with variations of the average crystallite height, the grain sizes D are determined by means of the Scherrer equation according to

$$D = k \cdot \frac{\lambda_{\text{Co/Cu}}}{\gamma \cdot \cos(\theta)}, \quad (5.3)$$

where λ is the radiation wavelength, k is a grain shape-specific constant (0.94), and γ is the full width at half-maximum of the diffraction peak at 2θ . The FWHM is quadratically corrected for the influence of the experimental set-up,

$\Delta\gamma = 0.18^\circ$ at $2\theta \approx 59^\circ$ for measurements with the Co anode. For the measurements on the HZG 4, peak broadening due to the diffractometer geometry was determined with polycrystalline Si with large grains. The value of $\Delta\gamma$ was found to vary between 0.08° to 0.1° depending on the diffraction angle. The overview of the determined grain sizes is given in Tab. 5.1 for samples grown at -100 mV vs. SCE and arrays deposited in thick membranes.

30 μm membrane						
wire diameter	(205)		(015)		(110)	
[nm]	4°C	20°C	4°C	20°C	4°C	20°C
30	-	-	30	30	-	-
50	-	17	24	27	-	-
260	23	25	33	34	30	33

	60 μm membrane			100 μm membrane		
dep. potential	(205)			(205)		
[mV vs. SCE]	4°C	20°C	35°C	4°C	20°C	
- 40	31	28	26	x	x	
- 100	x	32	x	28	34	

Table 5.1.: Sizes (given in nm) determined for grains with the given preferential orientation. All samples shown for 30- μm thick membranes were deposited at -100 mV vs. SCE. For membranes with thickness of 60 and 100 μm , the etching time was always 7 min. '-' marks that the corresponding grain orientation was not present within the sample, or the signal intensity was too low for evaluation of the grain size. 'x' shows that no sample with the given parameters was measured.

Within the investigated parameter space of deposition conditions, no conclusive tendencies were observable as a function of membrane thickness, nanowire diameter and temperature. The smallest observed grain sizes are ≈ 17 nm, while the largest grains amount to ≈ 34 nm. From the extracted values, it is not possible to conclude that low deposition temperature in combination with the corresponding potentials offer the possibility to tune the average grain sizes in $\text{Bi}_{2+x}\text{Te}_{3-y}$ nanowires in a controlled way. For measurements on samples

grown at more positive deposition potentials of - 40 mV, grains with preferential $\langle 015 \rangle$ texture were found to be as large as 40 nm (wire diameter 50 – 60 nm) and ≈ 51 nm (wire diameter 140 nm), which is larger than under the above mentioned conditions. Values ranging from 49 nm (40 mV, RT) to 62 nm (± 0 mV, RT) were estimated from (110) reflexes in wires with 140 nm wire diameter. In comparison, the deposition potential presumably has a larger impact on grain size in the given electrochemical system than the other growth parameters.

5.3. Transmission Electron Microscopy

For the investigation of the crystalline structure of single nanowires, transmission electron microscopy was conducted on several samples. In all samples that were prepared with a specific electrolyte (5 mMol Bi, 7.5 mMol Te)². Prior to electron microscopy on the wires, the polymer template was dissolved in baths of CH₂Cl₂ or C₃H₇NO. A drop of the final mixture of nanowires and solvent was placed on a holey carbon film supported by a TEM grid. Ni based TEM-grids were chosen rather than the more commonly used Cu grids. This ensured that potential Cu impurities in the wires could be detected and would not be hidden by the EDX-signal from the employed TEM grids. For detailed investigation of the crystalline structures and high-resolution imaging of the compound nanowires, measurements on 6 different samples were made at the MPI for Metals Research in Stuttgart with a JEOL 4000FX with 400 kV. Results from 5 of the samples with diameters below 30 nm are discussed in this section. The deposition potentials for wire synthesis were - 75, - 100 and - 150 mV vs. SCE for growth at room temperature (samples No. B02, B04, B03). For a fixed potential of - 100 mV vs. SCE, the deposition temperature was changed from 4 to 35°C (samples No. B05, B04, B06). Only polycrystalline nanowires were found, independent of the different deposition conditions and wire diameters.

Polycrystallinity has also been observed for conical wires (diameters ranging from 30 – 50 nm) and thicker nanowires with diameters of 70 – 80 nm. In both cases, the deposition potential was -75 mV vs. SCE, the deposition temperature

²preparation by dissolution of TeO₂

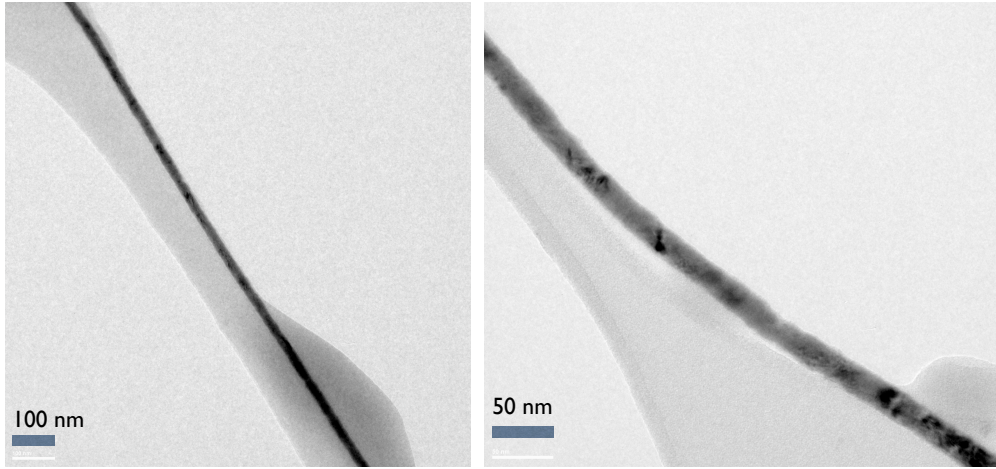


Figure 5.13.: Cylindrical nanowires with average diameter of ≈ 25 nm. (left) Nanowire electrodeposited at -75 mV vs. SCE at RT. (right) Nanowire grown at -100 mV vs. SCE at RT.

4°C . Since the analysis offers no additional information to the shown data, the according TEM images are not presented in this context.

Under the given experimental conditions and local variations in the thickness of the wires, the samples were estimated to exhibit diameters below 30 but larger than 20 nm along the wire axis. From the analyzed samples, the average diameter of the nanowires is approximated by 25 nm. An overview image of cylindrical nanowires deposited at -75 and -100 mV at RT is given in Fig. 5.13. From both images, it can be concluded that the wires exhibit smooth surface contours over long ranges.

High-resolution images were taken in combination with EDX to verify that the wires have the composition of $\text{Bi}_{2+x}\text{Te}_{3-y}$. An overview of the extracted interplanar spacings is given in Tab. 5.2. The given experimental errors are derived from the graphical determination of the distances and the calibration accuracy of the TEM system. For comparison, experimental values obtained by Francombe et al. [25] were included. In all cases, the determined spacings could be matched to known data of Bi_2Te_3 bulk material.

Several HRTEM images are shown in Figs. 5.14 and 5.15, exemplary crystal planes are marked and the extracted spacings given. The grain orientation

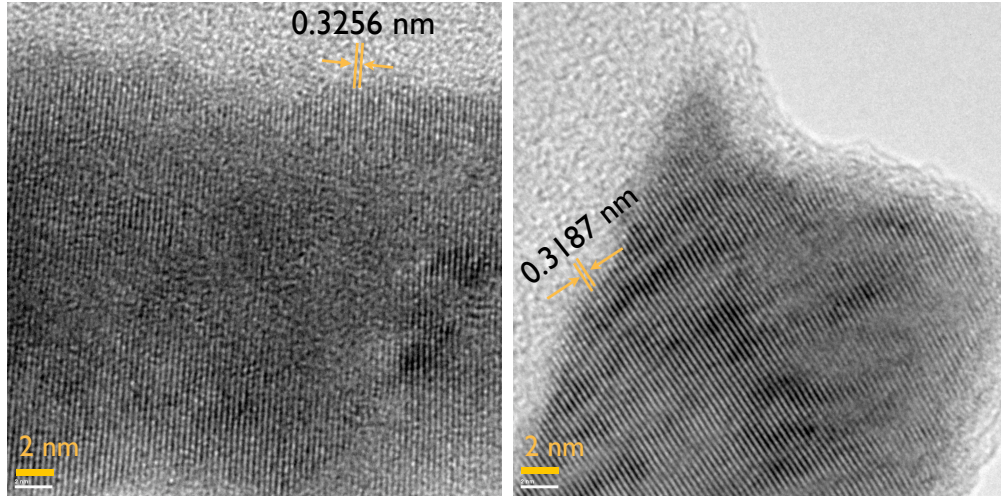


Figure 5.14.: HRTEM view on nanowires with average diameters of ≈ 25 nm, electrodeposited at RT. For the wire deposited at -75 mV (left), the nanowire edge is visible on the top of the image. In the other picture, the nanowire tip is shown for a wire deposited at -100 mV (right). The extracted distances are $d_{(015)} = (3.256 \pm 0.077) \text{ \AA}$ and $d_{(015)} = (3.187 \pm 0.049) \text{ \AA}$.

observed in Fig. 5.14 (left) is in accordance with the texture analysis of wires with 30 nm diameter determined by XRD (Fig. 5.7). The given distance in the image was identified as the (015) plane spacing, which were found to be aligned perpendicular to the wire axis. Fig. 5.14 (right) gives a high-resolution view on a nanowire tip grown at -100 mV. Also in this case, no obvious grain boundaries were detected and the (015) planes can be identified. The grain orientation is tilted by approx. 30° with respect to the wire axis, underlining the polycrystalline nature of the samples, despite the presence of a preferred growth direction. The shown HRTEM images also corroborate the determined average grain sizes by XRD (cf. Tab. 5.1). Further high-resolution views are given to complement the obtained information on crystallite sizes and polycrystallinity. In Fig. 5.15, the wire segments exhibit widths below the average value of 25 nm and, despite the presence of two different crystal planes in the left image, the presence of a grain boundary can not be clearly stated. The angle between the two identified planes (015) and (110) is determined to $\approx 40^\circ$, which is close to the angle between these two planes in undisturbed bulk (42.75° [114]). Hence stress or a slight tilt of the nanowire could be responsible for the change in the

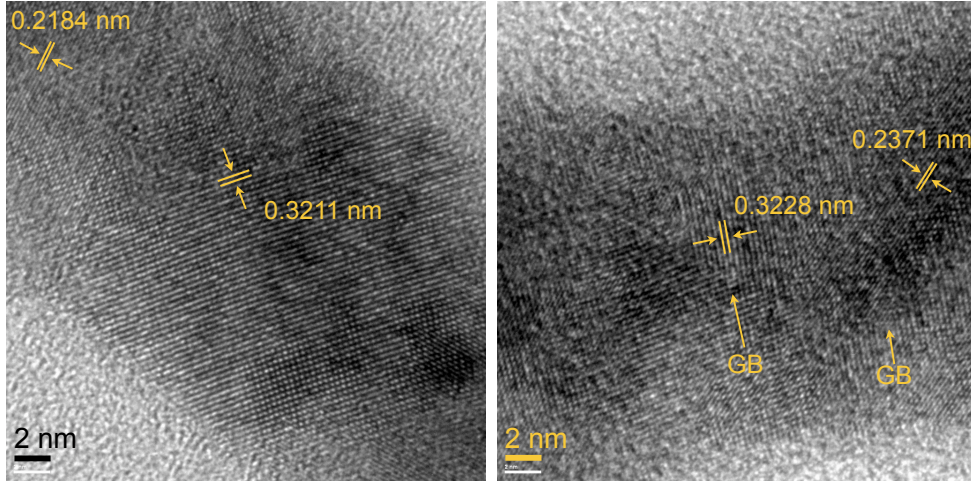


Figure 5.15.: HRTEM view on nanowire segments with diameters below the average of ≈ 25 nm. For the wire deposited at -150 mV (left), the nanowire edge is visible in the top right and bottom left corner of the image. The extracted interplanar spacings are $d_{(110)} = (2.184 \pm 0.060) \text{ \AA}$ and $d_{(015)} = (3.211 \pm 0.077) \text{ \AA}$. In the second image (right), the measured values are $d_{(015)} = (3.228 \pm 0.010) \text{ \AA}$ and $d_{(1010)} = (2.371 \pm 0.078) \text{ \AA}$ presume that the view on the marked grains is along the (015) and the (1010) plane, respectively. The polycrystalline nature of the nanowire is indicated by the presence of grain boundaries (GB). The wire was grown at 4°C at -100 mV vs. SCE.

observed plane in this case. In Fig. 5.15 (right), two different grain orientations are clearly visible, and the existence of grain boundaries (GB) further underlines the polycrystalline nature of the electrodeposited wires.

To sum up, HRTEM investigations have corroborated the findings of XRD, confirming the nanowires being polycrystalline with large grains and Bi_2Te_3 -based in origin. Furthermore, all measured wires were cylindrical in shape, showing smooth surface contour as expected from the shape of the nanochannels. In addition, the variation of deposition parameters between deposition potentials of -75 to -150 mV are not sufficient to yield visible variations, neither in the determined distances nor in the size of crystallites. This is also in accordance with XRD on nanowires with slightly larger diameters where, independently from the applied potential, only arrays with a preferential orientation of the (015) plane perpendicular to the wire axis were observed.

Sample No.	interplanar spacings [\AA]		plane
	HRTEM	Ref. [25]	
B-02	3.206 ± 0.052	3.22	(015)
	3.263 ± 0.084	3.22	(015)
	3.247 ± 0.084	3.22	(015)
	3.279 ± 0.095	3.22	(015)
	3.256 ± 0.077	3.22	(015)
B-03	3.211 ± 0.077	3.22	(015)
	2.386 ± 0.092	2.378	(1 0 10)
	2.184 ± 0.060	2.191	(110)
	1.807 ± 0.065	1.810	(205)
B-04	5.048 ± 0.125	5.09	(006)
	3.197 ± 0.057	3.22	(015)
	3.185 ± 0.058	3.22	(015)
	3.187 ± 0.049	3.22	(015)
B-05	3.228 ± 0.099	3.22	(015)
	2.371 ± 0.078	2.378	(1 0 10)
	2.371 ± 0.072	2.378	(1 0 10)
B-06	1.843 ± 0.076	1.810	(205)

Table 5.2.: Overview on the extracted interplanar spacings for the different samples measured by HRTEM. All extracted values are in accordance with experimental values from Francombe et al. [25].

Conclusions

The investigation of the morphology of electrodeposited $\text{Bi}_{2+x}\text{Te}_{3-y}$ nanowires and caps has evidenced a deposition potential-dependent variation of the nanowire roughness at approx. -75 mV vs SCE, with the observation of rougher nanowire contours and stronger cap texture for more negative deposition potentials. Even though the transition point could not be correlated to observed changes in XRD or HRTEM, diffraction analysis has shown temperature, potential, and diameter dependent variations in preferential growth of the nanowire arrays.

In general, the appearance of the x-ray diffraction peak from the (205) plane spacing was dominant in many samples, preferably when arrays were deposited in thick membranes. It is found to be possible to reduce this diffraction peak successfully in $30\text{-}\mu\text{m}$ thick membranes by lowering the temperature of the growth process to 4°C , or switching to more positive deposition potentials. Via this approach, the other present orientation (mostly $\langle 015 \rangle$ or $\langle 110 \rangle$) is increased comparatively in signal.

Nanowires deposited at increasingly negative potentials with respect to the reference electrode potential have shown to prefer $\langle 015 \rangle$, in addition to $\langle 205 \rangle$ texture. For wires with larger diameters of $\approx 140\text{ nm}$, a transition from the preferential growth of the $\langle 015 \rangle$ to the $\langle 110 \rangle$ orientation was observed. This demonstrates that it is possible to tune the preferential orientation of nanowire growth for the investigated electrolyte-membrane system by variation of the potential.

Thinner nanowires and the corresponding caps have not exhibited visible morphological changes, indicating a size dependent influence in the deposition process. This observation is further corroborated by the XRD measurements on samples grown at $\pm 0\text{ mV}$ at 4°C . While wires with diameters of $\approx 140\text{ nm}$ show preferential textures of $\langle 110 \rangle$ and $\langle 205 \rangle$, wires with diameters in the range of $50 - 60\text{ nm}$ have shown a dominant reflex from the (015) plane. Over a wide range of deposition parameter, nanowires with low diameters predominantly exhibit $\langle 015 \rangle$ texture and mostly low intensities of the (205) reflex. In combination with the potential dependent variation of the texture, this evidences that

nanochannel diameter is a relevant factor for the selection of growth conditions.

Preferential $\langle 110 \rangle$ texture is found in Te-rich composites in literature [59, 98], while $\langle 015 \rangle$ texture is present in Bi-rich nanowire arrays [50] and films [100]. If a correlation between structure and composition proves true, the shown data suggests that the transition between Te-rich and Te-deficient composites can be tuned by the nanochannel diameters, as well as the applied deposition potentials.

Despite high texture coefficients, XRD and HRTEM have both shown that the wires are polycrystalline Bi_2Te_3 with grain sizes of the order of tens of nm.

6. Composition Analysis

The undoped Bi_2Te_3 semiconductor is known to exhibit p-type electrical conductivity. Doping by Te, I or Se has been shown to increase the charge carrier density of the n-type $\text{Bi}_{2-x}\text{Te}_{3+y}$, whereas doping with Bi, Si, Sb is known to transform the system into a p-type semiconductor. Already small amounts of copper ($\approx 1 \text{ at}\%$) are known to tune the charge carrier type from p- to n-type [115]. Due to the large variety of potential dopants in combination with usually very acidic electrolytes, the substrates used for electrochemical deposition have to be chosen carefully to inhibit contamination of the compound as well as possible. In addition to deliberately or unwittingly doping with other elements, $\text{Bi}_{2-x}\text{Te}_{3+y}$ can also change its type of conductivity by tuning the deviation of Bi and Te with respect to the stoichiometric compound. Since suitability of a thermoelectric material strongly depends on the sign of the Seebeck coefficient, as well as the electrical conductivity, it is necessary to obtain as much information as possible on the elemental composition of the nanowires and the correlation with their crystalline structure. For the determination of change in composition of the grown samples for varying deposition conditions, and in order to assess whether impurities can be found in the grown samples, EDX measurements were performed. TEM/EDX was used for the investigation on single wires, while SEM/EDX measurements were conducted on nanowire bundles and caps.

6.1. Energy Dispersive X-Ray (EDX) Analysis

Energy dispersive x-ray analysis (EDX) in SEM and TEM was employed to determine the composition of the nanowires. In Fig. 6.1, the interaction of an impinging electron beam with bulk samples is schematically depicted for the

case of SEM. In the case of low-density materials, the volume excited by the electron beam is larger than in the case of high-density materials. The range of the primary electrons R_{PE} is dependent on the acceleration voltage E_0 and the mass density of the material ρ . It can be described with the empirical relation [116]:

$$R_{PE} = 100 \cdot E_0^{1.43} \cdot \rho^{-1} \quad . \quad (6.1)$$

With an acceleration voltage of 8 kV, $R_{PE} \approx 840$, 250, and 100 nm for Si, Bi_2Te_3 , and Au, respectively. At an increased energy of 20 keV, R_{PE} amounts to 3.1 μm , 950 nm, and 375 nm for the same set of materials. In analogy to the interaction of accelerated charged ions with matter, electrons also undergo elastic and inelastic scattering. Elastic processes are single- and multiple-scattering

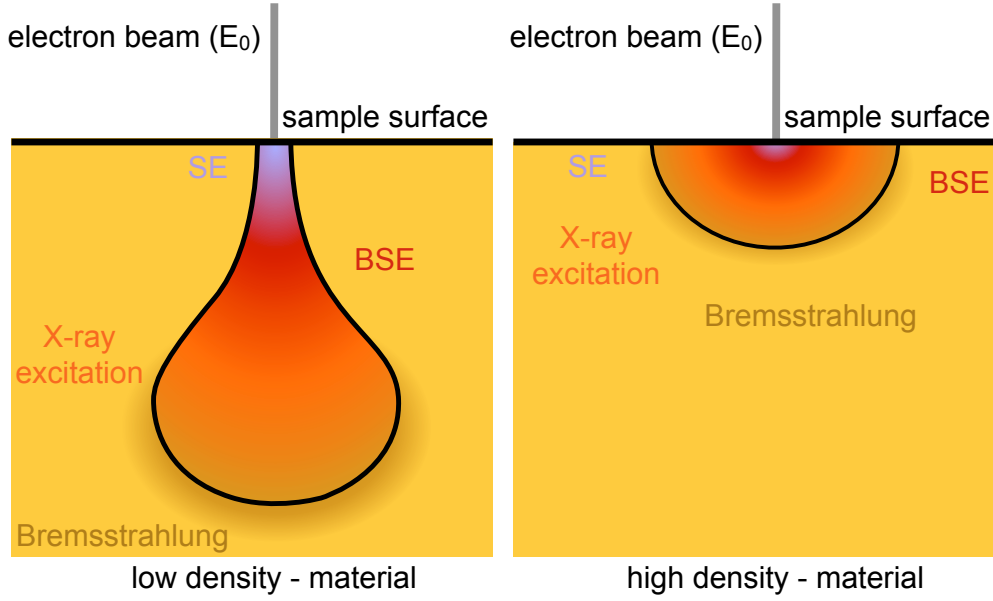


Figure 6.1.: Schematic illustration of the electron-sample interaction in SEM for low- and high-density materials. For both cases, escape depth of secondary and backscattered electrons, as well as characteristic x-rays and bremsstrahlung are depicted. The range of primary electrons and the width of the excited volume increase for larger acceleration voltages and scale inversely with sample density.

at target nuclei, which is accompanied with changes in electron trajectory and only minor changes in the electron energies. These so-called backscattered electrons (BSE) have high energies with a possible maximum value close to E_0 . The

yield of backscattered electrons increases with target density and can therefore be used to observe large compositional variations through intensity variations in detector signals. Inelastic scattering processes arise due to the interaction of the incoming electrons with the shell electrons of target atoms or target nuclei. The most prominent interaction is the creation of secondary electrons (SE) with low energies, ≤ 50 eV, which originate from energy transfer of high-energy electrons to shell electrons. SE electrons which are created in the surface near region of the specimen are mostly used for SEM imaging and suggest that the interaction of the electron beam with a material is only superficial, even though the real interaction volume is much larger (cf. Fig. 6.1). At larger depth, the electron energies are still sufficient to lead to the ionization of the target atoms. The photon that is emitted when the atom reverts to its original state, is element specific and can therefore be used to identify different elements within a sample as shown in Fig. 6.2, and to determine the composition of a specimen. In

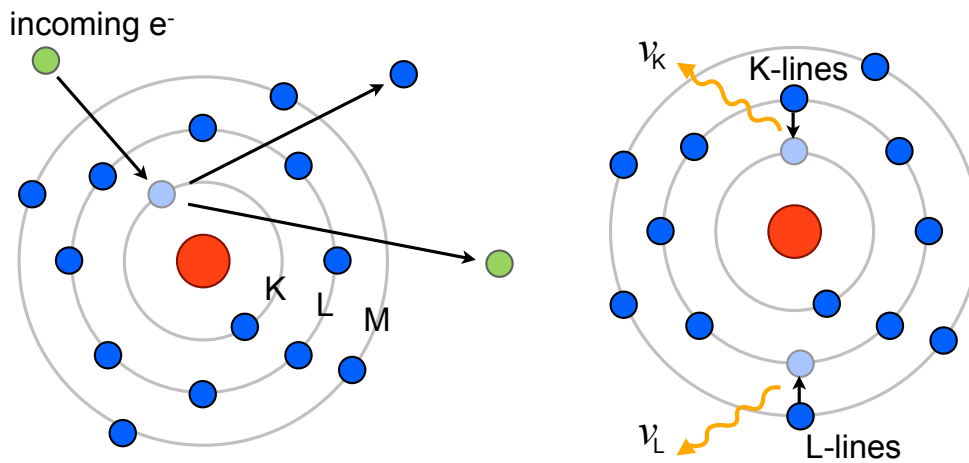


Figure 6.2.: The energy transfer from an incoming electron leads to the formation of a hole in a lower shell of the electron system of an atom. When the hole is filled by transition of an electron from the L- to the K-shell, then the emitted photon ν_K belongs to the so-called K-series. In analogy, transition from M- to L-shell yields a L-line photon ν_L . According to Moseley's law the photon energy is element and transition specific [117].

addition to the schematic description in Fig. 6.2, holes in a specific shell, e.g. K-shell, can also be filled by electrons from different shells, e.g. the M-, not only the L-shell in the given case. Further diversification of possible photon

energies is observed, when electron spin is considered and subshells need to be taken into consideration. Therefore, electron transitions to a specific shell are represented by a characteristic line spectrum in EDX analysis. Since the cross section for excitation of the electron system is energy dependent, E_0 must exceed the excitation energy by at least 2 – 2.5 times. For excitation of the Te L-lines, this corresponds to a minimum acceleration voltage of 7.54 kV. The Bi M-Line is lower in energy, therefore the minimum threshold for excitation is found at lower energies, and the Te-lines needs to be considered for choosing the right electron energies for EDX measurements. By increasing the acceleration voltage, the penetration depths of the electrons and hence the interaction volume is also increased. This implies several limitations to the composition analysis via electron beam excitation, e.g. the lateral resolution due to beam straggling and information depth R_d . The latter quantity is determined by primary electron energy, excitation energy needed for the electron transition between the shells and the material's atomic mass A , atomic number Z_A and mass density ρ . The maximum depth of X-ray generation can be approximated according to Castaing's formula [116]

$$R_d = 0.033 \cdot \left(E_0^{5/3} - E_c^{5/3} \right) \frac{A}{Z_A \cdot \rho} \quad , \quad (6.2)$$

where the acceleration voltage of the electrons E_0 should be inserted in kV and the energy of the generated x-rays E_c in keV. This yields R_d in μm . For 8 keV electrons in Bi_2Te_3 , R_d is 200 – 300 nm for Te and Bi, for 20 keV it was estimated to 1.5 – 1.6 μm . From the known diameters of the nanowires (max. 250 nm) and the calculated values for R_d and R_{PE} , it can be seen that even though high acceleration voltages are necessary to induce excitations in the electron shell of the target nuclei, it will also lead to an increased contribution from the substrate to the detected EDX signals and automatically reduces the signal strength of the Bi M-lines and the Te L-lines in comparison to the employed substrates, thereby decreasing the accuracy of the measurements. Therefore, an acceleration voltage of 8 kV was chosen for the measurements in SEM/EDX, since the use of a substrate could not be omitted under the given experimental conditions. With respect to the different interactions of electrons with matter, it should be included that the inelastic scattering of the electrons at target nuclei leads to appearance of bremsstrahlung, which is visible as background signal in EDX

analysis and also increases with higher acceleration voltages. Despite its lack of high accuracy, as compared to electron probe microanalysis (EPMA) with wave dispersive x-ray analysis (WDX), EDX can be employed with lower beam currents, hence reducing sample contamination and compositional or structural changes in radiation sensitive materials. For measurements on very thin samples, as prepared for TEM, adapted sample holders can also be used in SEM, avoiding interfering contributions from the substrate and significantly increasing the lateral resolution as compared to EPMA or conventional SEM/EDX.

6.2. SEM/EDX on Nanowires

Varying deposition conditions have shown to influence morphology and texture of nanowires. SEM/EDX analysis was performed on a JEOL JSM-7401F with an EDX system from Bruker AXS, to determine the influence of the deposition conditions on the composition of nanowire arrays. Due to the low interaction volume of the nanowires and the interfering contribution of substrates to the overall EDX spectra, successful composition analysis with SEM was only possible on bundles. Measurement times were chosen dependent on the obtained count rates and ranged from 6 to 9 minutes for the measurement of bundles as well as caps. Ignoring straggling of the electron beam, a diameter reduction of a factor of 2 yields a reduction of the potentially excited nanowire volume and count rates by 75 %.

Examples for EDX spectra, obtained from nanowire bundles of one sample and the corresponding SEM images, are displayed in Fig. 6.3. The shown wires have an average diameter of 200 nm and were deposited at room temperature at an applied potential of -100 mV vs. SCE. The analysis was performed with an acceleration voltage of 8 kV. Considering the experimental uncertainties of approx. 2 at%, The lower wire bundle exhibits a Te-rich composition (36 at% Bi, 64 at% Te). This tendency is also suggested for the set of wires (38.5 at% Bi, 61.5 at% Te) in the upper image, albeit the determined composition is close to stoichiometry in this case. In addition to the presence of C and O, only Si and Au from the substrate were identified in the spectra. No traces of other elements were visible, besides a minor contribution from Al, which is always present for

beam currents in the order of 500 pA or higher and long measurement times, and arises from stray radiation in the specimen chamber. For comparison, the composition of multiple nanowire bundles was determined for several samples. The extracted concentrations are given in Tab. 6.1 with the corresponding deposition conditions.

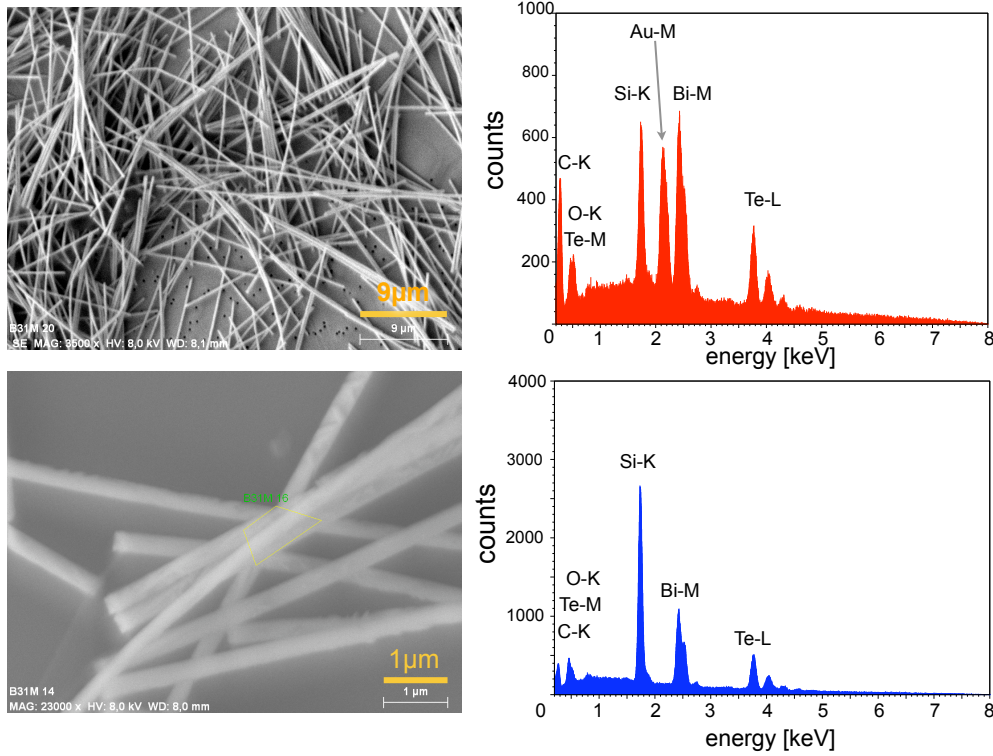


Figure 6.3.: SEM images on bundles of $\text{Bi}_{2+x}\text{Te}_{3-y}$ nanowires grown at -100 mV. The diameters are ≥ 100 nm. The corresponding EDX spectra are shown on the right side of the SEM images. In both cases, x-ray analysis indicates that the wires are Te-rich with extracted concentrations of ≈ 38.5 at% Bi and 61.5 at% Te for the upper sample and ≈ 36 at% Bi and 64 at% Te in the lower sample. The Si and Au peaks arise from the substrate and the cathode, respectively.

A comparison of the results indicates that lowering the deposition potential from 0 to -100 mV increases the Bi content of compound nanowires with diameters in the range of 150 to 200 nm. This would be in accordance with published results on electrodeposited thin films. However, the accuracy of the determined element concentrations suggests that the potential difference needs to be further increased to verify this tendency with the given experimental setup.

wire diam. [nm]	potential [mV]	membrane thicken. [μ m]	T _{dep}	Bi at%	Te at%	Δ at%
140 - 170	- 100	100	RT	38.5	61.5	2
200	- 100	30	RT	38	62	2
150	± 0	30	4 ° C	35.7	64.3	1.8
150	± 0	30	RT	36.7	63.3	1.9

Table 6.1.: SEM/EDX analysis of the averaged composition of bundles of nanowires with similar diameters. The growth conditions of the different samples are included in the table.

Nonetheless, deposition at -100 mV vs SCE in large nanochannels yields wires with composition close to stoichiometry, while a potential of 0 mV suggest the formation of Te-rich composite.

6.3. TEM/EDX on Nanowires

In combination with the HRTEM analysis of $\text{Bi}_{2-x}\text{Te}_{3+y}$ nanowires (see sect. 5.3), different wires were additionally characterized by EDX. The results of the composition analysis are shown in Fig. 6.4. All wires were grown in identically etched membranes, the average diameters were ≈ 25 nm. For comparison, deposition potentials and temperature were changed from -75 mV to -150 mV and 4 ° C to 35 ° C, respectively. The measured Bi:Te ratios are given with the according deposition parameters. From the histogram it can be concluded, that within the given experimental uncertainty no conclusive difference in the composition was found for this set of nanowires, despite the variety of growth conditions. This is in conformity with the observation made in SEM/EDX measurements. While bundles of nanowires with large diameters exhibit a Te-rich composition, the wires investigated HRTEM/EDX are Bi-rich, with a composition between BiTe and Bi_2Te_3 . In one of the samples, even higher Bi concentration was determined.

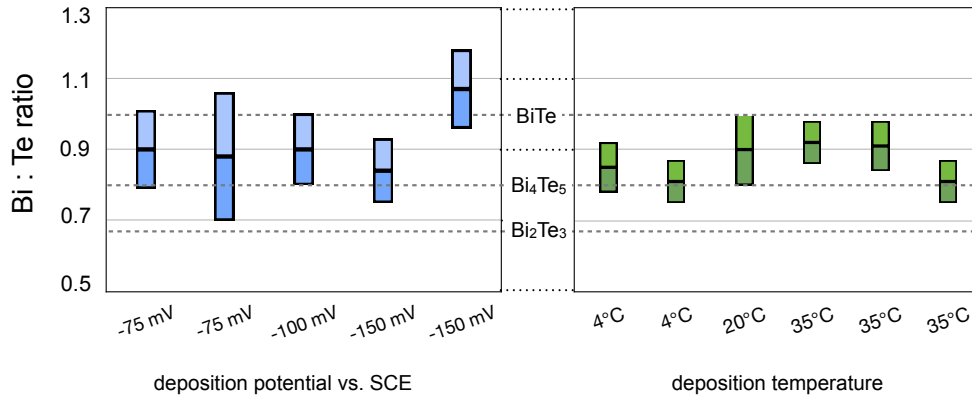


Figure 6.4.: Experimentally determined Bi:Te ratios for (a) different deposition potentials for constant deposition temperature of 20 °C and (b) for varying deposition temperature at constant potential -100 mV vs. SCE. Nanowire diameters are approx. 25 nm, theoretical Bi:Te ratios for Bi_2Te_3 , BiTe and Bi_4Te_5 are given for comparison.

6.4. EDX Analysis of Nanowire Caps

Motivated by the correlation between the morphology of nanowire caps and the crystallinity of single-element metal nanowires [77,108,109], energy dispersive x-ray analysis has been conducted on the caps of several samples and exemplarily compared with the concentration determined on the nanowires of sec. 6.3. The measurements were performed at a Philips XL30 SEM with a thermal tungsten emitter at voltages of 20 kV. Prior to the measurements, the samples with low number density of caps were coated with a few nm thick Au layer to avoid charge influence on the EDX spectra. For quantitative analysis of the spectra, Bi M-lines and Te L-lines were considered. In contrast to prior experiments, where the nanowire deposition was performed on copper plated and not only sputter coated cathodes, no visible traces of impurities were found in the spectra of the caps. The EDX spectra on caps from different samples¹ are shown in Fig. 6.5(a) and (b).

On the left side, SEM images of the caps are given, while exemplary EDX results for the different cap morphologies are displayed on the right side. All investigated caps grew on top of wires with diameters exceeding 100 nm and

¹for the different cap morphologies, cf. Fig. 5.2

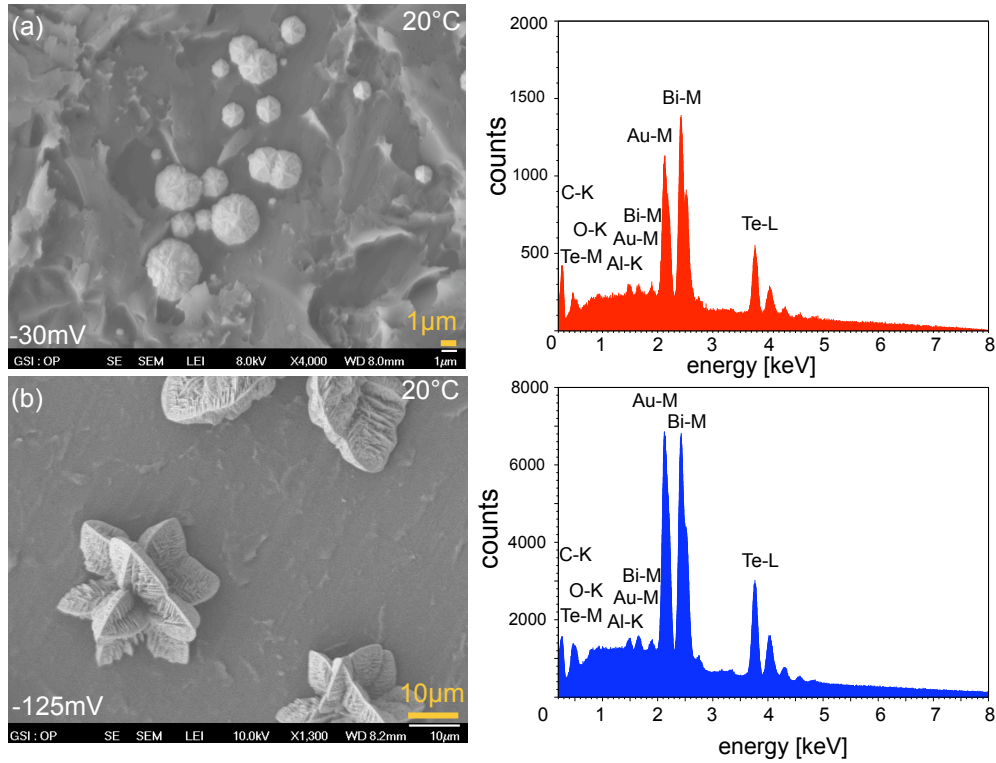


Figure 6.5.: EDX spectra of caps grown on nanowires with the given deposition conditions. The samples were coated with a thin Au layer to avoid charge buildup on the sample surface. Pore opening diameters were exceeding 100 nm. Neither signals from potential impurities nor large compositional changes are indicated in the shown spectra. Within experimental errors, both cap morphologies exhibit compositions close to the stoichiometric compound.

with the corresponding deposition conditions. For growth at -30 mV, the concentrations are determined to 39.4 at% Bi and 60.6 at% Te with an experimental uncertainty of 1.9 at%. The more textured caps, electrodeposited at -125 mV, exhibit average of 38.8 at% Bi and 61.2 at% Te (± 2 at%). With the same experimental error, measurements on large round caps, which appear to develop out of shown textured caps, showed a composition of 40.9 at% Bi and 59.1 at% Te. Analogously to the SEM/EDX observations on nanowires, no impurities were visible in the measured spectra. Neither for deposition temperature variations from 4°C to 35°C for a fixed potential of -100 mV vs. SCE, nor for potential variation from -30 to -150 mV vs. SCE at a deposition temperature of 20°C , any definite compositional variations could be extracted from the measured data. Due to the nanochannel diameter-related variation of cap morphology and observed texture, a comparison of the obtained Bi-Te ratio for caps grown on small-diameter pore openings (30 nm) and the HRTEM results on nanowires is shown in Fig. 6.6.

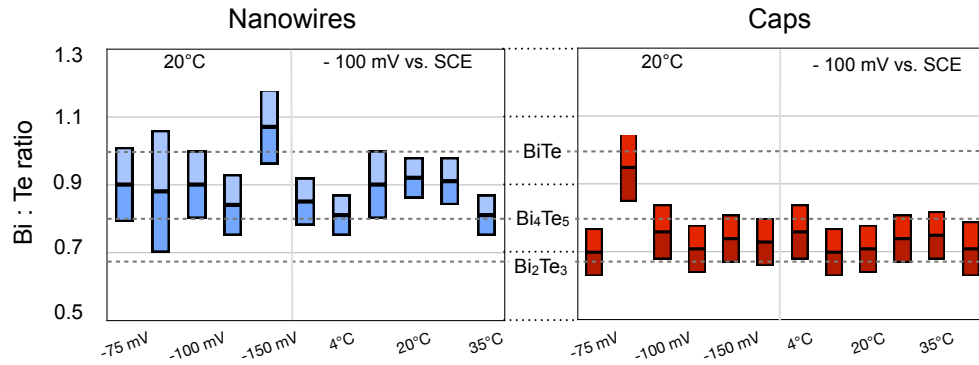


Figure 6.6.: Experimentally determined Bi:Te ratios for (a) 25 nm diameter nanowires by EDX in TEM and (b) the corresponding caps observed on top of the templates. The theoretical Bi:Te ratios for Bi_2Te_3 , BiTe and Bi_4Te_5 are given for comparison.

In the given plot, it can be clearly seen that nanowires appear Bi-richer than caps, independent of the deposition conditions. The composition of the caps has been corroborated for several samples by additional EDX measurements with a different SEM/EDX system². In that case, the average composition ratio was shown to vary between 0.67 ± 0.07 to 0.77 ± 0.07 , which is also on the Bi-rich

²JEOL JSM-7401F with Bruker EDX detector

side of the $\text{Bi}_{2-x}\text{Te}_{3+y}$ composite. In general, EDX data obtained for both cases suggest that caps as well as nanowires with a diameters of 25 nm are on the Te-deficient side of the stoichiometric compound.

Conclusions

As for the texture variation in the case of electrodeposition of increasingly thinner nanowires, the composition measured by EDX also indicates an influence of the restricted geometry of the nanochannels.

While measurements on nanowire bundles exhibit Te-rich composition for various deposition conditions and large wire diameters, TEM/EDX suggests a Bi-rich compound for nanowires with small diameters. These observations fit the evaluation of the preferential growth of the nanowires, where the (110) and (101) reflexes occurred for larger wire diameters, while the $\langle 015 \rangle$ texture was dominant in the case of thin wires.

First EDX results suggest that the correlation between texture and composition holds for the electrochemical growth of nanowires and only small deviations from stoichiometry can be assumed, which is in accordance with observations on submicron wires. The results indicate that the transition conditions for the change from n- to p-type could be a function of the nanochannel diameter, which should be considered for future experiments. If this indication proves true, it would be of great importance to the thermoelectrics community and would shed new light on the preparation of thermoelectric nanowires.

In order to obtain more detailed information on the composition, a reduction of the substrate contribution to the nanowire EDX spectra is essential. With the given accuracy of the setup, only indications on the influence of the deposition parameters can be given. Comparative measurements on different SEM/EDX and TEM/EDX systems are necessary to determine the composition of the wires more precisely and to determine potential deviations arising from the different set-ups and quantitative algorithms, employed for the analysis.

The viable information obtained from the measurements on caps is the conclusion that morphology and composition could not be correlated for the in-

vestigated samples. Furthermore, EDX on caps on embedded wires with small diameters showed that the composition of nanowires is not in accordance with the composition of the corresponding caps. This deviation might arise either from the different devices for analysis or, alternatively, from the different electrochemical deposition conditions for recessed nanoelectrodes and hemispherical microelectrodes.

7. Summary and Outlook

The presented work covers the electrochemical growth of Bi_2Te_3 nanowires in ion track-etched templates and the characterization of their morphology, composition and crystallographic characteristics. Therefore, the relevant deposition parameters, e.g. electrolyte concentration, deposition potential and temperature, have been systematically varied to demonstrate their influence on the growth process. For a specific electrolyte, the aforementioned properties were investigated on nanowires with different diameters and lengths as a function of deposition potential and temperature.

Polycrystalline Bi_2Te_3 nanowires were electrochemically deposited in ion track-etched membranes of various thicknesses ranging from 30 to 100 μm . Fabrication of membranes by heavy ion irradiation of polycarbonate foils at the linear accelerator at GSI and subsequent chemical etching enabled the synthesis of nanowires with diameters as small as 20 nm and nanowires with length of 100 μm .

Systematic studies on the parameters for electrochemical deposition have been conducted with respect to the control of growth rates. Slower growth rates were achieved by lowered ion concentrations in the electrolyte and lowered deposition temperatures. Electrochemical growth at 4°C has shown to increase the effective filling ratio of the nanochannels during the fabrication process. In addition, indications were found that this could be accompanied by increased homogeneity of the deposition. Deposition of Bi_2Te_3 nanowires in 60- and 100- μm membranes exhibited a significant reduction of the growth rates as compared to growth in 30- μm membranes.

Nanowire and cap morphology were analyzed by electron microscopy. Morphological changes were observed as a function of the deposition conditions and

nanochannel diameter. For growth under small negative or positive potentials with respect to the reference potential and low deposition temperature, smooth contours of the nanowires were observed. Increasingly negative potentials, in combination with room temperature growth, led to increasingly rougher wire surfaces and highly textured caps.

The preferential orientation of the bismuth telluride nanowires was investigated by XRD. The investigation of the structural properties of nanowires deposited in thick membranes exhibited that the most dominant reflex in the $\omega - 2\Theta$ scans corresponds to the orientation with the (205) plane perpendicular to the wire axis and direction of wire growth.

Further studies showed that it was possible to control the preferred growth orientation for deposition in 30- μm membranes via applied potential and temperature. In particular, lower deposition temperatures led to a reduction of the (205) peak, while an increase in peak intensity of additionally present orientations is detected.

A very important result is the influence of nanochannel diameters on the preferential growth direction of the nanowire arrays. For fixed deposition conditions at 0 mV vs. SCE and 4°C, a reduction in the channel diameter from $\approx 140\text{-}150\text{ nm}$ to 50-60 nm has brought about the disappearance of the (110) reflex and the occurrence of preferential growth with the (015) planes perpendicular to the wire axis. At -100 mV vs. SCE, size reduction is tentatively accompanied with reduction of the (205) reflex. In addition, it was possible to demonstrate the tuning of the $\langle 110 \rangle$ to the $\langle 015 \rangle$ growth in nanowires with intermediate diameters, by varying the deposition potential.

Due to the highly anisotropic structure of bismuth telluride, deposition-control over crystallographic characteristics is of great relevance to the characterization of the thermoelectric properties of nanowires. Since the aforementioned potential dependent change in growth direction was not observed for thinner nanowires grown under the same conditions, this result further evidences the importance of systematically investigating the influence of the deposition parameters directly on nanowires rather than on thin films deposited with the same conditions. In addition, it shows that it is possible to tune the texture of

nanowires grown in ion track-etched membranes by variation of the deposition potential. Evaluation of the grain sizes by XRD shows no dependence on the employed growth conditions. Their sizes predominantly range from approx. 20 to 35 nm, which was found to be in accordance with observations on thin wires by HRTEM.

Energy dispersive X-ray analysis indicates Te-rich composition for wires with larger diameters and Bi-rich composition in thin wires. SEM/EDX on nanowire bundles also suggests, within experimental errors, that the Bi-content of wires with diameters of ≈ 150 nm is increased for increasingly negative deposition potentials.

In this work, the advantages of the versatile combination of electrochemical nanowire growth and ion track-etched membranes are successfully demonstrated by the synthesis of $\text{Bi}_{2+x}\text{Te}_{3-y}$ nanowires with very small diameters and large lengths. Furthermore, the influence of the deposition parameters on the fabrication process has been demonstrated. Variation of deposition conditions, e.g. electrolyte concentration, deposition temperature and potentials, and modification of nanowire diameters and lengths offer opportunities for the controlled growth and design of compound semiconductor nanowires. Precise knowledge of the interplay between these parameters is of great importance for the final thermoelectric performance of a semiconducting composite and indispensable for the interpretation of measured physical properties with respect to finite size or quantization effects, being it for application as low-dimensional model system for basic research or as a functional device.

Aiming at understanding and improving the thermoelectric properties of low-dimensional structures, future work will focus on measuring electrical and thermal properties of single nanowires with different compositions and crystallographic characteristics. For the development of a prototype nanowire-based thermoelectric device, efforts will focus on the fabrication of nanowire arrays with an increased filled volume fraction. This will be advantageous for the determination of the Seebeck coefficient in embedded nanowire arrays and for measurements of the thermal conductivity of the nanowire-polymer composite structures.

More generally, detailed structural and compositional analysis is of great importance for the determination of specific physical properties and additional work is needed to further explore the implications of size restriction by low-diameter nanochannels on the synthesis and physical properties of single-element and compound nanowires.

A. Ion Track-Etched Membranes

Ion track-etched membranes cover a large variety of technological applications, reaching from filter systems to membranes for nanostructure synthesis [77, 118–121]. Fabrication of these templates by the irradiation with heavy ions at the UNILAC facility of GSI offers several advantages over the commercially available membranes. Due to the high energy of the projectiles, comparatively thick polymer films can be irradiated and subsequently etched to polymeric membranes, with aspect ratio of the channels as high as 1000:1 [86]. In comparison to other facilities, the irradiation setup offers an ion beam with negligible angular dispersion, leading to highly oriented, i.e. parallel, damage tracks in the polymers. In all cases of fabrication of ion track membranes, the lateral positioning of the channels on a samples surface is random. For a given channel diameter d and ion fluence Φ , the probability of overlapping of two pore openings P_2 can be described by Poisson's Law [122],

$$P_2 = 1 - e^{-\pi d^2 \Phi}. \quad (\text{A.1})$$

Since the increase of the ion fluence automatically increases the area density of tracks and, hence, also the channel density in membrane, the probability of overlapping channels should be known for the specific application of the membranes. With respect to the usage as template for the synthesis of nanowires with specific size dependent properties, this is of special importance to ensure homogenous wire diameters for the majority of the grown nanowires. In Fig.A.1 an overview is given on the correlation between the maximum nanochannel diameter and the ion fluence for specific fixed amounts of pore overlaps. This correlation should be kept in mind for aiming at nanowire-polymer compos-

ite based thermoelectric devices, when nanowires with very low diameters are necessary to take advantage of nanoscale effects.

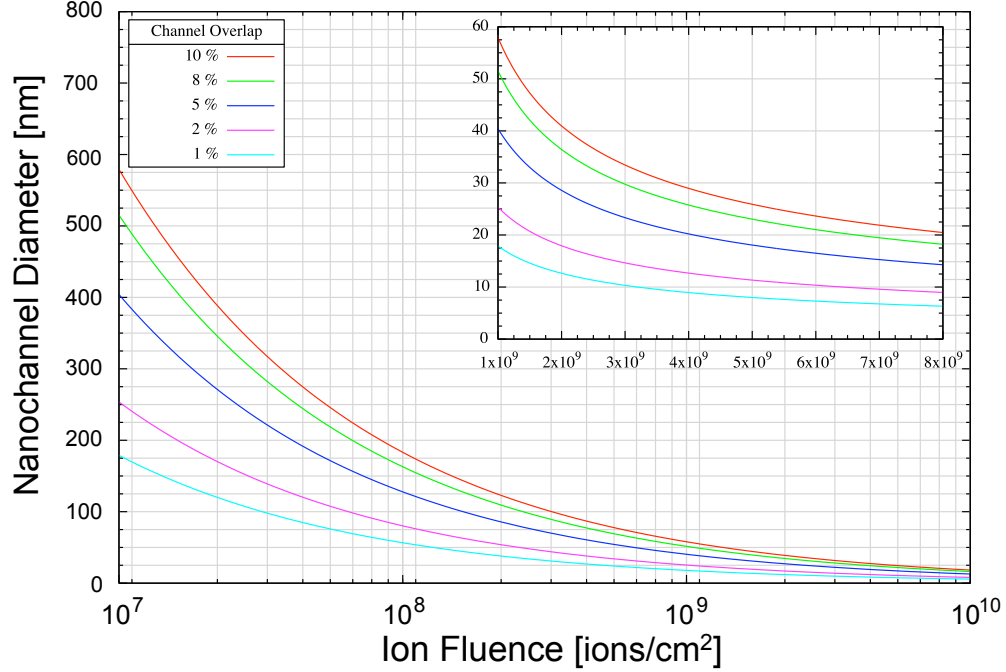


Figure A.1.: Channel diameter to ion fluence correlation for different probabilities of overlapping channels in ion track-etched membranes.

Several realizations for nanowire based thermoelectric devices have already been published [123,124]. The quantitative analysis of their performance did, so far, not meet the high hopes of low-dimensionality. Several implications need to be considered for potential application of nanowire based devices. In the following section a few basic considerations for on nanowire-template-composites and thermoelectric application are presented. Not only the difficulty in obtaining high quality nanostructures is one limiting factor in this context, in the last few years, the negative influence of the membranes or supporting structures has been repeatedly put into focus. The templates in which the nanowires are grown work as thermal shunts, i.e. they contribute to the overall thermal conductivity of the thermoelectric legs and significantly impede any beneficial contribution from the size reduction of the thermoelectric materials. In a simple model, the thermal conductivity can be assumed as the weighted sum of the surface fraction

occupied by the nanowires f_{nw} and the membrane f_M , respectively,

$$\kappa = f_{nw} \kappa_{nw} + (1 - f_{nw}) \kappa_m. \quad (\text{A.2})$$

The usage of a template with low thermal conductivity would be preferable to keep the negative influence of the membranes on the thermal conductivity as low as possible. In this context, Biswas et al. [63] reported the growth of bismuth telluride nanowires in AAO templates and used the effective medium approach to determine the reduction in ZT for composites. After replacing the AAO membrane with SU-8 via spin coating, while keeping the nanowire number density constant, measurement by a photoacoustic method exhibited a reduction of the thermal conductivity of 21% for the composite structures. Thereby they demonstrated the beneficial impact of polymeric template on the thermoelectric figure of merit. These considerations can be extended to include the influence of the nanowire fraction on ZT . The most commonly used membranes, e.g. non-conductive polymers, alumina, are insulators, therefore their contribution to the electrical conductivity can be neglected, while the fraction of thermoelectric material f_{nw} should still be reflected in the conductivity. ZT is then described by

$$ZT_{\text{comp}} = S^2 \frac{\sigma f_{nw}}{f_{nw} \kappa_{nw} + (1 - f_{nw}) \kappa_m} T = F(\kappa_m, \kappa_{nw}, f_{nw}) \cdot S^2 \cdot \sigma \cdot T. \quad (\text{A.3})$$

A comparison of qualitative dependence of $F(\kappa_m, \kappa_{nw}, f_{nw})$ on the fraction of nanowires is given in Fig.A.2 for different host materials : air ($\kappa = 0.03 \text{ W/mK}$), polycarbonate ($\kappa = 0.2 \text{ W/mK}$) and alumina ($\kappa = 1.5 \text{ W/mK}$).

As seen from the work of Biswas et al. [63] and the results in Fig.A.2, the dependence of ZT on the thermal conductivity of the template material and the fraction of thermoelectric material is crucial. Especially low thermal conductivity alone is not sufficient for enhanced ZT , which is a large drawback of common ion track-etched membranes. The embedded nanowire arrays would need to represent approx. 20 to 30% of the nanowire-template composite to offer the same ZT as a corresponding AAO membrane with a nanowire volume fraction of 70 to 80%. It can be seen that deliberating nanowires from the templates is the most advantageous solution for obtaining a high ZT devices based on nanowires, independently from the gain in reduced thermal conductivity by

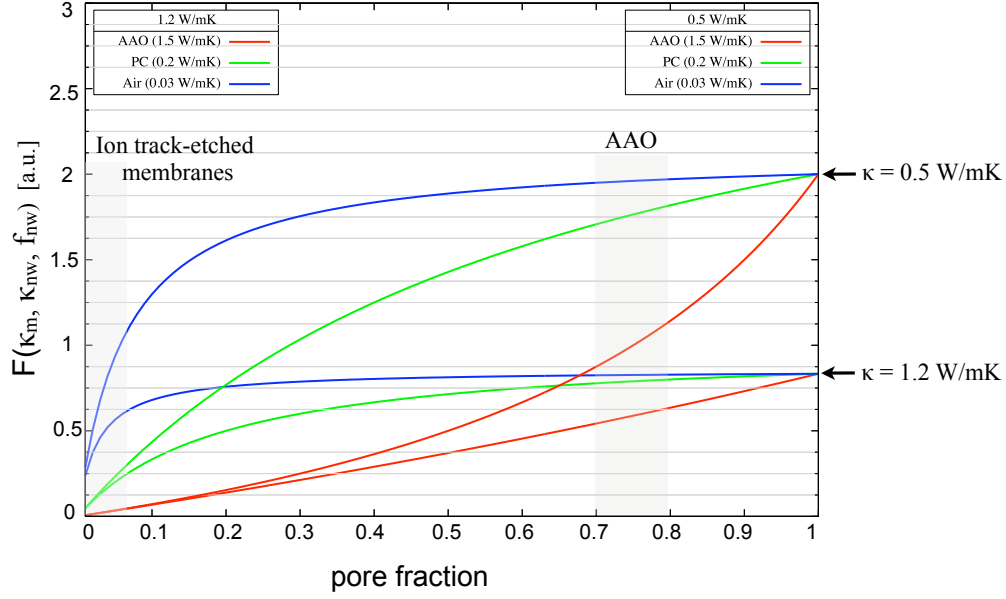


Figure A.2.: $F(\kappa_m, \kappa_{nw}, f_{nw})$ (in arbitrary units) as a function of the nanowire fraction in different host materials with the given thermal conductivity. The thermal conductivity of the nanowires is assumed 1.2 W/mK and 0.5 W/mK. The pore fraction in PC for low percentages of overlap is about 2%, common pore fractions in AAO are 70 to 80%

increased phonon scattering. Since the highest ZT is most easily obtained, when a nanowire-based device is sealed into a vacuum housing, it should be noted that nanowires suffer from problems with respect to mechanical stability at aspect ratios in the vicinity 50:1. For a nanowire-vacuum composite structure this would imply limitations to the maximum device heights. In the case of sensorics this implies limitations to the sensitivity of the nanowire-based devices. In conclusion, much more research is needed with respect to nanowire mechanical stability, surface and increased volume fraction in media with low thermal conductivity and their impact as thermal shunts for potential nanowire-based devices.

Bibliography

- [1] D.M. Rowe, editor. *Thermoelectrics Handbook - macro to nano*. CRC Press, Taylor & Francis Group, 2006.
- [2] L.D. Hicks and M.S. Dresselhaus. Thermoelectric figure of merit of a one-dimensional conductor. *Physical Review B*, 47(24):16631–16634, June 1993.
- [3] L.D. Hicks and M.S. Dresselhaus. Effect of quantum-well structures on the thermoelectric figure of merit. *Physical Review B*, 47(19):12727–12731, March 1993.
- [4] R.B. Dingle. The electrical conductivity of thin wires. *Proceedings of the Royal Society of London. Series A, Mathematical and Physical Sciences*, 201:545–560, 1950.
- [5] A.F. Mayadas and M. Shatzkes. Electrical-resistivity model for polycrystalline films : the case of arbitrary reflection at external surfaces. *Physical Review B*, 1(4):1382–1389, February 1970.
- [6] T.W. Cornelius, M.E. Toimil Molares, R. Neumann, G. Fahsold, R. Lovrincic, A. Pucci, and S. Karim. Quantum size effects manifest in infrared spectra of single bismuth nanowires. *Applied Physics Letters*, 88(103114), 2006.
- [7] A. Balandin and K.L. Wang. Effect of phonon confinement on the thermoelectric figure of merit of quantum wells. *Journal of Applied Physics*, 84(11):6149–6153, 1998.
- [8] Yu.A. Boikov, B.M. Gol'tsman, and V.A. Danilov. Ways to raise the figure of merit of semiconductor thermoelectric materials. *Semiconductors*, 29:464–470, 1995.

- [9] R. Venkatasubramanian, E. Siivola, T. Colpitts, and B. O'Quinn. Thin-film thermoelectric devices with high room-temperature figures of merit. *Nature*, 413:597–602, 2001.
- [10] Xinfeng Tang, Wenjie Xie, Han Li, Wenyu Zhao, Qingjie Zhang, and Masayuki Niino. Preparation and thermoelectric transport properties of high-performance p-type Bi_2Te_3 with layered nanostructure. *Applied Physics Letters*, 90:012102, January 2007.
- [11] M.P. Singh and C.M. Bhandari. Thermoelectric properties of bismuth telluride quantum wires. *Solid State Communications*, 127(9-10):649–654, 2003.
- [12] I. Bejenari and V. Kantser. Thermoelectric properties of bismuth telluride nanowires in the constant relaxation-time approximation. *Physical Review B*, 78:115322, 2008.
- [13] A. Mavrokefalos, A.L. Moore, M.T. Pettes, L. Shi, W. Wang, and X. Li. Thermoelectric and structural characterizations of individual electrodeposited bismuth telluride nanowires. *Journal of Applied Physics*, 105:104318, 2009.
- [14] T.J. Seebeck. Ueber die magnetische Polarisaton der Metalle und Erze durch Temperaturdifferenz. *Annalen der Physik*, 82:253–286, 1826.
- [15] G.S. Nolas, J. Sharp, and H.J. Goldsmid, editors. *Thermoelectrics - Basic Principles and New Materials Development*, volume 45 of *Springer Series in Materials Science*. Springer, 2001.
- [16] G. Wiedemann and R. Franz. Ueber die Wärme-Leitungsfähigkeit der Metalle. *Annalen der Physik und Chemie*, LXXXIX(8):497–531, 1853.
- [17] V.A. Kulbachinskii, H. Negishi, M. Sasaki, Y. Gimán, M. Inoue, P. Losták, and J. Horák. Thermoelectric power and scattering of carriers in $\text{Bi}_{2-x}\text{Sn}_x\text{Te}_3$ with layered structure. *physica status solidi b*, 199:505–513, 1997.
- [18] R.W. Keyes. High-temperature thermal conductivity of insulating crystals: Relationship to the melting point. *Physical Review*, 115:564–567, 1959.

- [19] D.A. Wright. Thermoelectric Properties of Bismuth Telluride and its Alloys. *Nature*, 181:834, 1958.
- [20] O. Yamashita and S. Tomiyoshi. High performance n-type bismuth telluride with highly stable thermoelectric figure of merit. *Journal of Applied Physics*, 95(11):6277–6285, June 2004.
- [21] O. Yamashita, S. Tomiyoshi, and K. Makita. Bismuth telluride compounds with high thermoelectric figures of merit. *Journal of Applied Physics*, 93(1):368–374, January 2003.
- [22] J.M. Schultz, J.P. McHugh, and W.A. Tiller. Effects of Heavy Deformation and Annealing on the Electrical Properties of Bi_2Te_3 . *Journal of Applied Physics*, 33:2443–2450, 1962.
- [23] J.W.G. Bos, H.W. Zandbergen, M.-H. Lee, N.P. Ong, and R.J. Cava. Structures and thermoelectric properties of the infinitely adaptive series $(\text{Bi}_2)_m(\text{Bi}_2\text{Te}_3)_n$. *Physical Review B*, 75:195203, 2007.
- [24] O. Madelung, editor. *Landolt Börnstein New Series IV/5B : Phase Equilibria, Crystallographic and Thermodynamic Data of Binary Alloys*, volume 5B: B-Ba - C-Zr. Springer, Berlin, 1983.
- [25] M.H. Francombe. Structure-cell data and expansion coefficients of bismuth telluride. *British Journal of Applied Physics*, 9:415–417, 1958.
- [26] S. Michel, S. Diliberto, C. Boulanger, N. Stein, and J.M. Lecuire. Galvanostatic and potentiostatic deposition of bismuth telluride films from nitric acid solution : effect of chemical and electrochemical parameters. *Journal of Crystal Growth*, 277(1-4):274–283, April 2005.
- [27] J.R. Drabble and C.H.L. Goodman. Chemical bonding in bismuth telluride. *Journal of Physics and Chemistry of Solids*, 5:142–144, 1958.
- [28] R.O. Carlson. Anisotropic diffusion of copper into bismuth telluride. *J. Phys. Chem. Solids*, 13:65–70, 1960.
- [29] J.P. Fleurial, L. Gailliard, R. Triboulet, H. Scherrer, and S. Scherrer. Thermal properties of high quality single crystals of bismuth telluride - part i : experimental characterization. *Journal of Physics and Chemistry of Solids*, 49(10):1237–1247, 1988.

- [30] H.J. Goldsmid. The electrical conductivity and thermoelectric power of bismuth telluride. *Proceedings of the Physical Society*, 71:633–646, 1960.
- [31] R.T. Delves, A.E. Bowley, D.W. Hazelden, and H.J. Goldsmid. Anisotropy of the electrical conductivity in bismuth telluride. *Proceedings of the Physical Society*, 78:838–843, 1961.
- [32] S.K. Mishra, S. Satpathy, and O. Jepsen. Electronic structure and thermoelectric properties of bismuth telluride and bismuth selenide. *J. Phys.: Condens. Matter*, 9:461–470, 1997.
- [33] D.L. Greenaway and G. Harbeke. Band structure of bismuth telluride , bismuth selenide and their respective alloys. *Journal of Physics and Chemistry of Solids*, 26:1585–1604, 1965.
- [34] V. Damodara Das and N. Soundararajan. Size and temperature effects on the thermoelectric power and electrical resistivity of bismuth telluride thin films. *Physical Review B*, 37(9):4552–4560, March 1988.
- [35] H.J. Goldsmid, A.R. Sheard, and D.A. Wright. The performance of bismuth telluride thermojunctions. *British Journal of Applied Physics*, 9:367–370, 1958.
- [36] H.J. Goldsmid. The thermal conductivity of bismuth telluride. *Proc. Phys. Soc.*, 69:203–209, 1956.
- [37] T.W. Cornelius, M.E. Toimil Molaes, R. Neumann, and S. Karim. Finite-size effects in the electrical transport properties of single bismuth nanowires. *Journal of Applied Physics*, 100:114307, 2006.
- [38] V.B. Sandomirskii. Quantum size effect in a semimetal film. *Soviet Physics JETP*, 25(1):101–106, July 1967.
- [39] O. Madelung, editor. *Landolt Börnstein New Series 17f : Numerical Data and Functional Relationships in Science and Technology, New Series*, volume 17f (pp.272-278). Springer Verlag, Berlin, 1983.
- [40] A. I. Hochbaum, R. Chen, R.D. Delgado, W. Liang, E.C. Garnett, M. Najarian, A. Majumdar, and P. Yang. Enhanced thermoelectric performance of rough silicon nanowires. *Nature*, 451:163–167, 2008.

- [41] A.I. Boukai, Y. Bunimovich, J. Tahir-Kheli, J.-K. Yu, W.A. Goddard III, and J.R. Heath. Silicon nanowires as efficient thermoelectric materials. *Nature*, 451:168–171, 2008.
- [42] C. Chiritescu, C. Mortensen, D.G. Cahill, D. Johnson, and P. Zschack. Lower limit to the lattice thermal conductivity of nanostructured Bi_2Te_3 -based materials. *Journal of Applied Physics*, 106:073503, 2009.
- [43] Y. Deng, C.-W. Cui, N.L. Zhang, T.H. Ji, Q.-L. Yang, and L. Guo. Bi_2Te_3 -Te nanocomposite formed by epitaxial growth of Bi_2Te_3 sheets on te rods. *Journal of Solid State Chemistry*, 179:1575–1580, 2006.
- [44] Y. Deng, C.-W. Nan, G.-D. Wei, L. Guo, and Y.-H. Lin. Organic-assisted growth of bismuth telluride nanocrystals. *Chemical Physics Letters*, 374:410–415, 2003.
- [45] X.A. Fan, J.Y. Yan, Z. Xie, K. Li, W. Zhu, X.K. Duan, C.J. Xiao, and Q.Q. Zhang. Bi_2Te_3 hexagonal nanoplates and thermoelectric properties of n-type Bi_2Te_3 nanocomposites. *Journal of Physics D : Applied Physics*, 40:5975–5979, 2007.
- [46] A. Purkayastha, Q. Yan, M.S. Raghuveer, D.D. Gandhi, H. Li, Z.W. Liu, R.V. Ramanujan, T. Borca-Tasciuc, and G. Ramanath. Surfactant-directed synthesis of branched bismuth telluride/sulfide core/shell nanorods. *Advanced Materials*, 20:2679–2683, 2008.
- [47] H. Yu, P.C. Gibbons, and W.E. Buhro. Bismuth, tellurium , and bismuth telluride nanowires. *Journal of Materials Chemistry*, 14:595–602, 2004.
- [48] F. Xiao, B. Yoo, K.H. Lee, and N.V. Myung. Synthesis of Bi_2Te_3 nanotubes by galvanic displacement. *Journal of the American Chemical Society*, 129:10068–10069, 2007.
- [49] A. Purkayastha, F. Lupo, S. Kim, T. Borca-Tasciuc, and G. Ramanath. Low-temperature, template-free synthesis of single-crystal bismuth telluride nanorods. *Advanced Materials*, 18:496–500, 2006.
- [50] W.-L. Wang, C.-C. Wan, and Y.-Y. Wang. Investigation of electrodeposition of Bi_2Te_3 nanowires into nanoporous alumina templates with a

- rotating electrode. *Journal of Physical Chemistry B*, 110:12974–12980, 2006.
- [51] M.S. Sander, A.L. Prieto, R. Gronsky, T. Sands, and A.M. Stacy. Fabrication of high-density, high aspect ratio, large-area bismuth telluride nanowire array by electrodeposition into porous anodic alumina templates. *Advanced Materials*, 14(9):665–667, 2002.
- [52] L. Li, Y. Yang, X. Huang, G. Li, and L. Zhang. Pulsed electrodeposition of single-crystalline Bi_2Te_3 nanowire arrays. *Nanotechnology*, 17(6):1706–1712, March 2006.
- [53] S.A. Sapp, B.B. Kakshmi, and C.R. Martin. Template synthesis of bismuth telluride nanowires. *Advanced Materials*, 11(5):402–404, 1999.
- [54] C. Jin, X. Xiang, C. Jia, W. Liu, W. Cai, L. Yao, and X. Li. Electrochemical fabrication of large-area, ordered Bi_2Te_3 nanowire arrays. *Journal of Physical Chemistry B*, 108:1844–1847, 2004.
- [55] M.S. Sander, R. Gronsky, T. Sands, and A.M. Stacy. Structure of bismuth telluride nanowire arrays fabricated by electrodeposition into porous anodic alumina templates. *Chemistry of Materials*, 15:335–339, 2003.
- [56] E.J. Menke, Q. Li, and R.M. Penner. Bismuth telluride (Bi_2Te_3) nanowires synthesized by cyclic electrodeposition/stripping coupled with step edge decoration. *Nano Letters*, 4(10):2009–2014, September 2004.
- [57] W. Wang, Q. Huang, F. Jia, and J. Zhu. Electrochemically assembled p-type Bi_2Te_3 nanowire arrays. *Journal of Applied Physics*, 96(1):615–618, 2004.
- [58] J. Lee, S. Farhangfar, J. Lee, L. Cagnon, R. Scholz, U. Gösele, and K. Nielsch. Tuning the crystallinity of thermoelectric Bi_2Te_3 nanowire arrays grown by pulsed electrodeposition. *Nanotechnology*, 19:365701, 2008.
- [59] L. Trahey, C.R. Becker, and A.M. Stacy. Electrodeposited bismuth telluride nanowire arrays with uniform growth fronts. *Nano Letters*, 7:2535–2539, 2007.
- [60] A.L. Prieto, M.S. Sander, M.S. Martín-González, R. Gronsky, T. Sands,

- and A.M. Stacy. Electrodeposition of ordered Bi_2Te_3 nanowire arrays. *J. Am. Chem. Soc.*, 123:7160–7161, 2001.
- [61] M.A. Thompson, E.J. Menke, C.C. Martens, and R.M. Penner. Shrinking nanowires by kinetically controlled electrooxidation. *Physical Chemistry B Letters*, 110:36–41, 2006.
- [62] D.-A. Borca-Tasciuc and G. Chen. Anisotropic thermal properties of nanochanneled alumina templates. *Journal of Applied Physics*, 97:084303, 2005.
- [63] K.G. Biswas, T.D. Sands, B.A. Cola, and X. Xu. Thermal conductivity of bismuth telluride nanowire array-epoxy composite. *Applied Physics Letters*, 94:223116, 2009.
- [64] E.J. Menke, M.A. Brown, Q. Li, J.C. Hemminger, and R.M. Penner. Bismuth telluride Bi_2Te_3 nanowires : Synthesis by cyclic electrodeposition/stripping, thinning by electrooxidation , and electrical power generation. *Langmuir*, 22:10564–10574, 2006.
- [65] E. Koukharenko, X. Li, I. Nandhakumar, N. Frety, S.P. Beeby, D. Cox, M.J. Tudor, B. Schiedt, C. Trautmann, A. Bertsch, and N.M. White. Towards a nanostructured thermoelectric generator using ion-track lithography. *J. Micromech. Microeng.*, 18:104015, 2008.
- [66] F. Xiao, B. Yoo, K.-H. Lee, and N.V. Myung. Electro-transport studies of electrodeposited $(\text{Bi}_{1-x}\text{Sb}_x)_2\text{Te}_3$ nanowires. *Nanotechnology*, 18:335203, 2007.
- [67] J. Zhou, C. Jin, Jae Hun Seol, Xiaoguang Li, and Li Shi. Thermoelectric properties of individual electrodeposited bismuth telluride nanowires. *Applied Physics Letters*, 87:133109, 2005.
- [68] M. von Ardenne, G. Musiol, and U. Klemradt, editors. *Effekte der Physik und ihre Anwendung*. Verlag Harri Deutsch, 2005.
- [69] R.L. Fleischer, P.B. Price, and R.M. Walker. *Nuclear Tracks in Solids, Principles and Applications*. University of California Press, Berkeley, 1975.
- [70] Y. Sun, Z. Zhu, Z. Wang, Y. Jin, J. Liu, M. Hou, and Q. Zhang. Swift heavy ions induced amorphisation and chemical modification in polycar-

- bonate. *Nuclear Instruments and Methods in Physics Research B*, 209:188–193, 2003.
- [71] F. Dehaye, E. Balanzat, E. Ferain, and R. Legras. Chemical modifications induced in bisphenol A polycarbonate by swift heavy ions. *Nuclear Instruments and Methods in Physics Research B*, 209:103–112, 2003.
- [72] V. Picq, J.M. Ramillon, and E. Balanzat. Swift heavy ions on polymers: Hydrocarbon gas release. *Nuclear Instruments and Methods in Physics Research B*, 146:496–503, 1998.
- [73] F. Peterson and W. Enge. Energy loss dependent transversal etching rates of heavy ion tracks in plastic. *Radiation Measurements*, 25(1-4):43–46, 1995.
- [74] P. Apel, A. Schulz, R. Spohr, C. Trautmann, and V. Vutsadakis. Track size and track structure in polymer irradiated by heavy ions. *Nuclear Instruments and Methods in Physics Research B*, 146(1-4):468–474, December 1998.
- [75] J.F. Ziegler. SRIM 2008 - www.srim.org.
- [76] C. Trautmann, S. Bouffard, and R. Spohr. Etching threshold for ion tracks in polyimide. *Nuclear Instruments and Methods in Physics Research B*, 116:429–433, 1996.
- [77] M.E. Toimil Molares, J. Brötz, V. Buschmann, D. Dobrev, R. Neumann, R. Scholz, I.U. Schuchert, C. Trautmann, and J. Vetter. Etched heavy ion tracks in polycarbonate as template for copper nanowires. *Nuclear Instruments and Methods in Physics Research B*, 185(1-4):192–197, 2001.
- [78] C. Schöneberger, B.M.I. van der Zande, L.G.J. Fokkink, M. Henny, M. Schmid, C. ND Krüger, A. Bachtold, R. Huber, H. Birk, and U. Staufer. Template synthesis of nanowires in porous polycarbonate membranes - electrochemistry and morphology. *Journal of Physical Chemistry B*, 101(28):5497–5505, 1997.
- [79] E. Ferain and R. Legras. Pore shape control in nanoporous particle track etched membrane. *Nuclear Instruments and Methods in Physics Research B*, 174:116–122, 2001.

- [80] N. Chtanko, M.E. Toimil Molaes, T.W. Cornelius, D. Dobrev, and R. Neumann. Etched single-ion-track templates for single nanowire synthesis. *Journal of Physical Chemistry*, 108:9950–9954, 2004.
- [81] V.A. Ditlov, A.U. Gatchegov, W. Enge, F. Petersen, M. Danziger, A. Schulz, and V. Trofimov. The radial etching velocity for tracks in polymer film. *Radiation Measurements*, 28(1-6):137–144, 1997.
- [82] W. DeSorbo. Ultraviolet effects and aging effects on etching characteristics of fission tracks in polycarbonate film. *Nuclear Tracks*, 3:13–32, 1979.
- [83] G. Pépy, P. Boesecke, A. Kuklin, E. Manceau, B. Schiedt, Z. Siwy, M. Toulemonde, and C. Trautmann. Cylindrical nanochannels in ion-track polycarbonate membranes studied by small-angle X-ray scattering. *Journal of Applied Crystallography*, 40:s388–s392, 2007.
- [84] S. Müller. Thermoelectric Properties of Bismuth Nanowires. Diploma Thesis, Universität Heidelberg, 2008.
- [85] S. Karim. *Fabrication and characterization of gold nanowires*. PhD thesis, Philipps-Universität Marburg, 2007.
- [86] T.W. Cornelius. *Fabrication and characterisation of bismuth nanowires*. PhD thesis, Universität Heidelberg, 2006.
- [87] J.-C. Puipe and F. Leaman. *Theory and Practice of Pulse Plating*. AESF, 1986.
- [88] M. Paunovic and M. Schlesinger. *Fundamentals of electrochemical deposition*. John Wiley & Sons, Inc., 2nd edition, 2006.
- [89] C.H. Hamann, A. Hammett, and W. Vielstich. *Electrochemistry*. WILEY-VCH Verlag GmbH & Co. KGaA, 2007.
- [90] E. Budevski, G. Staikov, and W.J. Lorenz. *Electrochemical Phase Formation and Growth*. VCH, 1996.
- [91] C.G. Zoski, editor. *Handbook of Electrochemistry*. Elsevier, first edition, 2007.

- [92] W. Sparreboom, A. van den Berg, and J.C.T. Eijkel. Principles and applications of nanofluidic transport. *Nature Nanotechnology*, 4:713–719, 2009.
- [93] M.S. Martín-González, A.L. Prieto, R. Gronsky, T. Sands, and A.M. Stacy. Insights into the electrodeposition of Bi_2Te_3 . *Journal of the Electrochemical Society*, 149(11):C546–C554, 2002.
- [94] S. Wen, R.R. Corderman, F. Seker, A.-P. Zhang, L. Denault, and M.L. Blohm. Kinetics and initial stages of bismuth telluride electrodeposition. *Journal of the Electrochemical Society*, 153(9):C595–C602, 2006.
- [95] P. Magri, C. Boulanger, and J.-M. Lecuire. Synthesis, properties and performances of electrodeposited bismuth telluride films. *J. Mater. Chem.*, 6(5):773–779, 1996.
- [96] M. Takahashi, Y. Katou, K. Nagata, and S. Furuta. The composition and conductivity of electrodeposited Bi-Te alloy films. *Thin Solid Films*, 240:70–72, 1994.
- [97] K. Tittes, A. Bund, W. Plieth, A. Bentien, S. Paschen, M. Plötner, H. Gräfe, and W.-J. Fischer. Electrochemical deposition of Bi_2Te_3 for thermoelectric microdevices. *Journal of Solid State Electrochemistry*, 7:714–723, 2003.
- [98] S. Michel, S. Diliberto, C. Boulanger, and B. Bolle. Effect of electrochemical deposition on the crystallographic texture of bismuth telluride alloys. *Journal of Crystal Growth*, 296:227–233, 2006.
- [99] S. Li, M.S. Toprak, H.M.A. Soliman, J. Zhou, M. Muhammed, D. Platzek, and E. Müller. Fabrication of nanostructured thermoelectric bismuth telluride thick films by electrochemical deposition. *Chemistry of Materials*, 18:3627–3633, 2006.
- [100] S. Golia, M. Arora, R.K. Sharma, and A.C. Rastogi. Electrochemically deposited bismuth telluride thin films. *Current Applied Physics*, 3:195–197, 2003.
- [101] M. Takahashi, M. Kojima, S. Sato, N. Ohnisi, A. Nishiwaki, K. Wakita, T. Miyuki, S. Ikeda, and Y. Muramatsu. Electric and thermoelectric

- properties of electrodeposited bismuth telluride Bi_2Te_3 films. *Journal of Applied Physics*, 96(10):5582–5587, November 2004.
- [102] Y. Miyazaki and T. Kajitani. Preparation of Bi_2Te_3 films by electrodeposition. *Journal of Crystal Growth*, 229(1-4):542–546, 2001.
- [103] J. Dheepa, R. Sathyamoorthy, and A. Subbarayan. Optical properties of thermally evaporated Bi_2Te_3 thin films. *Journal of Crystal Growth*, 274:100–105, 2005.
- [104] A. Suresh, K. Chatterjee, V.KR. Sharma, S. Ganguly, K. Kargupta, and D. Banerjee. Effect of pH on structural and electrical properties of electrodeposited Bi_2Te_3 thin films. *Journal of Electronic Materials*, 38:449–452, 2009.
- [105] L. Philippe, N. Kacem, and J. Michler. Electrochemical deposition of metals inside high aspect ratio nanoelectrode array. analytical current expression and multidimensional kinetic model for cobalt nanostructure synthesis. *Journal of Physical Chemistry C*, 111:5229–5235, 2007.
- [106] S. Valizadeh, J.M. George, P. Leisner, and L. Hultman. Electrochemical deposition of Co nanowire arrays; quantitative consideration of concentration profiles. *Electrochimica Acta*, 47:865–874, 2001.
- [107] M.E. Toimil Molares, V. Buschmann, D. Dobrev, R. Neumann, R. Scholz, I.U. Schuchert, and J. Vetter. Single-crystalline copper nanowires produced by electrochemical deposition in polymeric ion track membranes. *Advanced Materials*, 13(1):62–65, 2001.
- [108] T.W. Cornelius, J. Brötz, N. Chtanko, D. Dobrev, G. Mieke, R. Neumann, and M.E. Toimil Molares. Controlled fabrication of poly- and single-crystalline bismuth nanowires. *Nanotechnology*, 16(5):S246–S249, May 2005.
- [109] S. Karim, M.E. Toimil Molares, F. Maurer, G. Mieke, W. Ensinger, J. Liu, T.W. Cornelius, and R. Neumann. Synthesis of gold nanowires with controlled crystallographic characteristics. *Applied Physics A*, 84:403–407, 2006.
- [110] Te - JCPDS 86-2268.

- [111] BiTe - JCPDS 31-200.
- [112] Bi₂Te₃ - JCPDS 8-27.
- [113] Bi₄Te₃ - JCPDS 75-1096.
- [114] H. Chaoui, J. Bessieres, A. Modaressi, and J.J. Heizmann. Texture prediction of Bi₂Te₃ electroplated layers using Hartman's theory of crystal growth. *Journal of Applied Electrochemistry*, 30:419–427, 2000.
- [115] A.C. Yang and F.D. Shepherd. n- and p-type single crystal bismuth telluride. *Journal of the Electrochemical Society*, 108(2):197–198, February 1961.
- [116] P.F. Schmidt. *Praxis der Rasterelektronenmikroskopie und Mikobereichsanalyse*. Expert Verlag, 1994.
- [117] H. Haken and H.C. Wolf. *Atom- und Quantenphysik*. Springer Verlag, 7 edition, 2001.
- [118] P. Apel. Swift ion effects in polymers : industrial applications. *Nuclear Instruments and Methods in Physics Research B*, 208:11–20, 2003.
- [119] P. Apel. Track etching technique in membrane technology. *Radiation Measurements*, 34:559–566, 2001.
- [120] D. Dobrev, J. Vetter, N. Angert, and R. Neumann. Electrochemical growth of copper single crystals in pores of polymer ion-track membranes. *Applied Physics A*, 69:233–237, 1999.
- [121] D. Dobrev, J. Vetter, and N. Angert. Electrochemical preparation of metal microstructures on large areas of etched ion track membranes. *Nuclear Instruments and Methods in Physics Research B*, 149:207–212, 1999.
- [122] A.Yu. Didyk, S.N. Dmitriev, and W. Vutsadakis. Spatial overlapping of holes in nuclear-track membranes with differentt angular distributions. *High Energy Chemistry*, 37(2):89–95, 2003.
- [123] J. Keyani, A.M. Stacy, and J. Sharp. Assembly and measurement of a hybrid nanowire-bulk thermoelectric device. *Applied Physics Letters*, 89:233106, 2006.

-
- [124] W. Wang, F. Jia, Q. Huang, and J. Zhang. A new type of low power thermoelectric micro-generator fabricated by nanowire array thermoelectric material. *Microelectronic Engineering*, 77:223–229, 2005.

Acknowledgments

At this point I would like to thank all people who contributed to the success of this work :

- Prof. Dr. R. Neumann for the opportunity to perform this doctoral work in the Materials Research Department at GSI, for his supervision and the freedom of choice with respect to the focus of this scientific work. In addition, for the possibility to attend several interesting workshops and international conferences, as well as the possibility to present my work within the framework of the group's international collaborations.
- Prof. Dr. A. Pucci from the Kirchhoff Institute for Physics of Heidelberg University for acting as a referee for this dissertation.
- Dr. M.E. Toimil-Molares for her help and support during the doctoral work, many interesting scientific discussions as well as for reading and correcting this work.
- Dipl.-Phys. S. Müller for his support during the doctoral work, many critical and helpful discussions on thermoelectrics and measurement techniques and for commenting on this work.
- Dipl.-Chem. M. Rauber for the interesting discussions on (electro-)chemistry and nanofluidic transport.
- Dr. C. Trautmann for the introduction to the field of heavy-ion irradiation, helping with ion beam-related questions and her advice and encouragement.
- Dr. T. Cornelius for the introduction to the field of electrochemical nanowire growth.

- From the Institute for Material Science of the University of Technology Darmstadt, I am grateful to Dr. J. Brötz for XRD measurements and XRD-related discussions, as well as Dr. S. Lauterbach for first TEM measurements.
- Dr. W. Sigle from the MPI for Metals Research in Stuttgart for HRTEM and HRTEM/EDX measurements.
- Dipl.-Phys. V. Bayer, Dipl.-Phys. B. Schuster and Dipl.-Chem. T. Seidl for many fruitful and interesting (non-)scientific discussions in- and outside the group's coffee room.
- Dr. K.O.-Voss for his patient help in the group's machine shop.
- Prof. F. Vöklein, M.SC. M. Schmitt and M.SC. H. Reith of the Hochschule RheinMain University of Applied Sciences for their efforts in contacting single nanowires and characterizing the thermoelectric properties.
- E. Schubert and A. Siegmund for their technical support.
- The whole group of the Materials Research Department of GSI for the very pleasant working conditions and diverting coffee breaks.
- All group members who kindly agreed to critically read and comment on excerpts of this work.
- The DFG for partially funding this research within the priority program SPP 1165.

Finally, I would like to thank my parents W.-D. and U. Picht, my brother B. Picht and, in particular, my partner Ch. Purps for their constant personal support, encouragement, optimism and their ability to cheer me up whenever needed.